ULTRAFAST CARRIER DYNAMICS OF WIDE GAP SEMICONDUCTORS STUDIED VIA FOUR-WAVE-MIXING AND PUMP-PROBE SPECTROSCOPIES

By

ARTHUR J. FISCHER

Bachelor of Arts

University of Chicago

Chicago, Illinois

1992

Submitted to the Faculty of the
Graduate College of the
Oklahoma State University
in partial fulfillment of
the requirements for
the Degree of
DOCTOR OF PHILOSOPHY
July, 1998

ULTRAFAST CARRIER DYNAMICS OF WIDE GAP SEMICONDUCTORS STUDIED VIA FOUR-WAVE-MIXING AND PUMP-PROBE SPECTROSCOPIES

Thesis Approved:

Thesis Adviser

Dean of the Graduate College

ACKNOWLEDGEMENTS

I wish to express my sincere gratitude to my thesis advisor Dr. Jin-Joo Song for giving me the opportunity to work in her laboratory. With her guidance and support, I learned a great deal about being an experimental physicist. I would also like to extend my deepest gratitude to the members of my thesis committee, Dr. Dixon, Dr. Krasinski, Dr. Hauenstein, and Dr. Xie, for their valuable input into my research as well as their careful review of my thesis.

I would like to thank Dr. Dai-Sik Kim for teaching me how to do ultrafast laser spectroscopy. I am indebted to Dr. Wei Shan for teaching me valuable experimental techniques in linear spectroscopy. I would also like to thank all the members of Dr. Song's group past and present with whom I was fortunate enough to work: John Hays, John Jacob, Abdul Bouchalka, Seon-Ju Hwang, Gil-Han Park, Yong-Hoon Cho, Ted Schmidt, Brian Little, Serge Bidnyk, Gordon Gainer, Chan-Kyung Choi. I feel I benefitted greatly from working in a large group. The advice, support, and comradery of this research group helped to make this work possible.

I would like to thank my mother and father for their constant support. My deepest appreciation goes to my wife, Catherine, for her encouragement during times of difficulty, her love, her sacrifices, and her understanding as I worked towards this degree.

TABLE OF CONTENTS

Chapter Page

I. INTRODUCTION 1

II. GENERAL ASPECTS OF EXCITONS 6

Band Structure 6
ZnSe 8
GaN 10
Excitons 10

III. GaN ABSORPTION 17

Introduction 17
General features of absorption 18
Phonon-Assisted Absorption 27
Temperature Dependence 29

IV. COHERENT-TRANSIENT DEGENERATE FOUR-WAVE-MIXING: EXPERIMENT AND THEORY 34

Experimental Considerations 34
Experimental Setup 35
Sample Preparation 40
Theoretical Description of CT-FWM 43
Non-Interacting Two-Level Model 43
The Optical Bloch Equations 44
Density Matrix Formalism 45
Derivation of the Optical Bloch Equations 46
Interpretation of the Optical Bloch Equations 49
Coherent-Transient Degenerate Four-Wave-Mixing . . . 50
More Advanced Models Considering Interaction 52

V. FOUR-WAVE-MIXING MEASUREMENTS IN ZnSe-BASED MATERIALS 55

Introduction 55
Extremely High Order Signals 61
Third-Order Signal 70

Chapter Page
Origin of Nonlinearity 70
Negative Time Delay Signal 74
Exciton-Phonon Interaction 76
Exciton-Exciton Interaction 82
Localization Study 87
Conclusions 94

VI. FOUR-WAVE-MIXING IN GaN EPILAYERS 95

Introduction 95
Linewidth Analysis 97
Quantum Beating 103
Conclusion 107

VII. FEMTOSECOND OPTICAL PUMPING AND PUMP-PROBE MEASUREMENTS IN GaN EPILAYERS 109

Introduction 109
Stimulated Emission Measurements 110
Pump-Probe Measurements 110
Conclusions 121

VIII. THz SPECTROSCOPY OF SEMICONDUCTOR SAMPLES 122

Generation of THz Radiation 123
Photoconduction 123
Optical Rectification 125
Detection of THz Radiation 125
Electro-Optic Sampling 125
Antenna Detection 127

IX. CONCLUSIONS 132

BIBLIOGRAPHY 134

APPENDIX 142

APPENDIX A - CALCULATION OF THE THIRD ORDER POLARIZATION 143

LIST OF FIGURES

Figure Page

1. Diagram of the zinc blende structure. 9
2. Fundmental bands of ZnSe and GaN near the zone center. 11
3. Diagram of the wurtzite crystal structure. 12
4. Schematic diagram of Wannier and Frenkel excitons. 14
5. Diagram of the experimental set up used for absorption measurements. . 19
6. Absorption spectrum at 10 K of a 0.38 micron thick epilayer of GaN. . . 21
7. Absorption spectra for two different polarization geometries. 23
8. Absorption spectra at 10 K taken from samples of four different thicknesses. 24
9. Fit of the 10 K absorption data to the Elliot equation assuming three bands. 26
10. Calculation of indirect exciton absorption for CdS and GaN. 28
11. Absorption spectra for temperatures from 100 K to 475 K. 30
12. Exciton peak energy position (a) and broadening (b) shown as a function of temperature. 31
13. Coherent-transient degenerate four-wave-mixing (CT-DFWM) experimental set up 36
14. Scattering geometry for CT-DFWM 38
15. Autocorrelation and cross-correlation of laser pulses 41
16. Sample Structure of a ZnSe multiple quantum well 58
17. FWM signal for both the reflection and transmission geometries from the same sample. 59

Figure Page

18. Absorption and Photoluminescence data for a ZnCdSe/ZnSe MQW sample. 60

19. Photograph of higher order wave-mixing signals. 62

20. Third, fifth, and seventh order mixing signals shown as a function of pump power. 63

21. Power law dependence of the the third and fifth order signals. 65

22. Higher order FWM signals plotted as a function of time delay 66

23. Spectrally-Resolved FWM for the third, fifth and seventh order signals . 67

24. Comparison of signal intensities between ZnCdSe and GaAS MQW samples 69

25. FWM signal as a function of center laser frequency for a ZnCdSe MQW sample. 71

26. TI-FWM with the laser detuning centered at the HH, LH and Free Carrier energies. 73

27. FWM signal as a function of temperature for bulk ZnSe 75

28. FWM time constants for positive and negative delay from an epilayer of ZnSe. 77

29. FWM data as a function of temperature for several representative temperatures. 78

30. Decay rates of FWM for a ZnSe epilayer and a ZnCdSe MQW sample. . 79

31. Laser beam profile measured with a CCD camera. 83

32. FWM signal plotted for several different exciton densities. 84

33. Homogeneous linewidth plotted as a function of exciton density. 85

34. FWM data for samples A and B at 10 K. 89

35. FWM data on the high and low energy sides of the excitonic resonance. 90

36. Decay Rates for samples A and B plotted as a function of photon energy. 91

37. Homogeneous linewidth plotted as function of exciton density for Sample B for energy positions 4 meV above and below the line center. 93

Figure | Page

38. Time-integrated four-wave-mixing (TI-FWM) signal from a GaN epilayer at several temperatures. 98

39. Homogeneous linewidth derived from TI-FWM data plotted as a function of temperature. 99

40. Spectrally-resolved four-wave-mixing from the A and B Excitonic resonances at several temperatures. 101

41. Spectrally-resolved four-wave-mixing linewidth plotted as a function of temperature. 102

42. Time-integrated four-wave-mixing data at 10 K for different detunings around the B exciton. 104

43. Time-integrated four-wave-mixing signal at 10 K for collinear and cross-linear polarization geometries. 106

44. Calculated four-wave-mixing signal in the the ultrashort pulse limit. . . 108

45. Femtosecond simulated emission data at 10 K from GaN/Sapphire. . . . 111

46. Femtoseond stimulated emision at medium and high powers. 112

47. Absorption spectra at 10 K as a function of pump fluence. 115

48. Absorption spectra as a function of delay between the laser pump and white-light continuum probe. 117

49. Absorption spectra as a function of delay. 118

50. Absorption as a function of delay for the three dicrete wavelengths. . . . 120

51. Schematic diagram of a photoconducting antenna 124

52. Experimental set up for electro-optic sampling. 126

53. Experimental set up using antennas for both emission and detection. . . 128

54. THz radiation emitted from an unbiased InGaAs sample. 129

55. Frequency spectrum of the THz data from InGaAs. 131

CHAPTER I

INTRODUCTION

During the past decade, the growth and characterization of wide band gap semiconductors has received a great deal of attention. This is due to the fact that wide band gap direct semiconductors emit light in a wavelength region from the green to the ultraviolet (UV). Light emitting diodes (LEDs) and laser diodes (LDs) which emit in a wavelength region from the infrared to the red have been available for many years and are based on the material gallium arsenide (GaAs). GaAs-based LDs are used in devices such as red laser pointers and compact disc players. Although there are many interesting areas of active research related to GaAs semiconductors, in many ways GaAs semiconductor science is a mature technology. Using growth techniques such as molecular beam epitaxy (MBE) researchers can accurately grow semiconductor layers which are as thin as a few atomic layers. Researchers have been studying GaAs for many years and can now grow semiconductor samples which exhibit extremely high optical quality with a very low defect density. Therefore, GaAs is a good material system for studies of fundamental physics since much of the defect and impurity related effects can be neglected. GaAs is the most developed semiconductor technology next to Si which is used for virtually all computer integrated circuits (ICs).

For many years scientists and researchers have known of the potential benefits of having small, efficient semiconductor laser diodes operating at shorter wavelengths. Shorter wavelengths can be focused to a smaller spot size which will allow more information to fit on a single optical disc. Compact disc players now operate at wavelengths in the infrared. If this wavelength could be decreased by a factor of two, then

an optical disc could potentially store four times more information. Blue/UV LDs will also open up the possibility for new types of communication systems. Certain wavelengths of light in the blue spectral region travel through water with reduced attenuation. It should be possible to develop an underwater communication system which, for example, would allow communication between submarines. Using emitters and detectors in the UV, it should be possible to transmit data between satellites in orbit which would be impossible for listeners on the ground to intercept since the atmosphere is very good at absorbing UV radiation. Another very important area of application for blue-green LEDs and LDs is for full color displays. In order to complete the basic set of colors we need devices emitting in the red, green, and blue wavelength regions. In general, having a full spectrum of wavelengths greatly increases the usefulness of semiconductor lasers. For example, laser surgery can be performed by utilizing the fact that different types of tissue in the human body absorb light at a different wavelengths. Thus, laser surgeons would like to be able to select the appropriate wavelength for efficiently cutting a particular type of tissue. By having the correct wavelength available, doctors have a larger arsenal of available tools to perform laser surgery.

Since a pure semiconductor emits only at one specific wavelength, special materials must be made in order to produce the wavelengths of interest. For example, pure GaAs emits light only in a very narrow region around 860 nm which is in the infrared. In order to get the range of wavelengths from the infrared to the red, another material must be added to GaAs to form an alloy or, alternatively, very thin layers can be fabricated to form a quantum well (QW). An example of an alloy is AlGaAs. When a small amount of Al is added to GaAs, the material emits at shorter wavelength. By growing extremely thin lasers of GaAs between layers of AlGaAs one can also form a quantum well. Due to the extremely small size of the QW, electrons trapped in the well are governed by quantum mechanics. One main result is that these confined carriers emit light at shorter wavelengths. Quantum wells also have very useful properties for LDs. QW structures can be designed to spatially confine

both the carriers and the optical mode in the same region so that the device will have efficient lasing.

One of the first wide band gap semiconductors to capture the interest of researchers was ZnSe. ZnSe has a band gap of 2.58 eV at room temperature and emits light at about 475 nm which is in the blue-green wavelength region. The company 3M created the first ZnSe laser diode in 1991 [1] using a device based on ZnSe. The device operated at 77 K under pulsed current injection and emitted light at about 490 nm. The lifetime of the device was only a few seconds. With improvements in the device manufacture and material quality, advances were made in the area of p-type doping and a laser diode with continuous wave (CW) operation was achieved [2]. The lifetime of the devices based on ZnSe now exceeds 100 hours [3]. However, the increases in device lifetime have been extremely slow and a commercial device has not yet been realized. Although there is still a great deal of active research on ZnSe, many researchers have turned their attention to the III-Nitrides.

In several ways, gallium nitride (GaN) is a more promising material system than ZnSe. GaN has a direct band gap of 3.4 eV at room temperature which means it emits light in the UV at about 360 nm. By alloying GaN with indium nitride (InN), which has a direct gap at 1.9 eV (650 nm) in red wavelength region, almost the whole visible spectrum can be covered by one semiconductor alloy. It should be possible to produce devices operating at wavelengths further into the UV by alloying GaN with aluminum nitride (AlN). AlN has a direct band gap of 6.2 eV (200 nm) which is in the deep UV spectral region. With the achievement of p-type doping [4,5], blue LEDs were fabricated and are now commercially available. LDs fabricated from InGaN multiple QW structures which operate CW are now reported with a lifetime estimated from high temperature testing at more than 10,000 hours [6]. Thus, LDs based on the III-Nitrides are already commercially viable. So far devices made from InGaN operate well in a wavelength region around 410 nm and researchers are working to expand this wavelength region further towards both the red and the UV. It remains to be seen if LDs made from GaN and AlGaN will develop as rapidly as the devices made from InGaN.

In order to make devices and make improvements to devices, it is important to understand the underlying physics describing the device operation. A detailed understanding of what the carriers are doing inside the material is necessary in order to understand why the material is or is not lasing. One way to learn such information is by studying the optical properties of the materials from which the devices are made. Optical studies provide a non-invasive method of measuring material properties so that certain optical measurements can be a routine part of the device manufacturing process. Optical studies range from the very simplest photoluminescence measurements to very complicated techniques such as four-wave-mixing.

The study of the ultrafast properties of semiconductors has flourished during the past decade because advances in pulsed laser technology have made extremely short laser pulses readily accessible to researchers. Many interesting processes in a semiconductor happen on picosecond and femtosecond time scales. These processes can be divided into coherent and non-coherent regimes. When a semiconductor is excited by an ultrafast laser pulse, the carriers created remain coherent with the exciting laser pulse for a short time. This time is called the dephasing time and is simply the time required for carriers to scatter out of their initially created states and form a quasi-equilibrium state within the conduction band. This is termed quasi-equilibrium because the equilibrium state of an intrinsic, wide band gap semiconductor is one where there are no carriers in the conduction band. However, when carriers are excited to the conduction band they redistribute themselves within the conduction band in a quasi-equilibrium state before recombining with holes. The time for this redistribution is the dephasing time. Processes happening before such a redistribution are coherent processes and process happening after dephasing are non-coherent. Dephasing times in semiconductors usually occur on the ps time scale. Recombination of electrons with holes is usually non-coherent and usually occurs on a time scale of 100 ps or longer.

In this thesis, a wide variety of optical measurement techniques are used to investigate the interaction of light with wide band gap semiconductors. The increased

interest in producing optoelectronic devices operating in the green and blue wavelength regions has paved the way for advances in growth of wide gap semiconductors, so many high quality samples are now available for fundamental optical studies. For this work, samples based on both the ZnSe and the GaN material systems will be studied. Chapter 2 gives a brief introduction to excitons in semiconductors with an emphasis on specific information about ZnSe and GaN. In chapter 3, the results of absorption measurements performed on epilayers of GaN are presented. Absorption is one of the most fundamental optical measurements that can be performed and it tells us at what wavelength a semiconductor sample begins to absorb light. Chapter 4 describes the experimental and theoretical details of coherent-transient degenerate four-wave-mixing (CT-DFWM). CT-DFWM is used to measure the time required for carriers to lose their phase coherence with the original excitation. In chapters 5 and 6, CT-DFWM is discussed for ZnSe and GaN, respectively. In chapter 7, experiments using very high power femtosecond pulses are discussed. Stimulated emission measurements in GaN epilayers using femtosecond pulses show a new emission peak which is not observed under nanosecond excitation. Saturation and recovery of the GaN absorption spectrum are presented which show interesting ultrafast gain dynamics. Finally, chapter 8 contains general conclusions.

CHAPTER II

GENERAL ASPECTS OF EXCITONS

When a photon with energy above the fundamental band gap is incident on a crystal, an electron from the valence band can be promoted to the conduction band. However, this is not the lowest excited state of a crystal. The lowest excited state of the crystal occurs when an electron and a hole are bound to each other via the Coulomb interaction. This bound state of the electron hole pair is referred to as an exciton. Excitons have been shown to dominate the band edge optical properties of wide gap semiconductors even at room temperature. An excitonic state with a light electron bound to a heavier hole very closely parallels a hydrogen atom and, in fact, much of the formalism describing the hydrogen atom can be applied to an exciton. In this chapter, the general properties of excitons will be discussed for excitons in ZnSe and GaN material systems. ZnSe is a material which crystallizes in the zinc blende structure, while GaN crystallizes in a hexagonal wurtzite structure. Many books on solid state physics [7,8] cover binding in crystals and crystal band structure and no attempt is made here to cover the subject in detail. Only a brief introduction is given here as it applies to the materials used in this thesis. The first section of this chapter will describe the band structure of zinc blende and wurtzite crystals. The second section of this chapter will describe the general properties of excitons for each material system.

Band Structure

Atoms are composed of a very small positive nucleus with a distribution of electrons defining a much larger radius around the nucleus. Electrons can be divided into core electrons and valence electrons. Core electrons are strongly bound

to the nucleus, while valence electrons are more weakly bound and for the most part determine the chemical properties of the material. As atoms are brought closer together to form a crystalline material the electronic wave functions of the atoms begin to overlap and there is a repulsive force pushing the atoms apart due to the Pauli exclusion principle. According to the Pauli exclusion principle, no Fermions can occupy the same energy levels at the same time. As an electron distribution moves closer to the electron distribution of a neighboring atom, it feels a repulsive force because it cannot occupy the same core electronic levels surrounding the positive nucleus. However, the electronic distribution also feels an attractive force due to Coulomb interaction with the positive nucleus of the neighboring atom. Thus, atoms are bound at a distance determined by the relative strength of these two forces. The extent to which one atom gives away its electron determines something about the type of binding which will occur. If one atom tends to almost completely give its least bound electron to a neighboring atom, then this type of binding is called ionic binding and is present in salts such as common table salt (NaCl) and other materials composed from elements in columns I and VII of the periodic table. Covalent bonding is characterized by the fact that a large amount of the electronic distribution is positioned in the space between the atoms. Examples of materials with covalent bonding are Si and Ge as well as other materials made from elements in column VI of the periodic chart. Materials can have any degree of binding between ionic and covalent depending on the size of each atom, the electronic environment, as well as many other factors. In this study, we will mainly discuss ZnSe and GaN. ZnSe is a II-VI material with an ionic character stronger than Si or GaAs, but weaker than NaCl. This makes ZnSe somewhat more polar than GaAs in that more electronic charge tends to stay near the selenium atom. This will be important later when we discuss exciton-phonon interaction since more polar materials tend to have larger exciton-phonon interactions. GaN is a III-V material that is expected to have an ionic character that is nearly the same as ZnSe.

As a group of atoms are brought closer together to form a crystal, the electronic wave functions begin to overlap and a series of bands are formed with gaps or regions

where the electrons cannot exist. The spacing and distribution of these bands is determined by the atoms involved and the atoms' electron distributions. For all materials in their ground state at zero temperature, there is some region between occupied levels and unoccupied levels. For a material with a partially full band, carriers can move under the influence of an applied electric field and the material is classified as a metal. For a materials in which the separation between occupied and unoccupied levels occurs in an energy gap, the material is either an insulator or a semiconductor. The separation between an insulator and a semiconductor varies throughout the literature. Some researchers have categorized materials with a band gap larger than 2.0 eV as insulators, and materials with a band gap smaller than 2.0 eV as semiconductors. Semiconductors are very useful because they are conductors under certain circumstances and insulators under others. For example, if we heat up a narrow gap semiconductor carriers will be thermally excited to the conduction band and the material will begin to conduct. For wider gap materials, if we shine light on the material with a photon energy larger than the gap, carriers will be excited to the conduction band and the material will begin to conduct. The two materials studied in this thesis are ZnSe and GaN and have room temperature band gaps of $\approx$ 2.58 and $\approx$ 3.4 eV, respectively. While some researchers might refer to these materials as insulators, they will be referred to here as wide band gap semiconductors. In the next two subsections, the crystal structure and band structure of each material will be discussed in more detail.

ZnSe

ZnSe crystallizes into the zinc blende structure as shown in Fig. 1. Many other materials can crystallize in the zinc blende form such as GaAs, AlAs, InAs, InP, GaP, CdS, and ZnTe. ZnS is the prototypical zinc blende semiconductor and, in fact, the mineral name for ZnS is "zinc blende". The zinc blende structure can be viewed as a diamond lattice with two different atoms instead of all carbon atoms. Alternately the zinc blende structure can be viewed as two interpenetrating face centered cubic lattices where in the case of ZnSe one lattice contains Zn and the other Se.

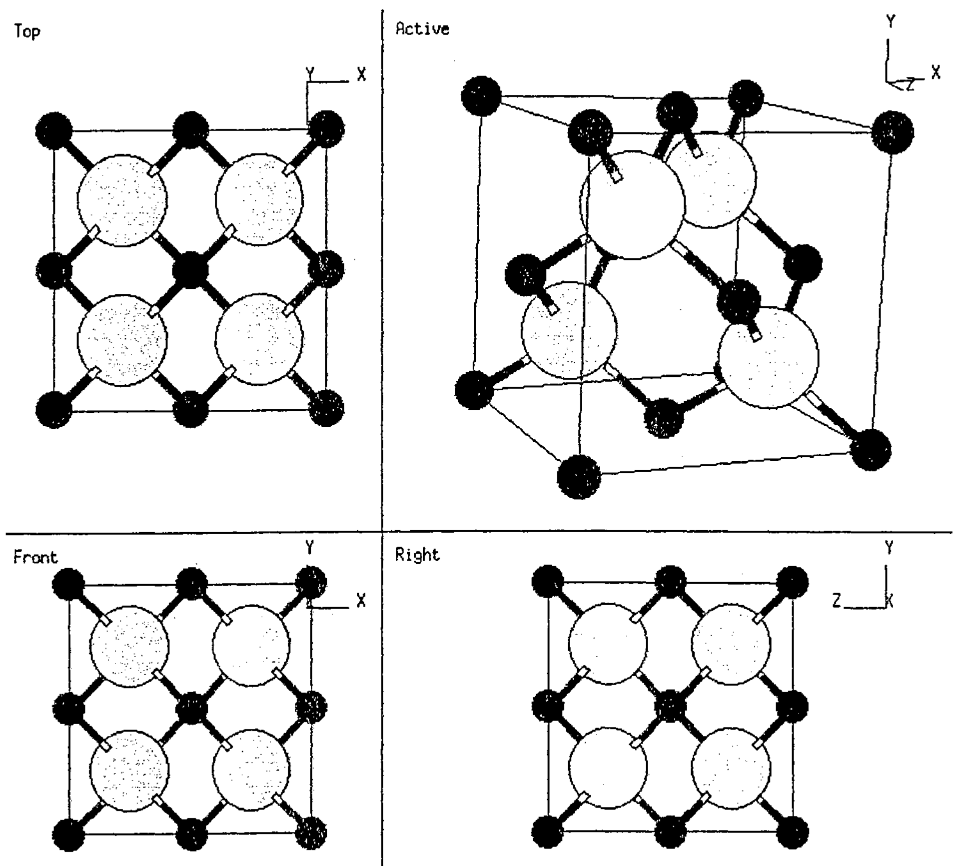

Figure 1. Diagram of the zinc blende structure. [9]

The band structure of ZnSe is very similar to that of GaAs. The fundamental absorption edge of ZnSe corresponds to transitions from the highest valence band to the lowest conduction band at the Γ point which in single-group notation is a transition from Γ_{15}^{ν} to Γ_{1}^{c}. The spin-orbit interaction splits the Γ_{15}^{ν} band into Γ_{7}^{v} and Γ_{8}^{v}which are separated in energy by about 43 meV [10]. This conduction band at lower energy is referred to as the spin-orbit split off band. The fundamental bands of ZnSe are shown in Fig. 2 (a).

GaN

GaN crystallizes with the wurtzite structure as shown in Fig. 3. Several other materials also can take the wurtzite structure such as ZnS, ZnO, SiC, and AlN. The conduction band of GaN has its minimum at the center of the Brillouin zone (Γ point) and has Γ_7 symmetry with a total angular momentum value of $J_Z = 1/2$. The maximum of the valence band also occurs at the zone center so that GaN has a direct fundamental band gap. The valence band is split by both crystal field splitting and spin orbit splitting which means that there are three fundamental valence bands in a small energy region at the Γ point. The three bands are conveniently referred to as the A, B, and C bands. Many recent review articles give extensive details concerning the band structure of GaN as well as other important parameters [12–14]. The fundamental bands of GaN are summarized in Fig. 2 (b).

Excitons

For a pure material, intrinsic free excitons represent the lowest possible excited state of the crystal. Excitons can generally be classified into two categories depending on how tightly bound the electron is to the hole. For materials where the electron and hole are very tightly bound the excitons are referred to as Frenkel excitons [15,16]. A Frenkel exciton is an exciton with an excitonic binding energy so large that the exciton is bound to a single atom of the crystal. A Frenkel exciton can therefore be thought of as an excitation of one atom of the crystal. This excitation can hop

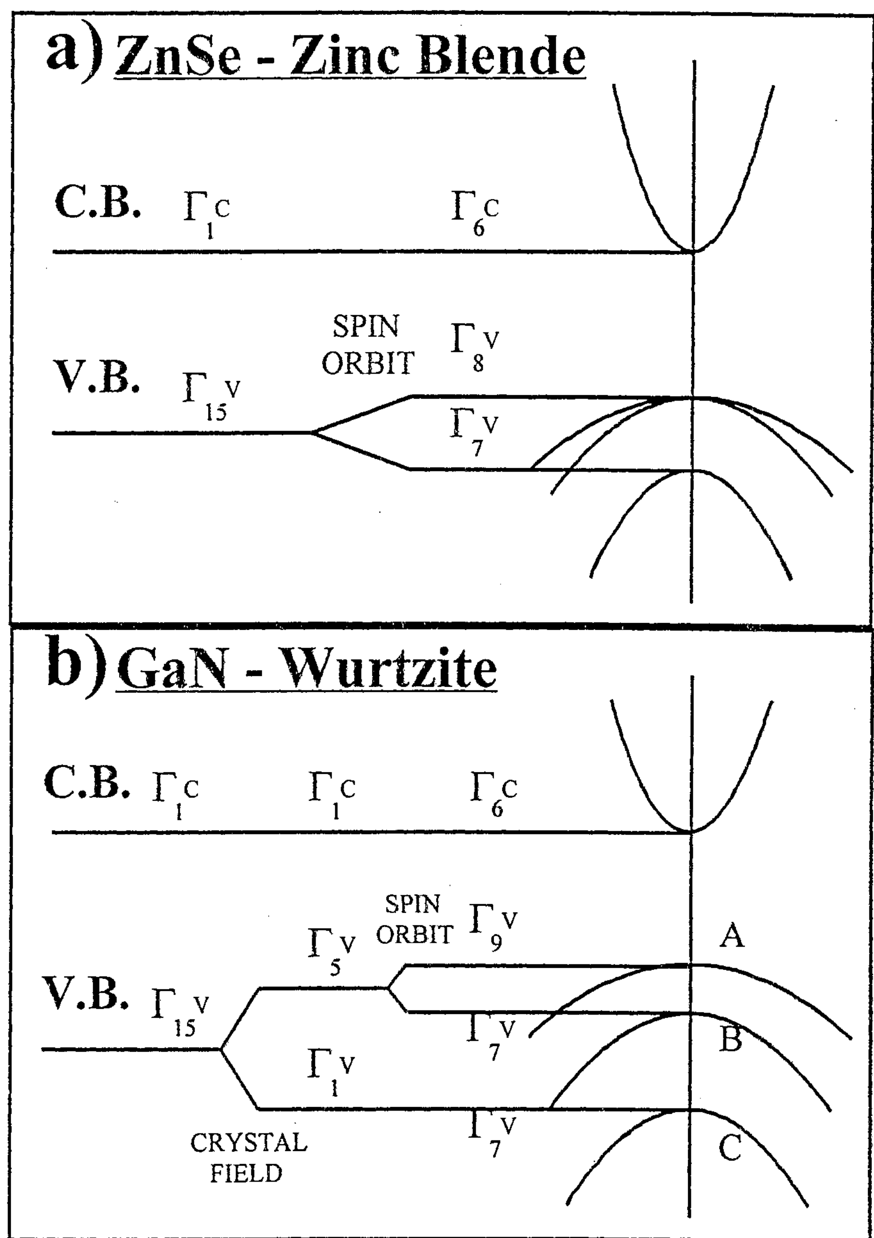

Figure 2. Fundmental bands of (a) ZnSe and (b) GaN near the Γ point for the conduction band (C.B.) and valence bands (V.B.). Note the additional splitting of the valence band for GaN due to crystal field splitting.

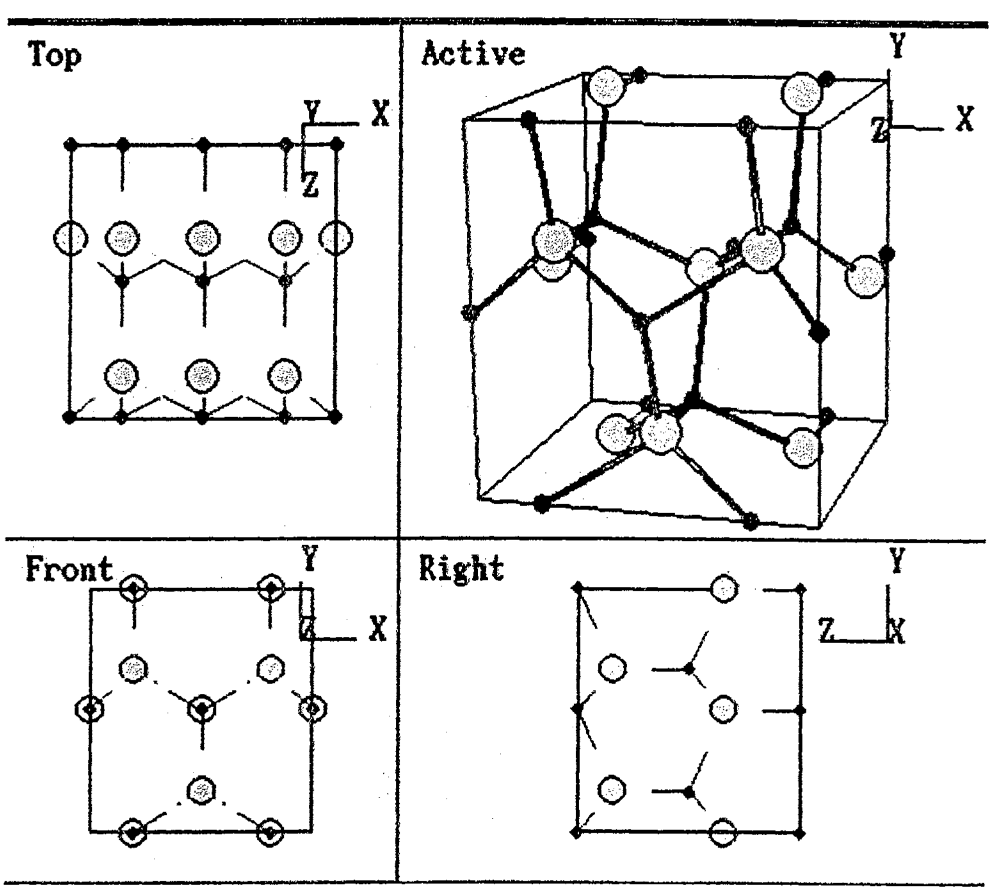

Figure 3. Diagram of the wurtzite crystal structure. [11]

from one atom to the next transferring energy around the crystal. Localized atomic wave functions are used to theoretically described Frenkel excitons. The excitons in alkali halide materials such as KBr and KCl are well described by the Frenkel exciton formalism [7].

The second type of exciton is referred to as Wannier-Mott exciton or simply as a Wannier exciton. Fig. 4 shows a schematic representation of both the Frenkel and the Wannier excitons. Wannier excitons are characterized as having relatively weak exciton binding energies so that the exciton and hole are separated from each other by a comparatively large distance in the crystal. In order for an exciton to be considered a Wannier exciton it must have an excitonic radius which extends over many lattice periods of the crystal. Wannier excitons are described by extended wave functions which average out the effects of individual lattice sites and treat the intervening space as being relatively good or bad at screening the coulomb interaction between the electron and the hole. In general, excitons that can be well described by the Wannier formalism, have to some extent or another covalent binding which places more electronic charge in the space between atoms compared to materials with ionic binding. Typically, the more covalent the bonds in a crystal, the weaker the attraction between the electron and the hole and the smaller the exciton binding energy. For example, GaAs has predominantly covalent bonds and has an excitonic binding energy of 4.2 meV while ZnSe has somewhat more ionic nature to the bonds and has an excitonic binding energy of about 20 meV. These generalizations do not hold true universally, but are good guidelines to keep in mind when discussing excitons in semiconductors. For ZnSe and GaN, the materials used in this study, excitons are well described by the Wannier formalism and for the rest of this work the term exciton will refer to a Wannier-Mott exciton.

In a pure material, excitons are free to move about the crystal transferring energy from one area to another. The Coulomb interaction between electron and hole results in completely correlated motion through the crystal. In the effective

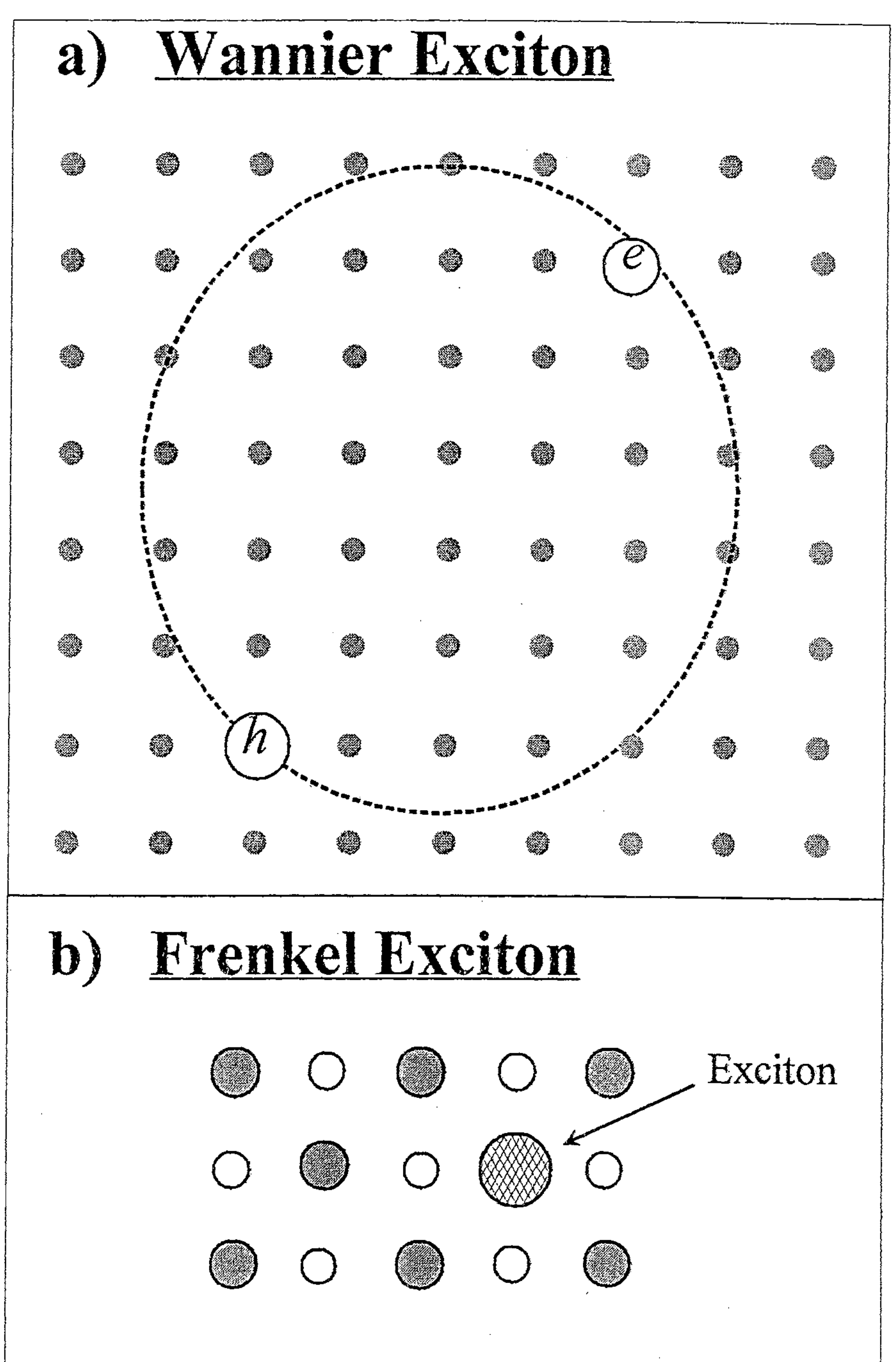

Figure 4. Schematic diagram of Wannier and Frenkel excitons. The Wannier exciton extends over many lattice sites while the Frenkel exciton is localized at one atom.

mass approximation, the total energy of the two-particle structure is given by:

$$E_K = E_n + \frac{\hbar^2 \mathbf{K}^2}{2\left(m_e^* + m_h^*\right)}, \tag{1}$$

where m_e^* and m_h^* are the effective masses of the electron and the hole, respectively, and $\mathbf{K}$ is the wavevector of the exciton. E_n is an energy that is a solution to the Hydrogen equation and is given by:

$$E_n = \frac{-e^4 \mu}{2\left(4\pi\hbar\epsilon\right)^2 n^2}, \tag{2}$$

where n is an integer, ϵ is the static dielectric constant, and μ is the reduced effective mass given by:

$$\frac{1}{\mu} = \frac{1}{m_e^*} + \frac{1}{m_h^*}. \tag{3}$$

As mentioned above, free excitons have a series of excited states which are similar to the excited states of the hydrogen atom with the ionization continuum corresponding to the bottom of the conduction band. Due to the presence of excitons, the lowest energy absorption occurs at discrete energy levels below the band gap E_g which are given by:

$$E = E_g - \frac{E_b}{n^2}, \tag{4}$$

where E_b is the binding energy of the exciton. This binding energy can then be written as:

$$E_b = \frac{e^4 \mu}{2\left(\hbar\ \epsilon\right)^2} = \left(\frac{\mu}{\epsilon\ ^2 m_e}\right) \cdot 13.6\ \text{eV}, \tag{5}$$

which is just the amount of energy required to ionize an electron into an unbound electron and hole. Note that 13.6 eV is the binding energy of an electron to the hydrogen atom in the ground state. Thus, we can see that the exciton binding energy, in this simple model, can be expressed as the binding energy of a hydrogen atom scaled by the reduced effective mass and the dielectric constant. The effective masses are parameters which describe the curvature of the bands at the zone center. They can be thought of as correcting for the fact that the electrons and holes are not free particles but are moving in a crystal. Similarly, the dielectric constant, ϵ, is a macroscopic parameter which describes how easily an electric field can penetrate

the crystal lattice. The simplest way to determine the excitonic binding energy of a material is to calculate it from the effective masses and dielectric constant. For GaAs, using parameters of $m_e^* = 0.07\ m_e$, $m_h^* = 0.5\ m_e$, and $\epsilon = 13.13$ [7], an exciton binding energy of 4.7 meV can be calculated which is close to the measured value of 4.2 meV. Similarly, for ZnSe, using parameters of $m_e^* = 0.17\ m_e$, $m_h^* = 0.75\ m_e$ [17], and $\epsilon = 9.1$ [10], an exciton binding energy of 22.7 meV can be calculated which is slightly larger than the measured value of 20 meV. Based on the simplicity of the model, it is amazing that these numbers agree as well as they do. In general, more careful calculations are required for an accurate prediction of the exciton binding energy for a given material. The Bohr radius of an exciton can be represented in a similar manner as:

$$a_B = \frac{\epsilon\,\hbar^2}{\mu e^2} = \left(\frac{\epsilon\, m_e}{\mu}\right) 0.053\ nm. \tag{6}$$

Using the parameters listed above, an excitonic Bohr radius of 11.3 nm can be calculated for GaAs, and a value of 3.5 nm can be calculated for ZnSe. Fundamental absorption at the excitonic resonance will be discussed in the next chapter.

CHAPTER III

GaN ABSORPTION

Introduction

Absorption is one of the most fundamental optical measurements that can be performed on a semiconductor. Absorption measurements have been performed in virtually every semiconductor including Si [18], Ge [19], GaAs [20,21], CdS [22,23], ZnSe [17] and GaN [24]. The experiment consists of sending light from a tunable light source into a semiconductor and measuring the transmitted light as a function of incident photon energy. For low excitation densities, the intensity of the transmitted light is given by:

$$I_t = I_0 \exp\left(-\alpha L\right),$$

where I_0 is the incident light intensity, L is the sample thickness, and α is the absorption coefficient. At low carrier densities α changes very little with carrier concentration. However, as the carrier density increases, the amount of absorption can increase or decrease depending on the experimental conditions. Absorption saturation and recovery will be discussed in Chapter 7. In this chapter, we will discuss absorption measurements performed on epilayers of GaN grown on sapphire substrates.

As mentioned in the introduction, GaN is an extremely promising material for a wide variety of technologically important applications such as Blue/UV light emitters, high temperature electronics, and solar-blind UV detectors. Although CW operation of an InGaN laser diode has already been demonstrated, fundamental studies of the optical properties of GaN are still important in order to understand the carrier dynamics in GaN. This information will hopefully will lead to new device applications and to the improvement of existing devices.

Due to the high absorption coefficient of GaN, mainly experiments such as photoluminescence (PL), reflection, and photoreflectance (PR), have been performed [25–31], while few transmission experiments have been performed [24,32,33]. Excitons were first observed in GaN absorption data by Dingle et al. [24] in 1971. Amano et al. [32] also published room temperature GaN absorption data which showed one broad excitonic peak. More recently, Manesreh [33] was able to resolve two excitonic features in 13 K GaN absorption data. The lowest energy peak was identified as due to a bound exciton. In this chapter, the result of a very careful series of absorption measurements will be discussed. Excitons are shown to be present in GaN for temperatures well above room temperature. Excitonic transitions associated with the three fundamental valence bands have been observed and the excitonic linewidth is studied as a function of temperature from 10 K up to 475 K.

The samples used in this study were high quality epilayers of GaN with thicknesses 0.2, 0.38, 0.5, and 0.8 μm which were grown by metalorganic chemical vapor deposition on (0001) sapphire substrates. The measurements were performed using a Xe arc lamp dispersed by a 0.5 meter spectrometer and a phase sensitive detection system comprised of a photomultiplier tube, an optical chopper, and a lock-in amplifier system. The experimental set up is shown in Fig. 5. For the temperature range from 10 to 325 K, the samples were mounted on a copper cold finger in a closed-cycle He refrigerator. For temperatures above 325 K, the samples were mounted in an oven capable of temperatures as high as 500 K.

General features of absorption

As described in Chapter 2, the Coulomb interaction between electrons and holes leads to the formation of excitonic resonances with a series of discrete hydrogen-like bound energy levels. The Coulomb interaction also affects unbound electrons and holes. Without the Coulomb interaction, the absorption edge in a semiconductor would have a simple square root dependence of the form $\alpha(\hbar\omega) \sim \sqrt{E_g - \hbar\omega}$ for photon energies larger than E_g. However, due to the Coulomb interaction, electron hole pairs with energies great than E_g are still correlated. This electron-hole

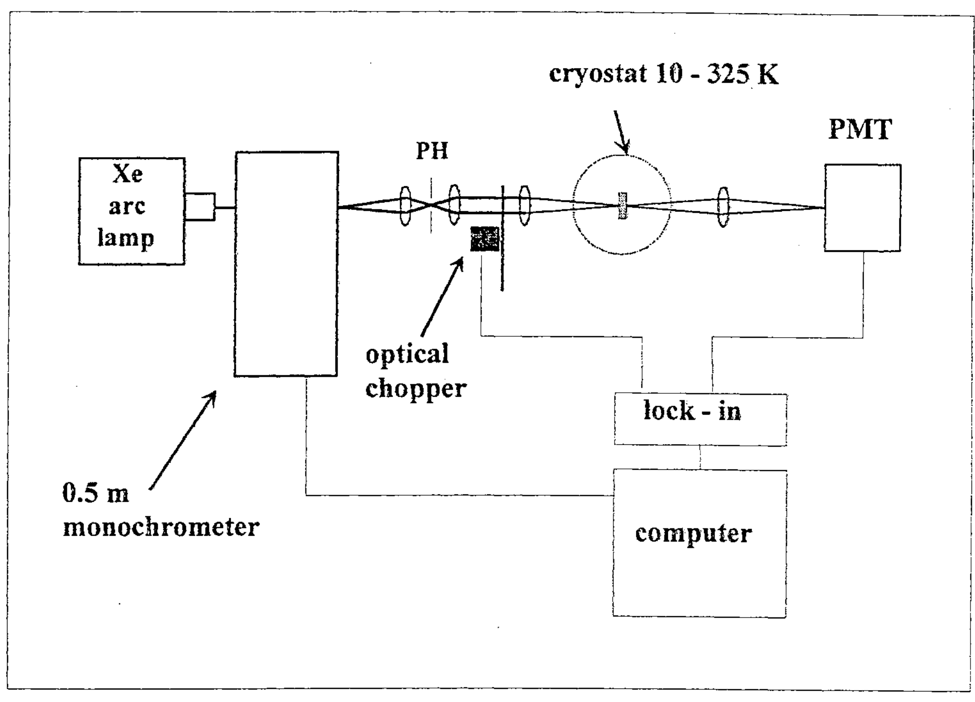

Figure 5. Diagram of the experimental set up used for absorption measurements.

correlation above the gap leads to increased absorption above the gap and to a substantial deviation from a simple square root dependence on energy. R.J. Elliot [15] was the first to calculate the absorption spectra of a semiconductor in the effective mass approximation. The Elliot equation for absorption in a semiconductor is given by [15,34]:

$$\alpha(\omega) = \alpha_0^{3D}\left(\frac{\hbar\omega}{E_b}\right)\left[\sum_{n=1}^{\infty}\left(\frac{4\pi}{n^3}\cdot\delta\left(\Delta+\frac{1}{n^2}\right)\right)+\Theta(\Delta)\frac{\pi\exp\left(\frac{\pi}{\sqrt{\Delta}}\right)}{\sinh\left(\frac{\pi}{\sqrt{\Delta}}\right)}\right] \tag{7}$$

where $\Delta = (\hbar\omega - E_g)/E_b$, $\Theta(\Delta)$ is the Heavyside function, and the binding energy E_b is given by:

$$E_b = \frac{e^4\mu}{2(\hbar\,\epsilon)^2}. \tag{8}$$

α_0^{3D} is given by:

$$\alpha_0^{3D} = \frac{\pi|d_{cv}|^2}{\hbar nc}\left(\frac{1}{2\pi a_B}\right)^3, \tag{9}$$

where d_{cv} is the momentum matrix element at the zone center, n is the index of refraction, and a_B is the excitonic Bohr radius given by:

$$a_B = \frac{\epsilon\,\hbar^2}{\mu e^2}. \tag{10}$$

The first term in the Elliot equation (Eq. (7)) models the bound excitonic resonances as an infinite sum of delta functions. In practice, one must assume some sort of broadening for the excitonic resonance in order to fit real absorption data. The second term in Eq.(7) represents absorption above the band gap and contains the contribution from electrons and holes correlated via the Coulomb interaction. We will fit the 10 K absorption data to this equation later in this section in order to see how closely our data fits this simple theory. Absorption data from GaN will now be presented.

As shown in Fig. 6, the low temperature absorption data are dominated by sharp excitonic resonances. Since, for low impurity concentrations, bound excitons are not expected to contribute significantly to band edge absorption, the two lowest energy peaks are attributed to absorption at the A and B free excitonic transitions. Recently, Manasreh [33] published absorption data showing two peaks where the

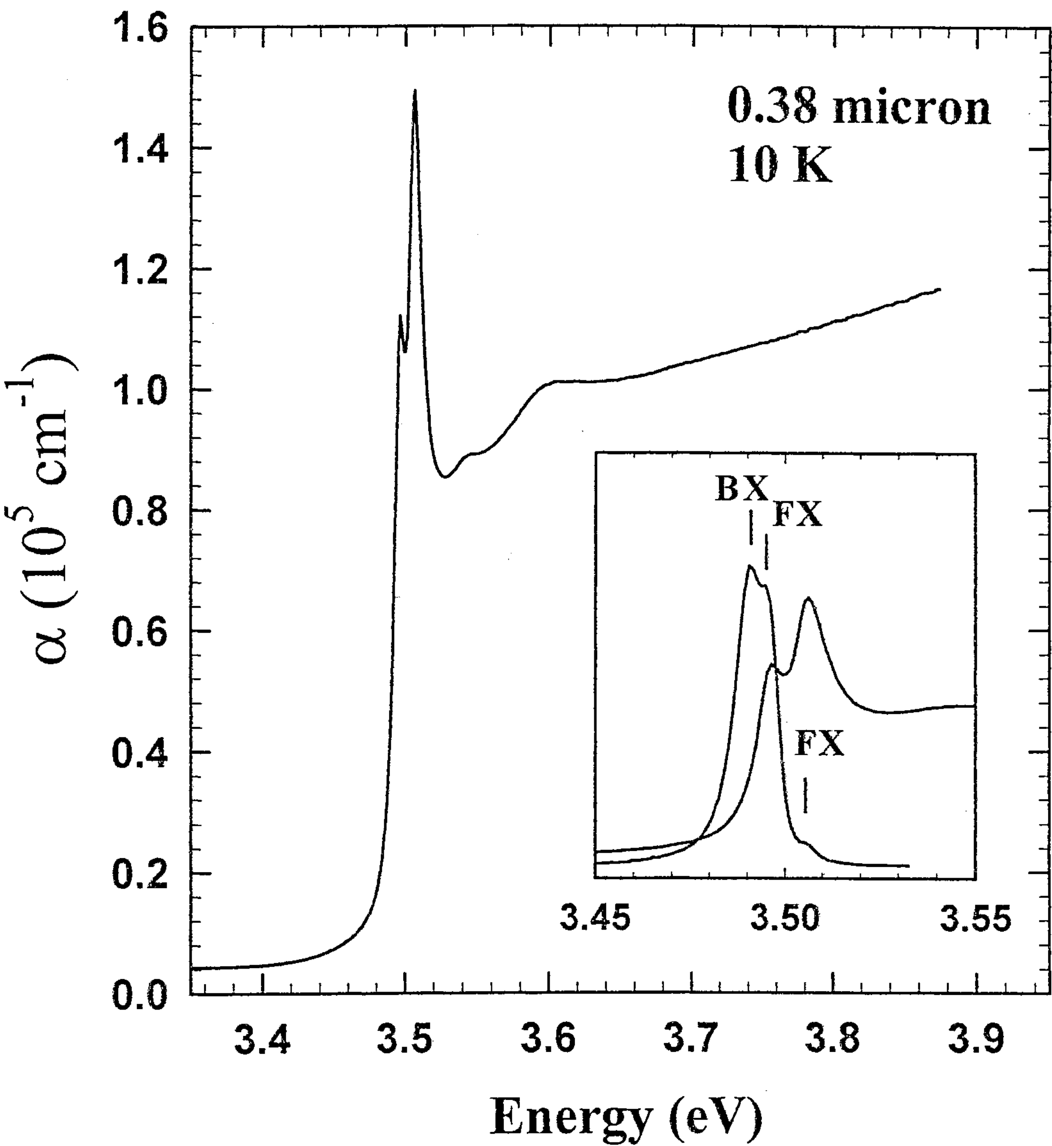

Figure 6. Absorption spectrum at 10 K of a 0.38 micron thick epilayer of GaN. The inset shows absorption in a narrower region near the band gap together with CW photoluminescence data.

lowest energy feature was tentatively identified as bound exciton absorption. The inset of Fig. 6 shows PL data together with the absorption spectrum. It is known from temperature dependent PL measurements of high quality GaN epilayers [25] that the lowest energy peak in PL is due to a bound exciton and the two higher energy features are due to free excitons. The two lowest energy absorption features match up well to the A and B free exciton resonances in PL, while the PL bound exciton peak is shifted to lower energy. If the lowest energy absorption peak were due to impurity absorption, one might expect to see a change in the absorption value from sample to sample depending on the impurity concentration. The relative absorption strength of the two lowest energy features is about the same for all of our samples (see Fig. 2). This apparent difference in oscillator strength is most likely due to band tailing states which raise the net absorption at the B exciton more than at the A exciton. For the above reasons, we have identified the two lowest energy features as absorption at the A and B free excitons.

Fig. 7 shows polarization dependent absorption data for the 0.38 μm thick sample. For these measurements, a pair of prisms was used in order to create a small component of the electric field which was parallel to the GaN c-axis. A comparison of the two curves shows an increased absorption for the feature at 3.546 eV. Since the C exciton is theoretically allowed only for E || c, the feature at 3.546 eV is identified as due to the C exciton. Similar polarization dependent measurements have been performed to identify the C exciton in PR data [30].

Fig. 8 shows the absorption spectrum for samples of four different thicknesses at 10 K. The A and B excitons can easily be observed in all samples, while features due to the C exciton can be observed only in the thicker samples. For the 0.8 μm sample, an absorption feature at 3.528 eV is observed as well as the C exciton peak at 3.544 eV. This peak is most likely due to absorption from the A band continuum states which gives an A exciton binding energy of 22 meV which is in good agreement with recent PR measurements [26]. For samples thicker than 1 μm, no excitonic resonance was observed in absorption. This is probably due to the large absorption coefficient of GaN and the experimental difficulty of detecting a very small

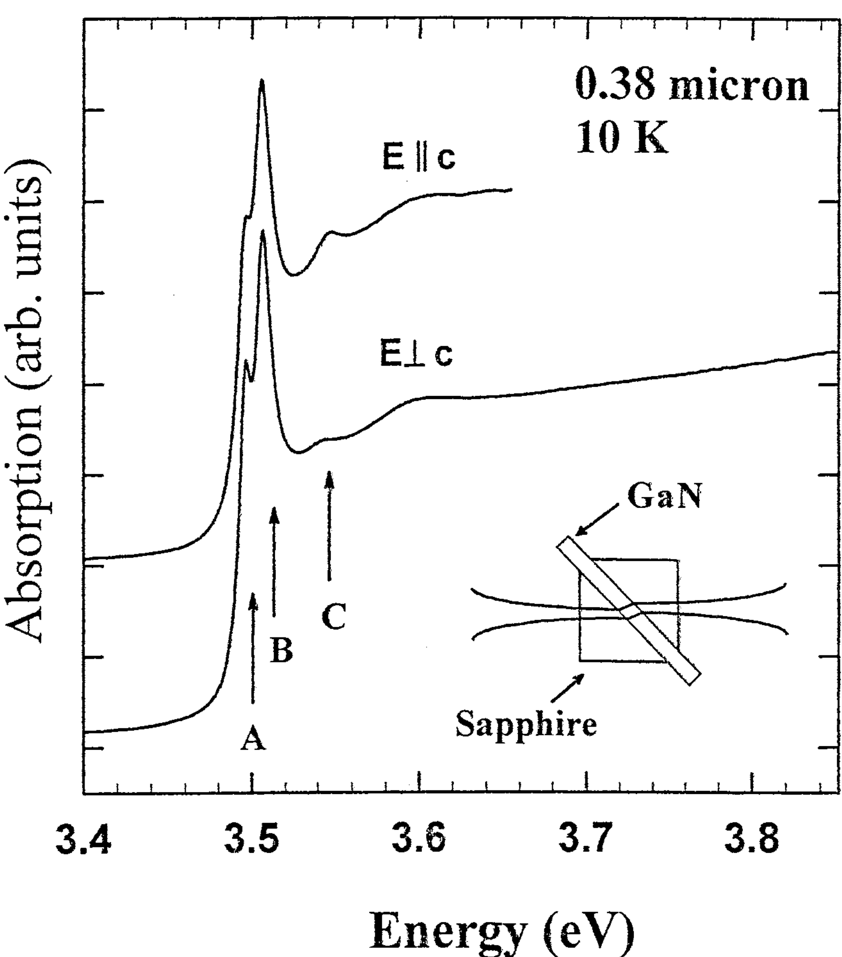

Figure 7. Absorption spectra for two different polarization geometries. The bottom curve show absorption data where the electric field of the incident light is perdendicular to the GaN c-axis. The top curve shows absorption where a pair of prisms has been used to couple light into the sample so that there is some light with its electric field parallel to the GaN c-axis. The inset shows the prisms used to coupled the light into the sample.

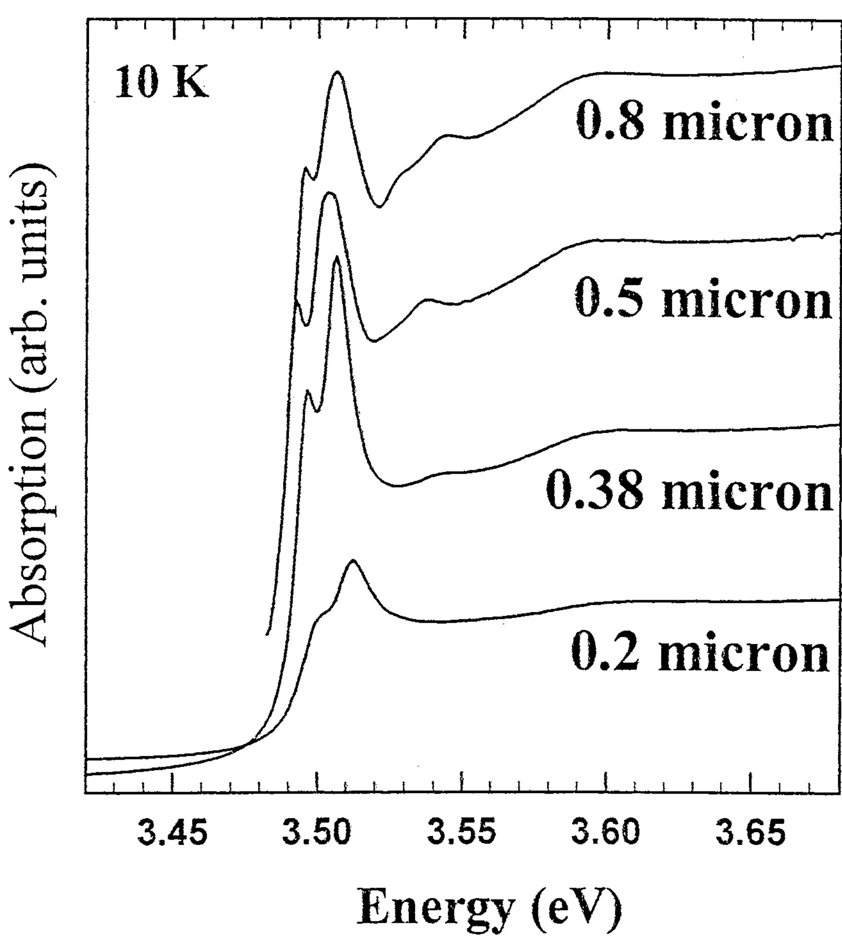

Figure 8. Absorption spectra at 10 K taken from samples of four different thicknesses. The positions of the excitonic resonances shift around slghtly due to differences in residual strain caused by differences in lattice constants and coefficients of thermal expansions between the sample and the substrate.

transmitted signal while suppressing luminescence from the sample. Luminescence is lower in energy than the fundamental absorption so that it can easily pass through the sample causing a background to the transmitted signal intensity. The energy positions of the excitonic resonances also shift around slightly from sample to sample. This is due to the differences in lattice constants and coefficients of thermal expansion between the sample and the substrate. Because these samples were grown at very high temperature ($\approx$ 1000 C), the samples can form dislocations and defects as they are cooled from this high temperature down to room temperature. Transitions associated with the three fundamental valence bands of GaN have been identified. However, there is one more broad feature at 3.6 eV which will be discussed in the next section.

It is interesting to compare the experimentally measured absorption data to the absorption lineshape predicted by the Elliot equation (Eq. (7)). Fig. 9 shows a fit of the absorption data from the 0.38 μm sample to the Elliot equation. The experimental data is given by the solid line while the fit is given by the dashed line. The data were fit assuming the three fundamental bands associated with the GaN A, B and C bands. The exciton resonances were assumed to have Lorentzian broadening. The band edge was artificially broadened by multiplying the second term in Eq.(7) by the Fermi-Dirac population equation to simulate broadened band edge. Representative exciton and band edge components of the fit are given by the dotted line in Fig. 7. The data do not fit well below the exciton resonance due to the presence of band tailing states. Even when the broadening parameter is made large the data cannot fit the low energy absorption shape. These band tail states have been shown to have an exponential energy dependence over a small energy region just below the band gap. A more complete theory including disorder and defects might be able to fully model this absorption data including band tail states. It should be noted here that this is not a particularly good method of fitting the experimental data due to the large number of fitting parameters. Five parameters are needed for each band plus a constant to account for reflection losses below the band gap. The five parameters are as follows: energy gap, exciton binding energy, exciton amplitude,

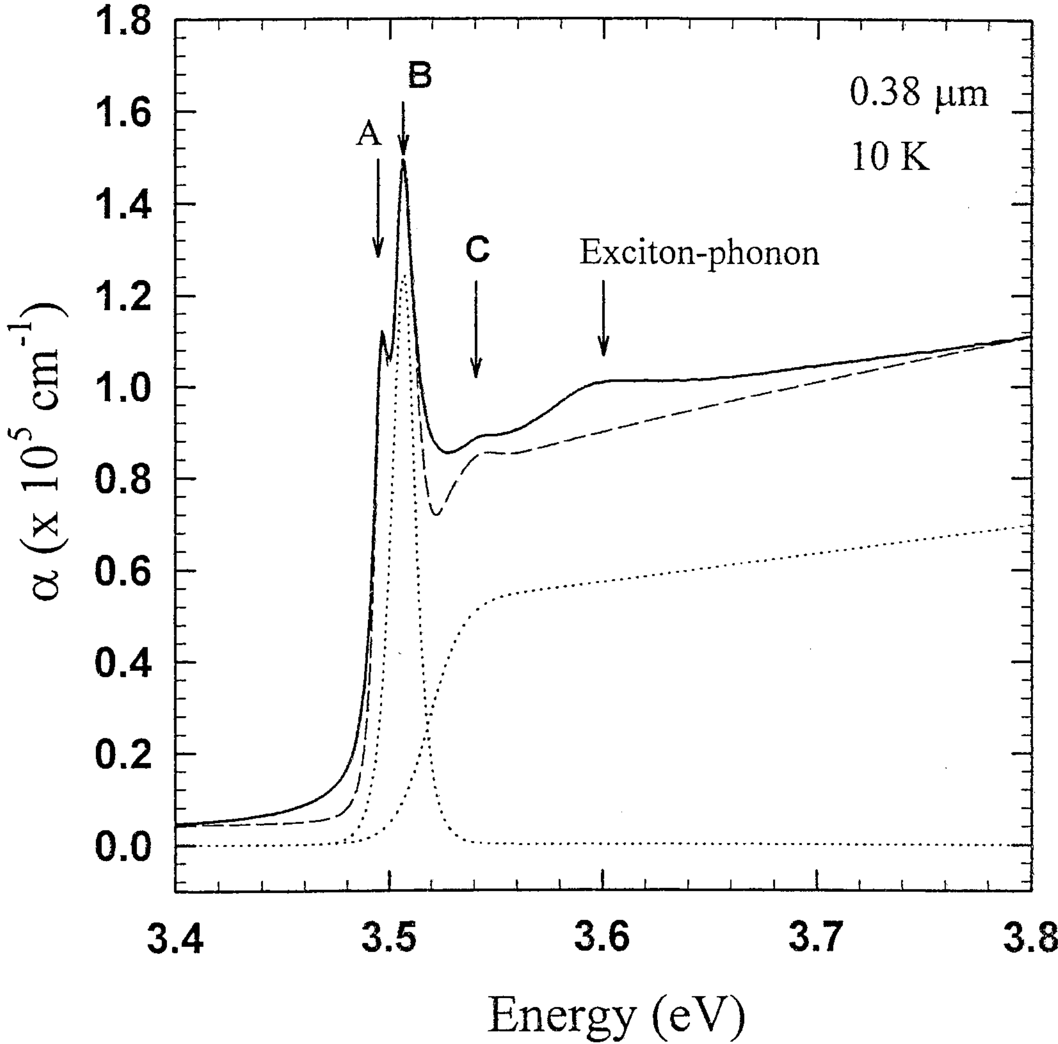

Figure 9. Fit of the 10 K absorption data from the 0.38 μm sample to the Elliot equation assuming three bands. The experimental data is the solid line while the fit is given by the dashed line. The excitonic and band edge contributions to the fit from the B exciton are shown as dotted lines.

exciton broadening, and band edge broadening. Thus, this could be up to a 16 parameter fit. The fit is included here only to show that the data can be fit using reasonable parameters. A value of 23 meV was found to work well for the exciton binding energy which is close to the value of 21 meV from photoreflectance data. Note also that there is a feature at 3.6 eV which cannot be fit with the Elliot equation assuming three fundamental bands. This feature is due to indirect absorption in a process where an exciton and an LO phonon are created simultaneously from a photon of energy 3.6 eV. This process will be discussed in the next subsection.

Phonon-Assisted Absorption

The absorption curves shown in Fig. 6 and Fig. 8 show an additional broad feature at about 3.6 eV. This feature is due to a strong exciton-LO phonon interaction in a phonon-assisted absorption process where a photon of energy 3.6 eV simultaneously creates an exciton and an LO phonon. The energy spacing between the band edge excitons and this 3.6 eV feature is only slightly larger than the 91.7 meV LO phonon energy of GaN.

Theoretical calculations for CdS predict this indirect absorption process to be as much as 10% of the direct band edge absorption and should reach its maximum at an energy position which is slightly larger than one LO phonon energy above the excitonic absorption resonance [35]. The calculation uses second order perturbation theory within the effective mass approximation to calculate the probability of a transition from an initial state containing the crystal in the ground state and a photon to a final state containing an exciton and an LO phonon. The theory considers only single LO phonon scattering. Fig. 10 shows the calculated absorption probability for this process. The curve for CdS was reproduced from Eq.(4) of Ref. [35]. The curve for GaN was calculated in a similar manner except that the following parameters were used: $m_e^* = 0.2\ m_e$, $m_h^* = 0.8\ m_e$, $E_{ph} = 91\ meV$, and $E_b = 28\ meV$. Note that the x-axis is in units of LO phonon energy. The maximum absorption for this process for both materials occurs at slightly larger than 1 LO phonon energy above the excitonic resonance. For GaN, the maximum indirect absorption occurs at 115 meV

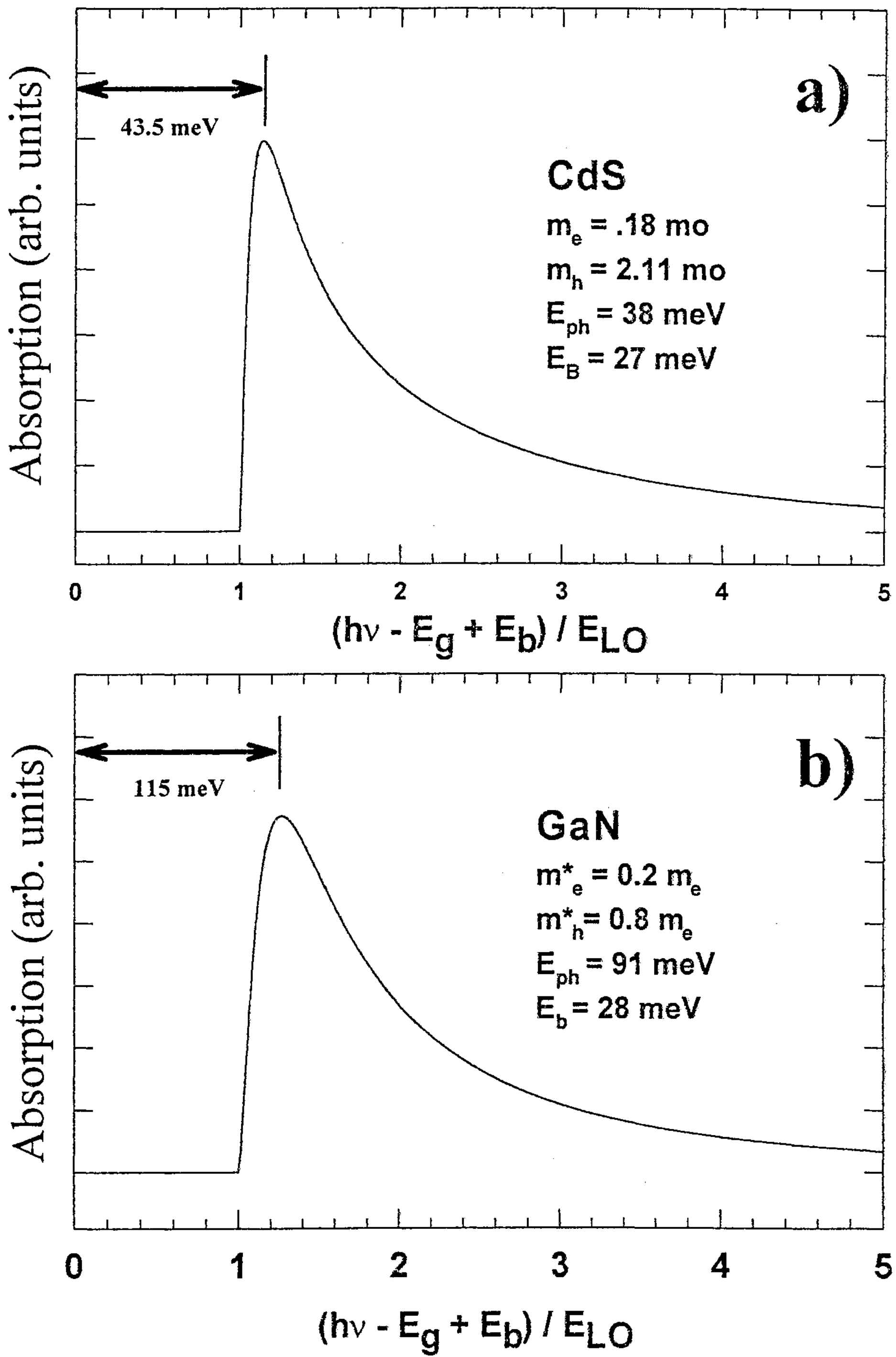

Figure 10. Calculation of indirect exciton absorption for (a) CdS and (b) GaN. Note that the units of the x-axis are in LO phonon energies. The absorption due to this indirect process peaks at slightly larger than 1 LO phonon energy above the excitonic resonance.

above the excitonic resonance. This is very close to that value of 100 meV observed experimentally. Considering the broad nature of the peak in the GaN absorption data at 3.6 eV and the fact that all three fundamental bands can contribution to this process, the data presented here are consistent with the interpretation that this feature is due to indirect absorption.

This absorption process has been observed experimentally in CdS where the polar nature of this material is known to give rise to strong exciton-LO phonon coupling [23]. Since the Ga-N bond is more polar than for other III-V semiconductors, such as GaAs, the large exciton-phonon interaction observed here may be a result of the polar nature of GaN. The recent observation of multiphonon resonant Raman scattering up to the fourth order [36] and of a large number of phonon replicas in PL and PL excitation data [37] both indicate that GaN is a polar material exhibiting strong exciton-LO phonon coupling.

Temperature Dependence

Fig. 11 shows temperature dependent data for the 0.38 μm sample from 100 K to 475 K. The data clearly show an excitonic resonance at 300 K and, in fact, excitons still contribute even at the highest temperatures in this study. The peak separation between the A and B exciton transitions was found to be 9.9 meV for temperatures below 150 K. Since above 150 K the two peaks are broadened together and there is no appreciable change in the peak separation from 10 K to 150 K, it is assumed that the A and B excitons have the same temperature dependence. The absorption spectrum at each temperature was fit to a double-Lorentzian functional form where the spacing between the peaks was fixed to 9.9 meV and it was assumed that the A and B excitons have the same broadening. The free carrier contribution to the absorption was modeled using a broadened 3-dimensional continuum [38]. Fig. 12 (a) shows the A exciton energy position as a function of temperature along with a fit to the Varshni equation which is given by [39]:

$$E(T_L) = E(T_L = 0) - \frac{\alpha \cdot T_L^2}{(\beta + T_L)} \tag{11}$$

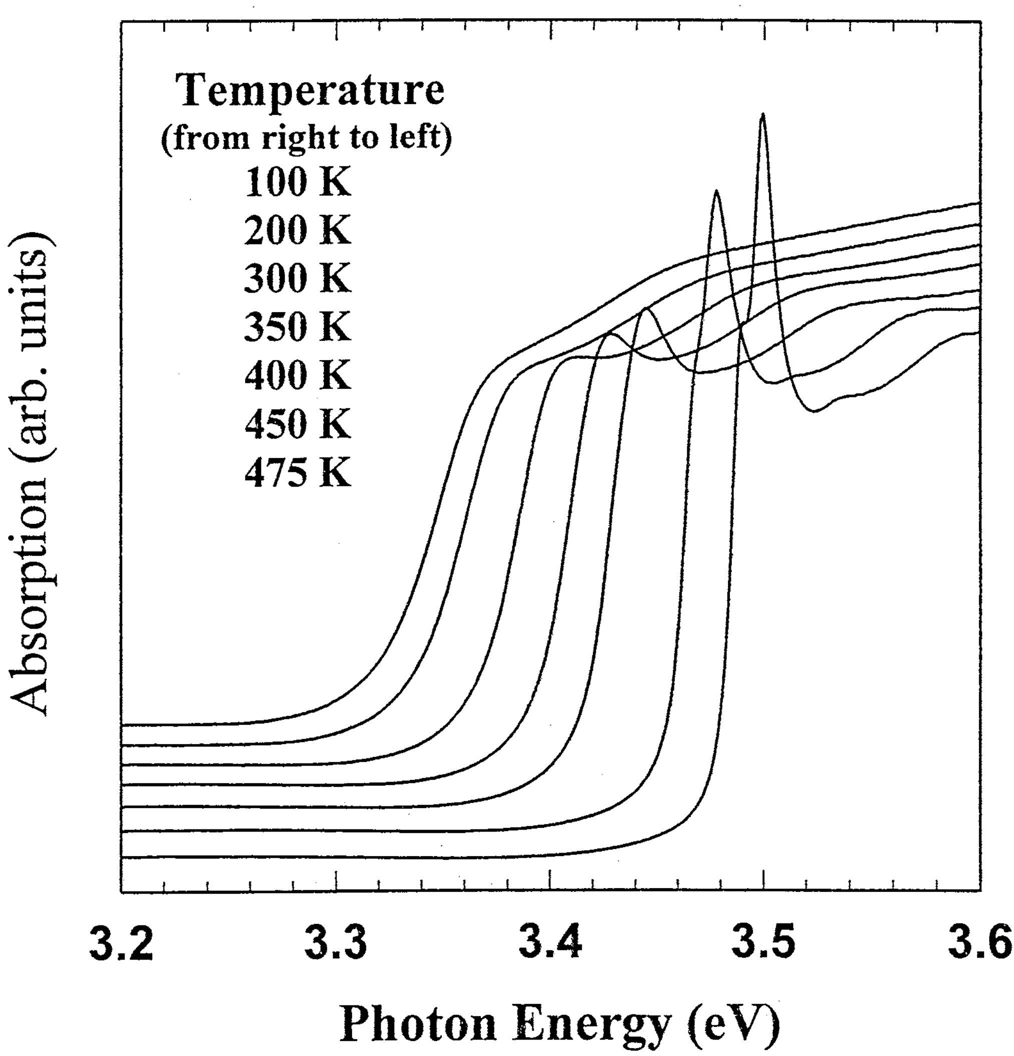

Figure 11. Absorption spectra for temperatures from 100 K to 475 K. Excitonic resonances are clearly visible at room temperature as well as above room temperature. The spectra have been vertically displaced for clarity.

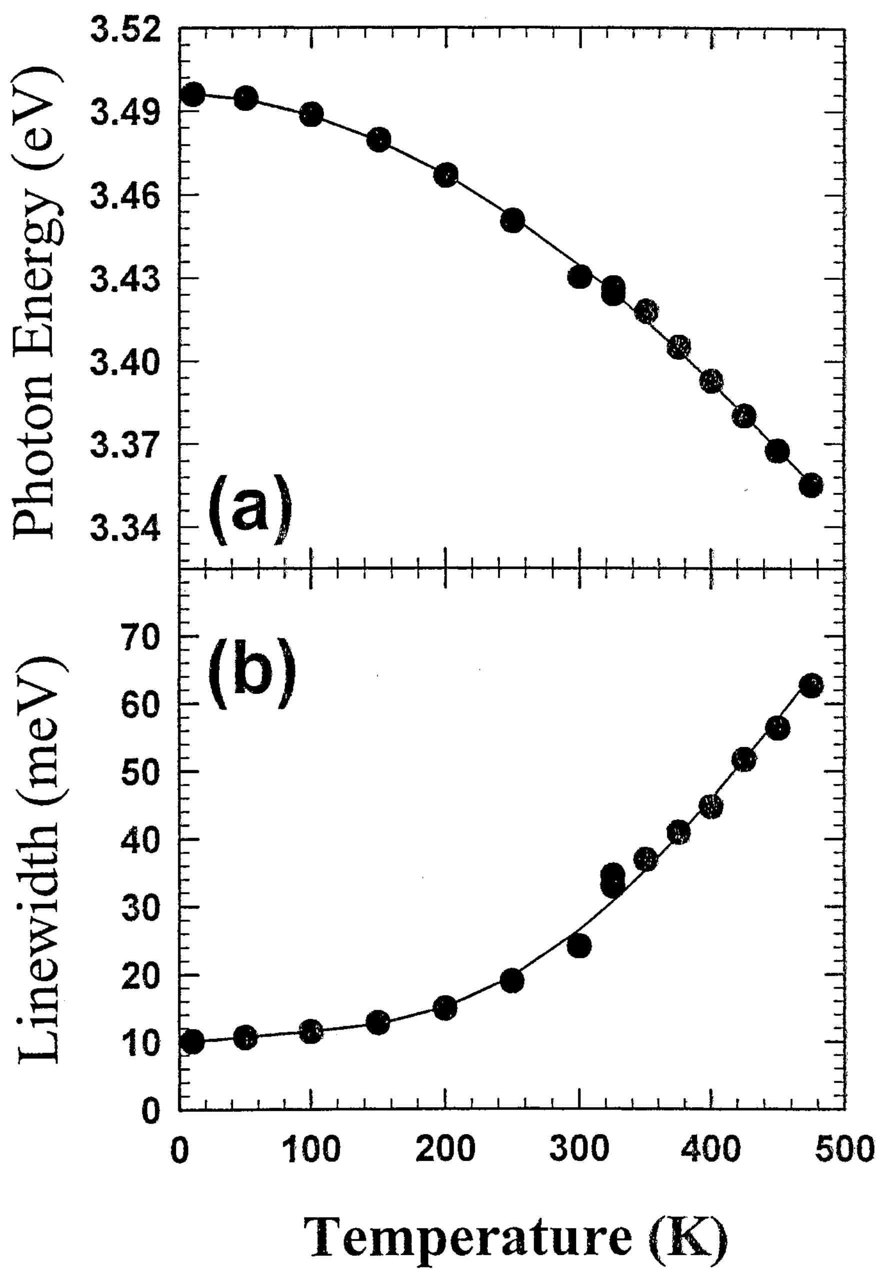

Figure 12. Exciton peak energy position (a) and broadening (b) shown as a function of temperature. The solid line in (a) is a fit to the Varshni equation while the solid line in (b) is a fit to the phonon brodening equation (see text).

where T_L is the lattice temperature and the best fit is given by α = 11.8 x 10-4 eV/K and β = 1414 K. These values are in good agreement with previous values determined from PR measurements [27].

Fig. 12 (b) shows the exciton broadening as determined from the fit to a double-Lorentzian function. The solid line represents a fit to the following phonon broadening equation [40]:

$$\Gamma(T_L) = \Gamma_0 + \gamma_{ph} \cdot T_L + \frac{\Gamma_{LO}}{\left[\exp\left(\frac{E_{LO}}{k_B T_L}\right) - 1\right]} \tag{12}$$

where Γ_0 represents temperature independent scattering, γ_{ph} represents exciton-acoustic phonon interaction, Γ_{LO} represents exciton- LO phonon broadening, and E_{LO} is the LO phonon energy (91.7 meV). The best fit yields the parameters $\Gamma_0 = 10$ meV, $\gamma_{ph} = 15$ meV/K, and $\Gamma_{LO} = 375$ meV full-width-at-half-maximum (FWHM). For GaAs, $\gamma_{ph} = 4.6$ meV/K and $\Gamma_{LO} = 14$ meV (FWHM) [40] and, for ZnSe materials, $\gamma_{ph} = 11$ meV/K and $\Gamma_{LO} = 80$ meV (FWHM) [41]. Compared to these values, the exciton-LO phonon broadening parameter obtained for GaN is extremely large. The much larger value of Γ_{LO} for GaN should in part be due to the much larger E_{LO} of GaN in comparison to ZnSe (92 vs 30 meV).

Recent linewidth analyses of excitons in GaN performed using other experimental techniques also report large exciton-phonon interaction [28,31,42]. FWM linewidth studies of GaN presented later in this thesis give a value of Γ_{LO} = 390 meV (FWHM) [43]. Chichibu et al. [28] analyzed their PL linewidth data by considering both the exciton-LO phonon interaction as well as interaction with the lower E_2 phonon which has an energy of 17.9 meV. We find that our data does not fit well to a broadening equation that includes the E_2 phonon contribution. The higher E_2 phonon population is offset by the fact that the E_2 phonon interacts only via the deformation potential interaction while the LO phonon interacts via both the deformation potential and the Fröhlich interactions.

In conclusion, temperature dependent absorption measurements have been performed which clearly show that excitons in GaN persist above room temperature. Sharp features have been observed near the band edge of GaN which are identified as

absorption at the 1s A and B excitons. The energy position of the C exciton was determined from polarization dependent measurements. The temperature dependence of the A and B excitons was derived from a fit to the Varshni empirical relation yielding thermodynamic coefficients of α = 11.8 x 10-4 eV/K and β = 1414 K. The broad absorption feature with a maximum at about 3.6 eV has been identified as an indirect absorption process where an exciton is created with the simultaneous emission of an LO phonon. Exciton broadening as a function of temperature also indicates that the exciton-phonon interaction in GaN is very large.

CHAPTER IV

COHERENT-TRANSIENT DEGENERATE FOUR-WAVE-MIXING: EXPERIMENT AND THEORY

Four-wave-mixing (FWM) is a general spectroscopic technique that can be used to study a wide variety of phenomena in solids, liquids and gases using excitation sources varying in time scales from continuous wave (CW) to the femtosecond regime. FWM, or laser-induced gratings, is comprehensively reviewed by Eichler [44]. FWM is said to be degenerate when both the pump and the probe beams have the same wavelength. In this study, only degenerate FWM is performed. Coherent-transient (CT)-DFWM, as the name implies, is a FWM technique used to measure the lifetime of a coherent state created via laser excitation. Coherence decay times, or dephasing times, are on the order of microseconds for gases while for semiconductors (and liquids), strong interaction with neighboring atoms produces dephasing times on the order of picoseconds or femtoseconds. The first section of this chapter will describe the important experimental details associated with performing CT-FWM. The second section will give a short theoretical description of CT-FWM based on a solution of the optical Bloch equations.

Experimental Considerations

In the past decade, many experimental investigations of dephasing times in semiconductors have been performed using CT-DFWM. These types of measurements were made possible, in part, due to recent advancements in picosecond and femtosecond laser systems. It has been shown that, for GaAs at low temperature (10

K), coherence times for free carriers are on the order of a 10's of femtoseconds [45], while excitons dephase a few picoseconds after excitation [46,47]. Researchers have also observed quantum beats, studied photon echoes, and have performed detailed measurements of semiconductor linewidths. CT-DFWM is one of the most reliable methods of measuring linewidths in semiconductors and gives a plethora of information on ultrafast interactions between excitons, phonons, and free carriers. The first part of this section will give the details of the experimental setup for CT-DFWM. The second part of this section will describe sample preparation techniques which are required in order to perform FWM on some samples.

Experimental Setup

The experimental set up used in this work is shown in Fig. 13. An Ar-ion laser is used to pump a Ti:Sapphire laser producing 100 femtosecond pulses which are tunable from 690 nm to 990 nm. A thin (0.5 mm) Lithium Barium Borate (LBO) crystal is used to create the second harmonic with a wavelength range from 345 nm to 495 nm. A beam splitter is used to spit the pulses in two, producing a weak probe pulse and a stronger pump pulse. As shown in the figure, two separate arms are created which have an equal optical path length from the beam splitter to the sample. An indexed optical delay line with 0.1 μm resolution is used to delay the probe with respect to the pump. The pulses are focused onto the sample and the scattered probe beam is measured using a slow detector such as a photomultiplier tube (PMT). In order to improve the signal to noise ratio, both the pump and the probe beam are chopped at a slightly different frequency and a lock-in amplifier is used to measure the signal at the difference frequency. A computer is used to advance the delay stage and to record the reading from the lock-in amplifier.

In order to perform CT-FWM, the laser pulses must be overlapped both temporally and spatially inside the semiconductor sample. Spatial overlap is achieved by focussing both beams onto a 50 μm pinhole so that both beams pass cleanly through the pinhole at their minimum beam waist. In order to determine the zero of the delay, autocorrelation was performed. When performing autocorrelation, one

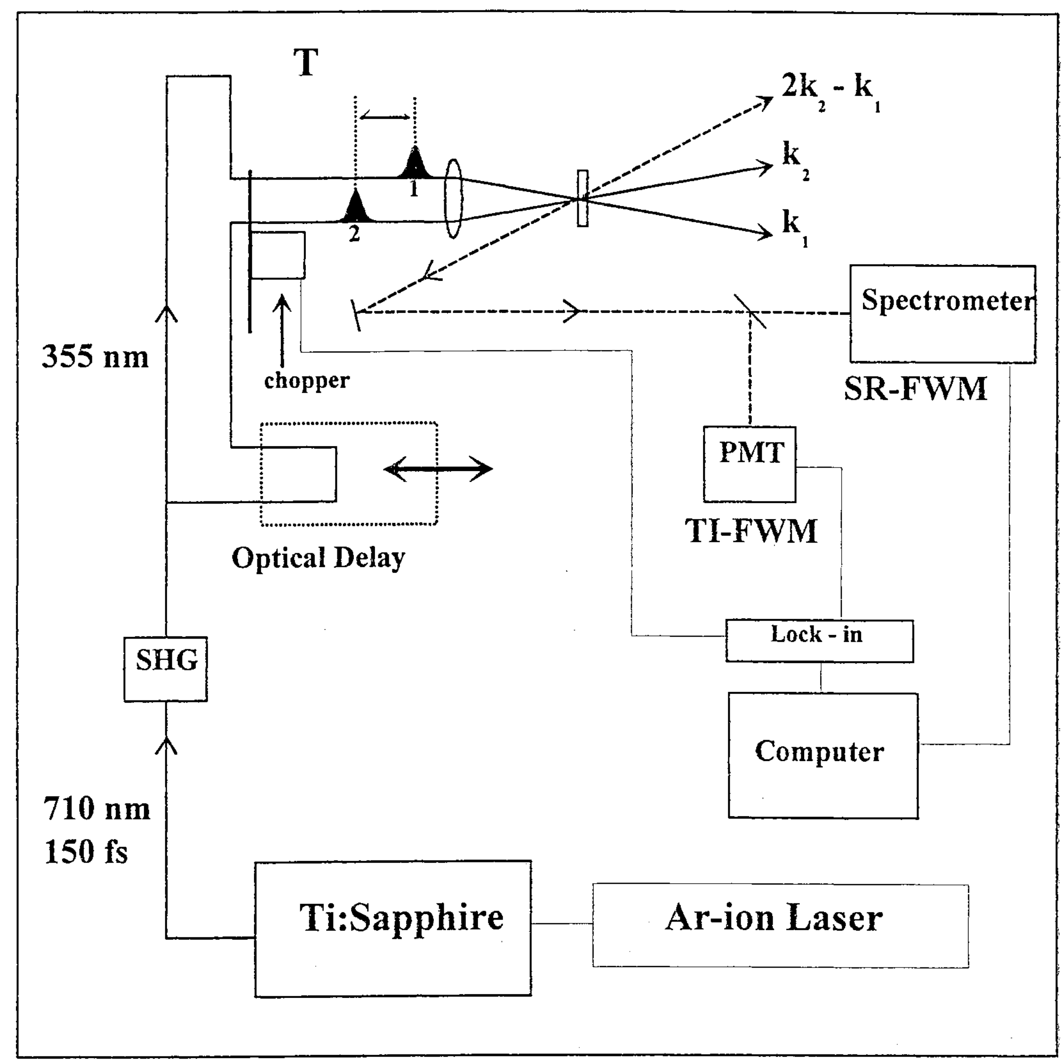

Figure 13. Coherent-transient degnerate four-wave-mixing (CT-DFWM) experimental set up. The second harmonic of 710 nm, 150 fs pulses from a modelocked Ti:Sapphire are used to resonantly excite the excitonic transition. The signal is generated in the reflection geometry in the phase-matched direction and measured as a function of optical delay between the two pulses in order to measure the time-integrated (TI)-FWM signal. Alternately, the energy spectrum of the signal at zero delay can be measured by sending the signal into a spectrometer to measure the spectrally-resolved (SR)-FWM signal.

focuses the spatially overlapped pulses onto a nonlinear crystal in order to create a non-collinear second harmonic (NCSH). The NCSH must be created using one photon from the pump and one photon from the probe. Thus, the NCSH only appears when the two laser pulses are overlapped in time. This is the basic nonlinear process used for autocorrelation of short laser pulses.

Once the pulses are overlapped both spatially and temporally, the sample is placed at the focus in the overlap region. The laser photon energy is then set to resonantly excite the excitonic transitions of the sample. The first laser pulse with wave vector $\vec{k}_1$ creates a coherent population of oscillators. A second laser pulse with wave vector $\vec{k}_2$, at a time T later and at a small angle with respect to the first, interferes with the polarization created by the first pulse. As long as the polarization created by the first pulse is in phase with the second laser pulse there will be radiation emitted coherently in the direction $2\vec{k}_2 - \vec{k}_1$. By varying the delay between the two pulses, we can measure how this third-order polarization decays over time. As described in more detail below, the decay of this third-order polarization is related to the dephasing time of the sample. This experiment is called time-integrated (TI) FWM as distinguished from an experiment called time-resolved (TR)-FWM where the actual evolution of the FWM signal is measured. The evolution of the FWM signal (TR-FWM) is not measured in this work. Although this nomenclature is roughly accepted now, many older papers refer to the experiment performed here as TR-FWM. The signal diffracted in the direction $2\vec{k}_2 - \vec{k}_1$ can also be directed into a spectrometer in order to perform spectrally-resolved (SR)-FWM. This experiment gives valuable information as to the origin of the FWM signal.

We should make a note here about the phase matching condition for this experiment. Due to the large absorption coefficient of semiconductors and hence the small skin depth, for this type of experiment, we are in a thin grating regime [44]. This means that the thickness of the grating created is less than or on the order of a wavelength of the exciting laser light. This is in contrast to a thick grating regime where Bragg type scattering is dominant. As shown in Fig. 14, the phase matching condition says that we must have $\Delta k = 0 = 2\vec{k}_2 - \vec{k}_1 - \vec{k}_{signal}$. Looking at

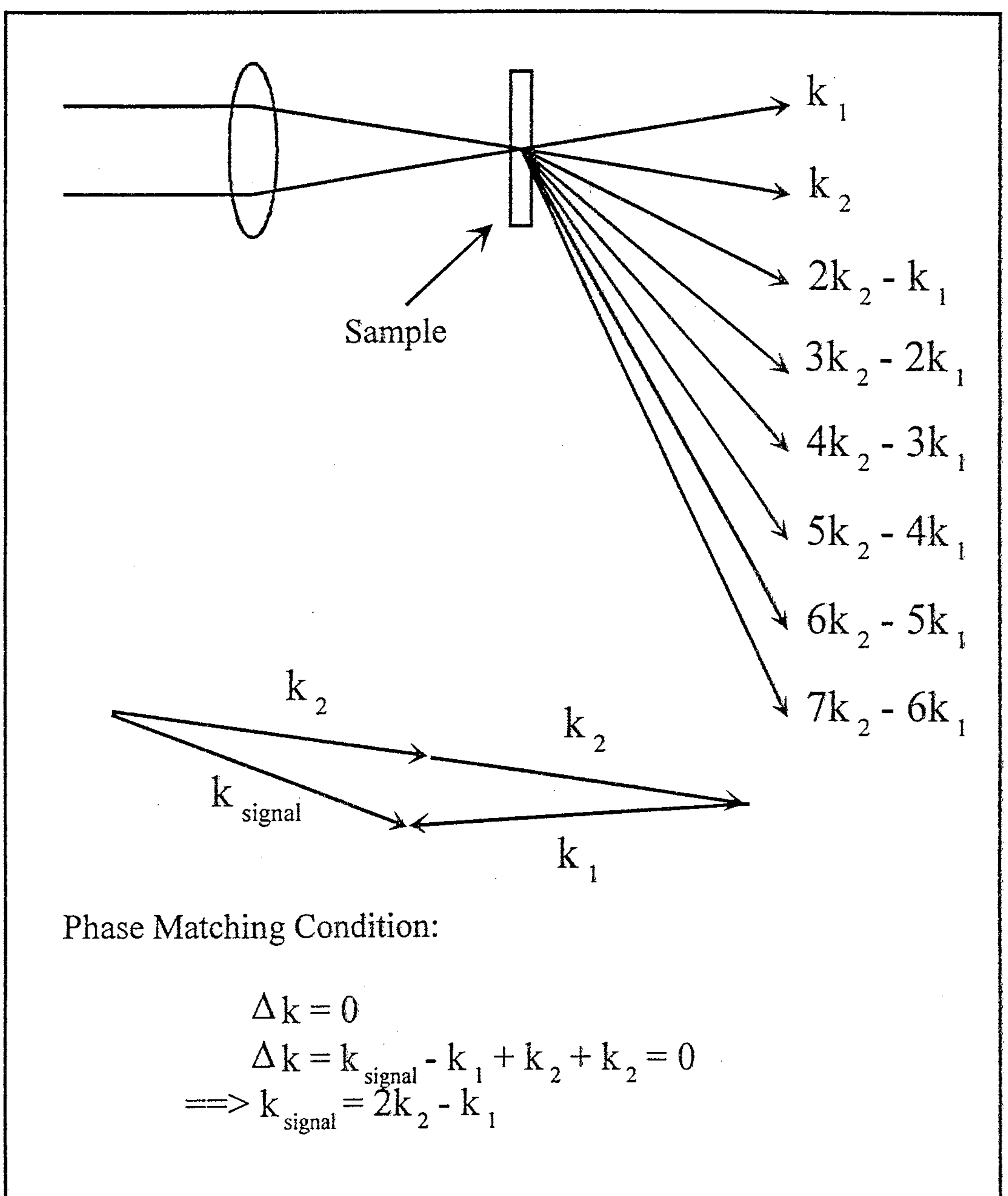

Figure 14. The light scattered into the direction $2k_2 - k_1$ is the normal four-wave-mixing signal. Higher order signals are also shown for the 5 th order througth the 13 th order. These higher order waving mixing siganls have been observed from ZnCdSe/ZnSe multiple quantum well samples.

the diagram in Fig.14 it becomes apparent that this condition can only be satisfied in a collinear geometry. However, for thin gratings, the phase matching condition $\vec{k}_{signal} = 2\vec{k}_2 - \vec{k}_1$ is somewhat relaxed due to normal diffraction effects. For this experiment, one focuses the beams onto the sample with a very small angle of only a few degrees between the pump and probe beams which helps to satisfy the phase matching condition. The same relaxation of the phase matching condition allows one to observe higher order mixing signals such as those scattered into directions $3\vec{k}_2 - 2\vec{k}_1$and $4\vec{k}_2 - 3\vec{k}_1$. These mixing signals have are also shown schematically in Fig. 14 and been observed experimentally in ZnCdSe multiple quantum wells.

Quantum beat spectroscopy and photon echo studies will also be described here since they directly pertain to experimental result presented in later chapters. Quantum beat spectroscopy considers the case where there exists three levels, two of which are closely spaced in energy. An ultrashort laser pulse, which is necessarily broad in photon energy, can coherently excite the closely spaced levels into a superposition state. Quantum beating occurs when there is population transfer back and forth between these two levels. A related phenomenon called a photon echo can occur for inhomogeneously broadened systems. One laser pulse, at time $t = 0$, creates a population of oscillators which begin to dephase after the pulse leaves the sample. Since the sample is inhomogeneously broadened, it is possible for the macroscopic polarization induced by the laser pulse to be zero before the individual atoms stop oscillating. A second laser pulse incident on the sample at a time $t = T$ can change the phase of the oscillation by 180 degrees. A coherent pulse of radiation will then be emitted at a time $t = 2T$ when the oscillators have rephased. For a homogeneously broadened resonance, a monotonic decay of the polarization is expected with no photon echo. TI-FWM cannot distinguish between a photon echo and a free polarization decay since the FWM signal is integrated in a slow detector. In order to know whether a sample exhibits a photon echo or a free polarization decay one must perform time-resolved FWM in order to measure the evolution of the FWM signal in time.

For ultrafast FWM experiments, it is important to know the temporal pulse width since this limits the time resolution of the experiment. For measurement of the fundamental pulse shape, a commercial autocorrelator (Inrad Model 514A) was used. Since it is very difficult to make the second harmonic required for autocorrelation in the wavelength range from 345 nm to 495 nm, an alternate method was used. Non-collinear sum-frequency generation was used to create the sum frequency of the fundamental and the second harmonic. The FWM set-up was used to scan the delay between the red and the blue pulses to get the cross-correlation. Thus, we had a measure of the pulse width of the second harmonic. The autocorrelation width was found to be $\approx$160 fs at 900 nm while for a cross-correlation of 450 nm with 900 nm the width increased to $\approx$190 fs. Fig.15 shows a typical autocorrelation trace together with a cross-correlation between the red and the blue pulses at 900 nm. The increase in pulse width is, to a certain degree, determined by the thickness of the doubling crystal. A thicker crystal can be used to achieve higher conversion efficiency, but the pulse width becomes larger due to the difference in dispersion between the fundamental and second harmonic as both pulses travel through the crystal. For this work, the 0.5 mm LBO crystal provided a conversion efficiency of about 15 percent with only minimal pulse broadening.

Sample Preparation

In addition to the careful cleaning required before focusing laser light onto a sample, many samples require additional preparation so that they can be studied in a transmission geometry. Two types of preparation were employed: sample polishing and substrate removal via selective wet etching. If the sample substrate is transparent to the excitation laser wavelength, then the substrate does not need to be removed. However, the surface must be specular so that the pump beams and scattered probe beam exit the sample with minimal interface scattering. The more Rayleigh scattered light due to surface imperfections, the harder it is to find the FWM signal. Therefore, the substrate side of most samples was polished with a standard mechanical polishing set up using diamond particles suspended in a light oil. The final polishing step used

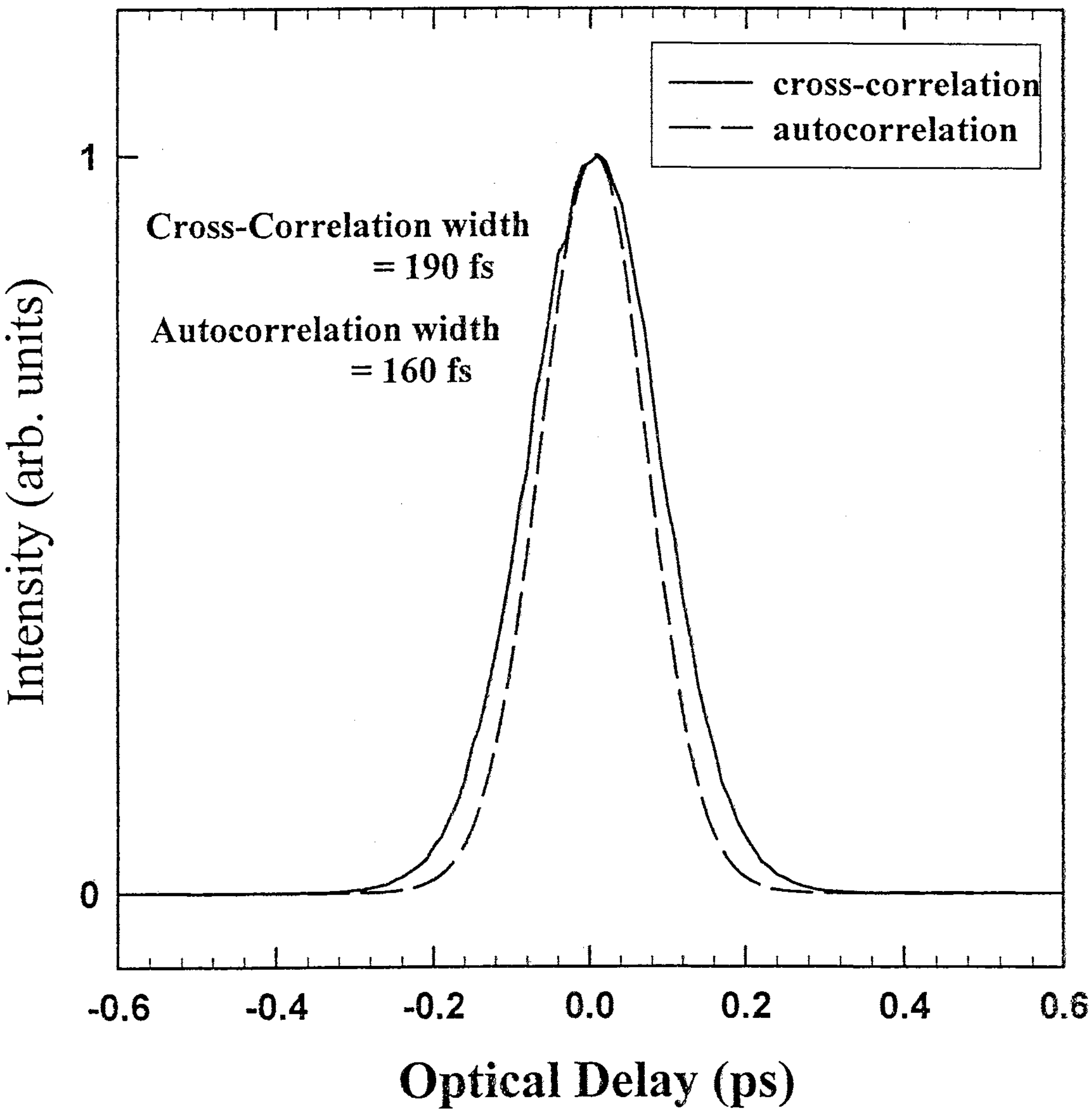

Figure 15. Autocorrelation and cross-correlation of laser pulses. The second harmonic is slightly broader than the fundamental due to dispersion in the doubling crystal. For an assumed inverse secant squared pulse shape the pulse widths would be ≈125 fs for the fundamental and ≈150 fs for the second harmonic.

0.25 micron diamond particles which provides a very smooth surface with very little scattered light.

Many of the first CT-FWM measurements were performed on high quality GaAs samples grown by molecular beam epitaxy and, in fact, results from a GaAs quantum well sample are presented below for comparison to wide gap materials. GaAs quantum well samples are grown on GaAs substrates which are opaque to the laser pump so that the substrate must be removed in order to perform transmission measurements. In order to be etched, a sample must have a relatively thick AlGaAs layer grown on the substrate prior to the growth of the quantum well. The AlGaAs layer etches much slower than the GaAs substrate and serves as an etch stop. A small piece of the sample with dimensions 5 mm x 5 mm is epoxied down to a one cm diameter piece of c-plane sapphire. Norland optical index matching glue was used in order to get the best possible index match from the sample to the sapphire. Actually, the index of the glue is only 1.5, but it is the highest glue available and hence provides a better match than other glues. The glue and the sapphire will provide structural support for the very thin epitaxial layer after the substrate has been removed. Photoresist is applied to the edges of the sample leaving only a very small hole less than 1 mm x 1 mm where the etch chemicals will remove the substrate. The sample is then placed in solution composed of 30 parts by volume of 30 % hydrogen peroxide and 1 part concentrated ammonium hydroxide. The etch time, of course, depends on the thickness of the substrate remaining after the bulk of the substrate is removed via mechanical polishing and can vary anywhere from 30 min to 3 hours. The AlGaAs etch-stop layer really only slows the etch and one must watch the sample constantly while it is in the etch solution. However, the sample can be removed and rinsed in de-ionized water and the etch continued after a short break. One can tell that the etch is complete when the sample becomes thin enough to be transparent. Unfortunately, an etched sample can be expected to behave slightly differently than an unetched sample at low temperature due to differences in the thermal expansion coefficients of the Norland glue, the sapphire, and the sample. An etched sample at low temperature may be under strain which

was not present in the unetched sample and the energy levels may shift slightly. An etched sample also has a finite lifetime due to temperature cycling and most etched samples crack beyond use after a hundred or more cycles to low temperature.

Theoretical Description of CT-FWM

A theoretical description of CT-FWM will be given based on the two-level, non-interacting model. This analysis results in the optical Bloch equations which are a general set of equations used to model resonance phenomena. The optical Bloch equations will then be solved for the specific case of CT-FWM in semiconductors using third-order perturbation theory. Many of the details of the FWM calculation will be presented in appendix A. Several more advanced theories considering interaction between resonances will briefly be described since they are required to explain various FWM experimental results.

Non-Interacting Two-Level Model

Many physical systems as a first approximation can be modeled as systems consisting of only two energy levels; it is assumed that all other energy levels in the system play a negligible role. It also proves very useful to assume that the individual species, whether they are atoms or semiconductor excitations, do not interact with each other. These approximations are useful in modelling many physical systems such as dilute atomic gases, where there is only a small probability of an atom interacting with another atom in the system. Here we will be applying these assumptions to excitons in a semiconductor where such approximations do not hold quite as well. However, if we consider a dilute gas of excitons for which the average distance between excitons is much larger than the exciton Bohr radius, then in a first approximation we can consider that the excitons do not interact with each other. As discussed below, several studies have included interaction effects in the interpretation of coherent spectroscopic data [46]. In the analysis of two-level systems, the radiation field is usually treated classically. Although a fully quantized analysis can be done using

the 'dressed atom' approach [48,49], for simplicity, only a semi-classical analysis of two-level atoms will be presented here.

Consider a collection of two-level oscillators which for times $t \langle 0$ are initially in the ground state (level a). At time $t = 0$ an extremely short laser pulse is incident upon the collection of oscillators. In the presence of the laser pulse, the oscillators are driven at the frequency of the incident field. After the laser pulse has passed through the sample, the oscillators will begin to drift out of phase with each other. This change from oscillation in phase to independent oscillation is known as dephasing. The oscillators slowly lose the phase coherence originally created by the laser pulse in a characteristic time T_2, the transverse relaxation time. The lifetime of the oscillators in the excited state is given by the longitudinal relaxation time T_1. Strictly speaking, since an atom is necessarily dephased when it drops back to the lower energy level, the dephasing time T_2 is given by

$$\frac{1}{T_2} = \frac{1}{2T_1} + \frac{1}{T'} \tag{13}$$

where T' represents pure dephasing processes. In order to observe coherent effects the system must be excited in a time which is short compared to T_2. The availability of ultrafast laser systems has allowed researchers to study coherent effects in semiconductors as well as atomic and molecular systems. Typically, semiconductors have dephasing times which are in the picosecond or sub-picosecond range whereas atomic systems take much longer to dephase. Since T_1 for semiconductors is typically in the nanosecond range and T' is in the picosecond range, the effect of the lifetime on dephasing can be neglected. That is, the number of oscillators losing their phase coherence due to relaxation to the lower level is negligible compared to those dephasing through other mechanisms.

The Optical Bloch Equations

A general theoretical treatment of the optical Bloch equations will be presented. These equations are used to model the evolution of such a system of two-level atoms under resonant excitation. Although, there are many interesting effects observed

in coherent spectroscopy, this paper will specifically be concerned with interpreting data from CT-DFWM experiments. The third-order polarization studied in a CT-DFWM experiment was first theoretically calculated by Yajima and Taira [50]. A derivation of the this third-order polarization will be presented with many of details presented in Appendix A.

In this section we show how a system of dipole oscillators under resonant excitation can be modeled in the coherent transient regime. The optical Bloch equations govern the dynamics of such a system of oscillators. The optical Bloch equations are derived in many texts [51–53] and the development and notation here closely follows that of Butcher and Cotter [52]. Since the density matrix formalism will be used extensively a short review will be provided.

Density Matrix Formalism. The expectation value for an arbitrary operator $\hat{A}$ can be expressed as

$$\left\langle \hat{A} \right\rangle = \sum_n p_n Tr \left[P\left(\psi_n\right) \hat{A} \right] \tag{14}$$

where p_n is the probability of the system being in state ψ_n and $P\left(\psi_n\right)$ is the projection operator [52]:

$$P\left(\psi_n\right) \Psi = \left[\langle \psi_n \mid \Psi \rangle\right] |\psi_n\rangle \,. \tag{15}$$

The expectation value of the operator $\hat{A}$ can then be written as [54]

$$\left\langle \hat{A} \right\rangle = Tr \left[\rho \hat{A} \right], \tag{16}$$

where the density matrix ρ is defined as [54]

$$\rho \equiv \sum_n p_n P\left(\psi_n\right). \tag{17}$$

The equation of motion for the density operator as determined by the Schrödinger equation is given by

$$i\hbar \frac{d\hat{\rho}}{dt} = \left[\hat{H}, \hat{\rho} \right] \tag{18}$$

In deriving the optical Bloch equations, we will use a Hamiltonian of the following form [52]

$$\hat{H} = \hat{H}_o + \hat{H}_I(t) + \hat{H}_R(t) \tag{19}$$

where $\hat{H}_o$ is the Hamiltonian of the unperturbed system and is assumed to be time independent. $\hat{H}_I(t)$ is the interaction Hamiltonian and $\hat{H}_R(t)$ is a time-dependent relaxation Hamiltonian. The equation of motion can then be written as

$$i\hbar\frac{d\hat{\rho}}{dt} = \left[\hat{H}_o, \hat{\rho}\right] + \left[\hat{H}_I(t), \hat{\rho}\right] + \left[\hat{H}_R(t), \hat{\rho}\right]. \tag{20}$$

The density matrix can be written as a power series in $\hat{H}_I(t)$ [52]

$$\hat{\rho}(t) = \hat{\rho}^{(0)} + \hat{\rho}^{(1)}(t) + \hat{\rho}^{(2)}(t) + ... + \hat{\rho}^{(n)}(t) + ..., \tag{21}$$

where $\hat{\rho}^{(0)}$ is the density matrix in the absence of perturbation, $\hat{\rho}^{(1)}(t)$ is linear in $\hat{H}_I(t)$, and so forth. We also impose the constraint that $\hat{\rho}^{(i)}(t = -\infty) = 0$ for any value of the index i [52]. By plugging Eqn.(21) into Eqn.(20) and equating like powers of $\hat{H}_I(t)$, we can write down an equation of motion for the nth component of the density matrix

$$i\hbar\frac{d\hat{\rho}^{(n)}(t)}{dt} = \left[\hat{H}_o, \hat{\rho}^{(n)}(t)\right] + \left[\hat{H}_I(t), \hat{\rho}^{(n-1)}(t)\right] + \left[\hat{H}_R(t), \hat{\rho}^{(n)}(t)\right]. \tag{22}$$

This equation will be used in section three when we derive the third-order polarization produced in a CT-DFWM experiment.

Derivation of the Optical Bloch Equations. Consider a system consisting of only two levels with energies E_a and E_b $(E_b \rangle E_a)$ and eigenfunctions u_a and u_b, respectively. In the absence of a perturbation and with the system initially in state u_a, the wave function will evolve in time according to

$$\psi = \exp\left(-\frac{iE_at}{\hbar}\right)u_a. \tag{23}$$

More generally, the system can be in some superposition of levels a and b and the wave function is then given as a superposition of the two states

$$\psi = a\exp\left(-\frac{iE_at}{\hbar}\right)u_a + b\exp\left(-\frac{iE_bt}{\hbar}\right)u_b. \tag{24}$$

Now we consider an ensemble of such two-level systems. The equation of motion for such an ensemble is given by Eqn.(18) and the density operator for an ensemble of

two-level systems is given by

$$\hat{\rho} = \begin{bmatrix} \rho_{aa} & \rho_{ab} \\ \rho_{ba} & \rho_{bb} \end{bmatrix} = \sum_n p_n \begin{bmatrix} |a|^2 & ab^* \exp\left(i\Omega_{ab}t\right) \\ a^*b \exp\left(-i\Omega_{ba}t\right) & |b|^2 \end{bmatrix}, \tag{25}$$

where $\hbar\Omega_{ba} = E_b - E_a$. The frequency of the incident radiation is ω. The unperturbed Hamiltonian is [52]

$$\hat{H}_o = \begin{bmatrix} E_a & 0 \\ 0 & E_b \end{bmatrix}, \tag{26}$$

and the Hamiltonian for a dipole interaction is given by

$$\hat{H}_I = \begin{bmatrix} \delta E_a & -e\vec{r}_{ab} \cdot \vec{E}(t) \\ -e\vec{r}_{ba} \cdot \vec{E}(t) & \delta E_b \end{bmatrix}. \tag{27}$$

The diagonal terms in the interaction Hamiltonian represent the optical Stark shift due to the applied field. Although this Stark splitting can be significant, for simplicity it will be neglected in this treatment. The off-diagonal elements correspond to allowed dipole transitions. Substituting Eqn.(23) and Eqn.(24) into Eqn.(20) we arrive at the following equations of motion

$$i\hbar\frac{d\rho_{aa}}{dt} = -e\left(\rho_{ba}\,\vec{r}_{ab} - \rho_{ab}\,\vec{r}_{ba}\right) \cdot \vec{E}(t) + \left[\hat{H}_R, \hat{\rho}\right]_{aa}, \tag{28}$$

$$i\hbar\frac{d\rho_{bb}}{dt} = e\left(\rho_{ba}\,\vec{r}_{ab} - \rho_{ab}\,\vec{r}_{ba}\right) \cdot \vec{E}(t) + \left[\hat{H}_R, \hat{\rho}\right]_{bb}, \tag{29}$$

$$i\hbar\frac{d\rho_{ab}}{dt} = i\hbar\frac{d\rho*_{ba}}{dt} = -\rho_{ab}\left(\hbar\Omega_{ba}\right) - \left(\rho_{bb} - \rho_{aa}\right) e\,\vec{r}_{ba} \cdot \vec{E}(t) + \left[\hat{H}_R, \hat{\rho}\right]_{ab}. \tag{30}$$

We will also assume that the electric field $\vec{E}(t)$ is a single quasi-monochromatic wave of frequency ω given by

$$\vec{E}(t) = \frac{1}{2}\vec{E}_\omega(t)\exp(-i\omega t) + c.c. \tag{31}$$

We now let $\vec{E}_\omega(t) = \hat{e}E(t)$ and define the "Rabi Frequency" $\beta(t) = e\,\vec{r}_{ba} \cdot \hat{e}E(t)$. The equations then become

$$\dot{\rho}_{aa} = i\left(\rho_{ba} - \rho_{ab}\right)\beta(t)\cos\left(\omega t\right) - \frac{i}{\hbar}\left[\hat{H}_R, \hat{\rho}\right]_{aa}, \tag{32}$$

$$\dot{\rho}_{bb} = -i\left(\rho_{ba} - \rho_{ab}\right)\beta(t)\cos\left(\omega t\right) - \frac{i}{\hbar}\left[\hat{H}_R, \hat{\rho}\right]_{bb}, \tag{33}$$

$$\dot{\rho}_{ab} = -i\,\rho_{ab}\Omega_{ba} + i\left(\rho_{bb} - \rho_{aa}\right)\beta(t)\cos\left(\omega t\right) - \frac{i}{\hbar}\left[\hat{H}_R, \hat{\rho}\right]_{ab}. \tag{34}$$

Next we will invoke the rotating wave approximation. This approximation consists of neglecting terms which oscillate at a frequency of $\omega + \Omega_{ba}$. In order to understand where these oscillations come from we will examine one equation in detail. Substituting Eqn.(25) into Eqn.(32) we get the following equation:

$$\begin{aligned}\dot{\rho}_{aa} = \tfrac{1}{2}i\ \{\ & a^*b\left[\exp\left(-i\Delta t\right) + \exp\left(-i\left\{\omega + \Omega_{ba}\right\}\right)\right] \\ & -ab^*\left[\exp\left(-i\Delta t\right) + \exp\left(-i\left\{\omega + \Omega_{ba}\right\}\right)\right]\ \}\ \beta(t) - \tfrac{i}{\hbar}\left[\hat{H}_R, \hat{\rho}\right]_{aa},\end{aligned} \tag{35}$$

where $\Delta = \omega - \Omega_{ba}$. For near resonant excitation, we can safely neglect terms oscillating at frequency $\omega + \Omega_{ba}$. The relaxation Hamiltonian will be treated phenomenologically. Rather than trying to model relaxation processes, we will simply assign a transverse lifetime T_2, and a longitudinal lifetime T_1. We make the following substitutions:

$$\left[\hat{H}_R, \hat{\rho}\right]_{bb} = -i\hbar\frac{\rho_{bb}}{T_1}, \tag{36}$$

$$\left[\hat{H}_R, \hat{\rho}\right]_{aa} = i\hbar\frac{\rho_{aa}}{T_1} = i\hbar\frac{\left(1 - \rho_{bb}\right)}{T_1}, \tag{37}$$

$$\left[\hat{H}_R, \hat{\rho}\right]_{ab} = -i\hbar\frac{\rho_{ab}}{T_2}, \tag{38}$$

$$\left[\hat{H}_R, \hat{\rho}\right]_{ba} = -i\hbar\frac{\rho_{ba}}{T_2}. \tag{39}$$

Applying the rotating wave approximation, substituting in these phenomenological relaxation terms, and using the substitution $\rho_{ab} = \rho_{ab}^{\Omega}\exp\left[i\left(\Omega_{ba} - \Delta\right)t\right]$, the equations of motion become

$$\dot{\rho}_{aa} = \frac{i}{2}\left(\rho_{ba}^{\Omega} - \rho_{ab}^{\Omega}\right)\beta(t) + \frac{\left(1 - \rho_{bb}\right)}{T_1}, \tag{40}$$

$$\dot{\rho}_{bb} = -\frac{i}{2}\left(\rho_{ba}^{\Omega} - \rho_{ab}^{\Omega}\right)\beta(t) + \frac{\rho_{bb}}{T_1}, \tag{41}$$

$$\dot{\rho}_{ab}^{\Omega} = i\,\rho_{ab}^{\Omega}\Delta + \frac{i}{2}\left(\rho_{bb} - \rho_{aa}\right)\beta(t) + \frac{\rho_{ba}}{T_2}\exp\left[i\left(\Omega_{ba} - \Delta\right)t\right]. \tag{42}$$

One final substitution of

$$u = \rho_{ba}^{\Omega} + \rho_{ab}^{\Omega}, \tag{43}$$

$$v = i\left(\rho_{ba}^{\Omega} - \rho_{ab}^{\Omega}\right), \tag{44}$$

$$w = \rho_{bb} - \rho_{aa}, \tag{45}$$

yields

$$\dot{u} = -\Delta v - \frac{u}{T_2}, \tag{46}$$

$$\dot{v} = -\Delta u + \beta(t)w - \frac{v}{T_2}, \tag{47}$$

$$\dot{w} = -\beta(t)v - \frac{w - w_0}{T_1}, \tag{48}$$

where $w_0 \equiv \rho^0_{bb} - \rho^0_{aa}$ is equilibrium population difference. These are the optical Bloch equations which are used to describe the dynamics of an ensemble of resonantly excited two-level atoms.

Interpretation of the Optical Bloch Equations. We will now consider the physical implications of the equations derived in the previous section. The macroscopic polarization for an ensemble of two-level atoms in the presence of an external field given by Eqn.(31) can be written as

$$\vec{P}(t) = N\langle e\vec{r}\rangle = N\,Tr(\hat{\rho}e\vec{r}), \tag{49}$$

where N is the number of atoms or oscillators. Using the equations above it can be shown that the amplitude of the polarization is given by [55]

$$P(t) = N\,e\vec{r}\cdot\hat{e}\,(u - iv)\,. \tag{50}$$

So we see that u is the in-phase portion of the polarization while v is the in-quadrature part. From Eqn.(45), we can see that w represents the population difference between the upper and lower levels. Thus w is sometimes called the population inversion.

The components of the optical Bloch equations can be changed into a vector format as follows. The vectors

$$\begin{aligned} \vec{R} &\equiv u\hat{x} + v\hat{y} + w\hat{z} \\ \vec{\Omega} &\equiv -\beta(t)\hat{x} + 0\hat{y} + \hat{z} \end{aligned} \tag{51}$$

are defined and from Eqn.(46) the equation of motion for the vector $\vec{R}$ can be written as [51]

$$\frac{d\vec{R}}{dt} = \vec{\Omega}\ X\ \vec{R} + \text{relaxation terms.} \tag{52}$$

This vector $\vec{R}$ is called the Bloch vector. The evolution of the system in the presence of an external field results in rotations of the Bloch vector. In thermal equilibrium with no external field, $u = 0$ and $v = 0$ and we have only population in the lower energy level and thus the vector $\vec{R}$ is stationary and points in the $-\hat{z}$ direction. When an ultrashort laser pulse is incident on a collection of oscillators, we can describe the effect of the pulse in terms of a sudden change in the vector $\vec{R}$. Consider a system initially in equilibrium with $\vec{R} = w_0\hat{z}$. For population only in the lower level this will point in the $-\hat{z}$ direction. A resonant pulse will act to rotate the vector about the $\hat{x}$ axis [52]. For example, if we apply a pulse such that $\beta t = \frac{\pi}{2}$ (a '$\frac{\pi}{2}$ pulse') to a system initially in thermal equilibrium, then we will have $\vec{R} = v\hat{y}$ and the system will begin to evolve according to Eqn.(52). Note that βt is the pulse area defined by [51]

$$\Theta(r,t) = \beta t = \frac{\mu_{ba}}{\hbar}\int_{-\infty}^{+\infty} E(r,t')dt', \tag{53}$$

where $\mu_{ba} = \langle\psi_b| e\vec{r} |\psi_a\rangle$ is the dipole matrix element. Another important example is that of an incident pulse of area π. This case produces a complete population inversion with $\vec{R} = -w_0\hat{z}$. Many additional results, including solutions to the optical Bloch equations in various limiting cases [53], can be found in several excellent reviews [51–53]. Although the optical Bloch equations generally describe the interaction of a resonant electric field and a system of dipoles, many experimental procedures used to study coherent phenomena require specialized theoretical analysis. In the next section we shall consider how one theoretically models the polarization produced in a simple four-wave-mixing experiment.

Coherent-Transient Degenerate Four-Wave-Mixing

For the case of a semiconductor where $T_1 \gg T_2$, we can relate the homogeneous linewidth to T_2 by the relation $\Gamma = \hbar/T_2$. CT-FWM is one of the most reliable methods of determining T_2 and hence the homogeneous linewidth. In fact, the homogeneous linewidth can even be determined in the presence of strong inhomogeneous broadening. As mentioned above, CT-FWM can provide valuable information about the time required for excitations in semiconductors to lose their phase coherence.

The decay time of the FWM signal, τ_{FWM}, is related to, but not equal to, the pure dephasing time T_2. In order to know how τ_{FWM} is related to T_2, the FWM signal must be calculated. In this section we will describe how one calculates the FWM signal diffracted into the $2\vec{k}_2 - \vec{k}_1$ direction.

The calculation was first performed by Yajima and Taira [50] and is based on a perturbative solution to the optical Bloch equations. The results of the calculation are presented here with the details of the calculation presented in Appendix A. In the experiment shown in Fig. 1, we are interested in an averaged polarization. Therefore, the third-order polarization diffracted into the direction $2\vec{k}_2 - \vec{k}$ is integrated to get the energy of the emitted light according to the following formula:

$$J = \int_{-\infty}^{+\infty} \left| \hat{P}_3^{(3)} (\vec{r}, t) \right|^2 dt. \tag{54}$$

After performing this integration we arrive at the final expressions for the energy of the third-order polarization. As discussed in appendix A, inhomogeneous broadening was included in the calculation using a Gaussian distribution function where $\delta\omega$ represents the amount of inhomogeneous broadening. For the case of strong inhomogeneous broadening $\left(\delta\omega \gg \frac{1}{T_2}\right)$:

$$J_I = \left\{ \begin{array}{ll} A \exp\left[-\frac{4}{T_2}(t_2 - t_1)\right] \left\{1 + \Phi\left[\frac{\delta\omega}{\sqrt{\pi}}(t_2 - t_1)\right]\right\} & t_2 - t_1 \rangle\ 0 \\ 0 & t_2 - t_1 \langle\ 0 \end{array} \right\} \tag{55}$$

where $\Phi(x) \equiv \frac{2}{\sqrt{\pi}} \int_0^x \exp(-t^2)\, dt$ and A is some constant. For the case of homogeneous broadening

$$J_H = \left\{ \begin{array}{ll} B \exp\left[-\frac{2}{T_2}(t_2 - t_1)\right] & t_2 - t_1 \rangle\ 0 \\ 0 & t_2 - t_1 \langle\ 0 \end{array} \right\}, \tag{56}$$

where B is some constant. These two equations can now be used to interpret the decay times found in CT-DFWM experiments. We see that we can relate the four-wave-mixing decay time to the transverse relaxation time by the following relations

$$T_2 = 4 \cdot \tau_{FWM} \qquad \text{inhomogeneously broadening,} \tag{57}$$

$$T_2 = 2 \cdot \tau_{FWM} \qquad \text{homogeneous broadening.} \tag{58}$$

Thus the homogeneous linewidth can be determined even in the presence of inhomogeneous broadening. These relations will be used to interpret experimental data presented in the next two chapters.

More Advanced Models Considering Interaction

The two-level, non-interacting model presented above works well to describe many of the features observed in CT-FWM measurements. However, there are interesting exceptions, such as negative time delay signal, where we must look to more complicated theories in order to explain the observed experimental results. The above analysis is based on the assumption that the two important levels involved do not interact with each other. This means that the excitations must be sufficiently dilute that there is no appreciable interaction between different oscillators. This assumption hold quite well for dilute atomic gases, but carriers in semiconductors interact strongly with their environment. This means that even at the lowest carrier densities some interaction can be expected. Thus, we must consider the effects of many body interactions in the FWM signal. The main way to do this is through the use of the semiconductor Bloch equations [34]. These equations allow for interactions between carriers via the Coulomb interaction. Within the Hartree-Fock approximation, these equations allow for Coulomb interactions between carriers and consider band filling effects, exchange interaction, and screening of the Coulomb potential. A great deal of theoretical work has been done to apply these equations to coherent processes in semiconductor [56–58] and several works calculate the expected FWM signal including many body interactions [59–63]. The calculation of the FWM signal via these equations is normally performed numerically and is beyond the scope of this experimental thesis. However, many body effects have been shown to influence the FWM signal. There is still much controversy regarding which effects are dominant. Two important concepts will be mentioned here which directly apply to interpretation of experimental data. Researchers have used calculations based on the semiconductor

Bloch equations to describe experimental data relating the density dependence of FWM and to negative time delay signal.

It was known even for the earliest CT-FWM experiments performed on GaAs semiconductors that excitons dephase more rapidly at higher carrier densities [64,65]. This is easy to understand based on the fact that when an exciton scatters with another exciton it loses its phase coherence with the original excitation and is dephased. As the density of excitons increases, the probability that excitons will scatter with each other increases and the dephasing time becomes faster. In one study, however, it was shown that the main contribution to the dephasing in semiconductors is due to excitation induced dephasing [63]. Their data indicate that dephasing rate is dependent on excitation density even for very low exciton densities. A non-interacting model cannot explain the observed data. The data were consistent with a calculation based on the semiconductor Bloch equations where dephasing due to excitonic screening is considered. In another study, researchers observed that the lineshape of the FWM signal changes at high exciton densities and they were able to qualitatively model their data via a numerical solution of the semiconductor Bloch equations to all orders [61].

Another experimental phenomenon which cannot be explained by a non-interacting two-level model is referred to as negative time delay signal [61,62]. Positive time delays are when the pump beam arrives before the probe. If the pump arrives before the probe, then there is a pump-induced polarization with which the probe interacts and scatters into the direction $2\vec{k}_2 - \vec{k}_1$. For negative time delays when the probe arrives before the pump, the pump-induced polarization has not yet been created so that the probe pulse cannot scatter into the direction $2\vec{k}_2 - \vec{k}_1$. However, negative time delay signals have been observed for homogeneously broadened GaAs-based samples even at very low densities. This cannot be understood in terms of the non-interacting, two-level model. Again, this data was theoretically described by numerically solving the semiconductor Bloch equations. The negative time delay signal can equivalently be described as due to a coherent exciton-exciton interaction. It was shown by Stafford *et al.* [66], that excitons can interact not only with the

electric field of the laser, but also with the polarization of every other exciton. Thus, we can have the diffraction of polarizations as well as the diffraction of electric fields. For negative time delays, the probe arrives first and creates a polarization response in the material. When the pump arrives, it causes that polarization created by the probe to be scattered into the direction $2\vec{k}_2 - \vec{k}$. Thus, the coherent exciton-exciton interaction allows for the diffraction of polarization and causes the negative time delay signal. Negative time delay signal has been observed from a ZnSe epilayer grown on GaAs. The results will be presented in the next chapter.

CHAPTER V

FOUR-WAVE-MIXING MEASUREMENTS IN ZnSe-BASED MATERIALS

Introduction

In the early 90's, there was a great deal of interest in II-VI materials for their potential use in blue light emitting devices. Due to the short lifetime of devices, researchers have largely given up on ZnSe-based blue emitters and have embraced the III-nitrides as the blue/UV emitting material of choice. However, the interest in II-VI materials as blue light emitters has stimulated a great deal of fundamental studies of the properties of this wide gap material. Advances in the growth of II-VI materials has made available samples extremely high optical quality. This has allowed researchers to study fundamental optical processes in samples where the effects of impurities and dislocations were greatly reduced. In particular, the optical properties of excitons in II-VI compounds and their quantum wells have been studied in great detail [67–77].

It has been many years since strong nonlinearities in II-VI compounds were first recognized and studied, both theoretically and experimentally [78–80,67]. With the wide availability of tunable picosecond and femtosecond laser sources, transient nonlinear spectroscopy is being used more and more to study bulk semiconductors and quantum wells. Various transient nonlinear spectroscopic techniques have already been used to study II-VI compound semiconductors. For example, a large third-order nonlinearity was reported in ZnSe using picosecond polarization spectroscopy, whereas Faraday rotation was used to investigate dephasing and spin relaxation in ZnSe based magnetic quantum wells [69]. In CdTe, CdSe, and related quantum wells,

FWM has been used to investigate exciton-acoustic phonon, and exciton-exciton interactions, and well as hot exciton relaxation [70–76]. In this chapter, the results will be presented from FWM measurements performed on ZnSe and ZnCdSe multiple quantum wells.

Since an abundance of coherent-transient, degenerate four-wave mixing (CT-DFWM) has already been done in GaAs and related quantum wells, it is interesting to compare results from GaAs compounds to experiments on II-VI materials. In GaAs based materials, DFWM has been used to study interactions among excitons, Fermi edge singularities, free carriers, and phonons [47,81,82,40], while the source of the nonlinearity itself has also been widely investigated [83,62,61,84–88,66]. It is now well established that contributions from coherent exciton-exciton interaction (or local field correction) [83,62,61,84,85] and biexcitonic effects play major roles in nonlinearities of GaAs based quantum wells. Do these same results or similar results hold for II-VI materials? What is the relative importance of exciton-exciton, exciton-phonon, and exciton-free carrier interactions in II-VI materials? Finally, what role do biexcitons play in the nonlinearities of II-VI compounds? All of these questions can be readily answered with coherent spectroscopy.

After briefly describing the samples used in this work and their linear optical properties, the results of coherent-transient FWM measurements in ZnSe-based materials will be presented. Extremely high order nonlinear signals have been observed as high as the thirteenth-order from a ZnCdSe/ZnSe multiple quantum well (MQW) sample. A direct comparison is made between CT-DFWM in CdZnSe quantum wells to a similar experiment on a GaAs based MQW. This comparison of CT-DFWM signals in II-VI and III-V materials is valuable in determining differences in materials systems as well as from a nonlinear optics point of view, since such a comparison gives information regarding the relative strength of the nonlinearities in each material. Negative time delay signal has been observed from an epilayer of ZnSe due to the 'so called' coherent exciton-exciton interaction. The homogeneous linewidth is studied as a function of temperature and exciton density in order to determine exciton-phonon and exciton-exciton coupling constants for this material system. A

study of exciton localization was also perform for several MQW samples of slightly lower optical quality where excitons are localized due to interface roughness.

The samples used in this work were grown by molecular beam epitaxy and were either epilayers of ZnSe grown on a GaAs substrate or MQW samples with a ZnCdSe well and ZnSe barriers grown on either GaAs or ZnSe substrates. The structure of a six period MQW sample with 12 % Cd concentration in the well is show in Fig. 16. The samples grown on GaAs substrates had to have the substrates removed via the selective wet etching process described in Chapter 4. Alternatively, FWM could be performed in the reflection geometry where the FWM is collected in the $-2k_2 + k_1$direction. Fig. 17 shows reflection geometry data together with transmission geometry data from the same sample. One can see that both geometries give the same FWM decay time. Note that the data has been scaled and that the signal intensity in reflection is comparable to that of the transmission geometry. For the work presented in this thesis, measurements were performed in a transmission geometry for ZnSe-based samples grown on GaAs substrates. Several of the samples were grown on a ZnSe substrate which reduced the effects of lattice mismatch and produced very high quality samples. For these samples, FWM could be performed in a transmission geometry without substrate removal. The substrate was thinned down and then polished as specular as possible to reduce the amount of unwanted Rayleigh scattered light.

Linear absorption and photoluminescence measurements taken from one MQW sample as shown in Fig. 18. The absorption data shows the heavy hole (HH) and light hole (LH) excitonic resonances from the ZnCdSe quantum wells. The low energy shoulder on the HH exciton peak is due to a one monolayer fluctuation in well thickness. The energy separation and intensity is consistent with one quantum well out of six being on monolayer thicker than the others. The PL data show only luminescence from the HH exciton states. The PL linewidth for the lowest energy peak is $\approx$ 6 meV full-width-at-half-maximum (FWHM) while the HH exciton from the absorption data is $\approx$ 9 meV. The CT-DFWM signal is more closely related to the absorption data since we are dealing with scattering out of initially excited

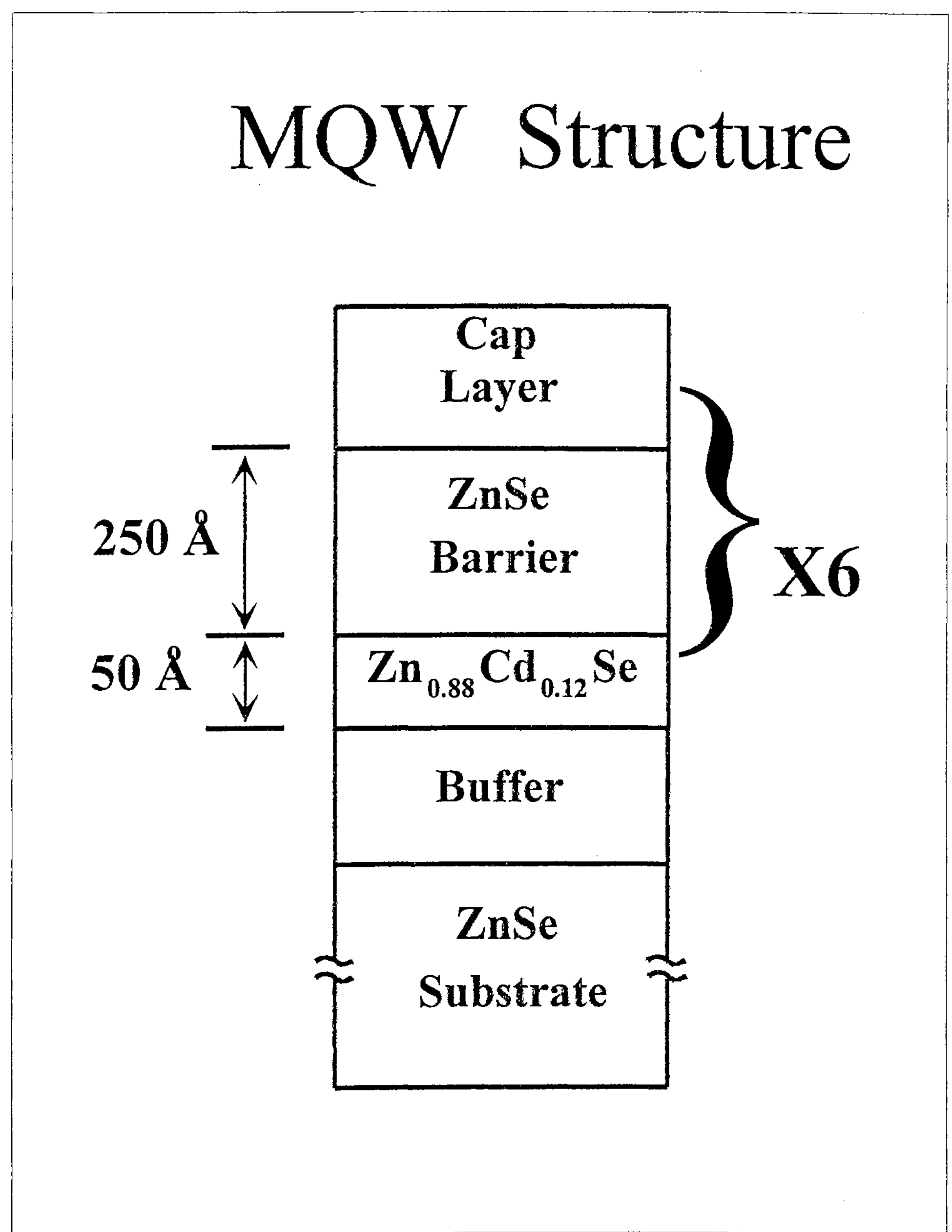

Figure 16. Sample structure of a ZnSe multiple quantum well (MQW). This sample was grown by molecular beam epitaxy on a ZnSe substrate. This type of sample was used for the majority of the FWM performed on ZnSe based materials.

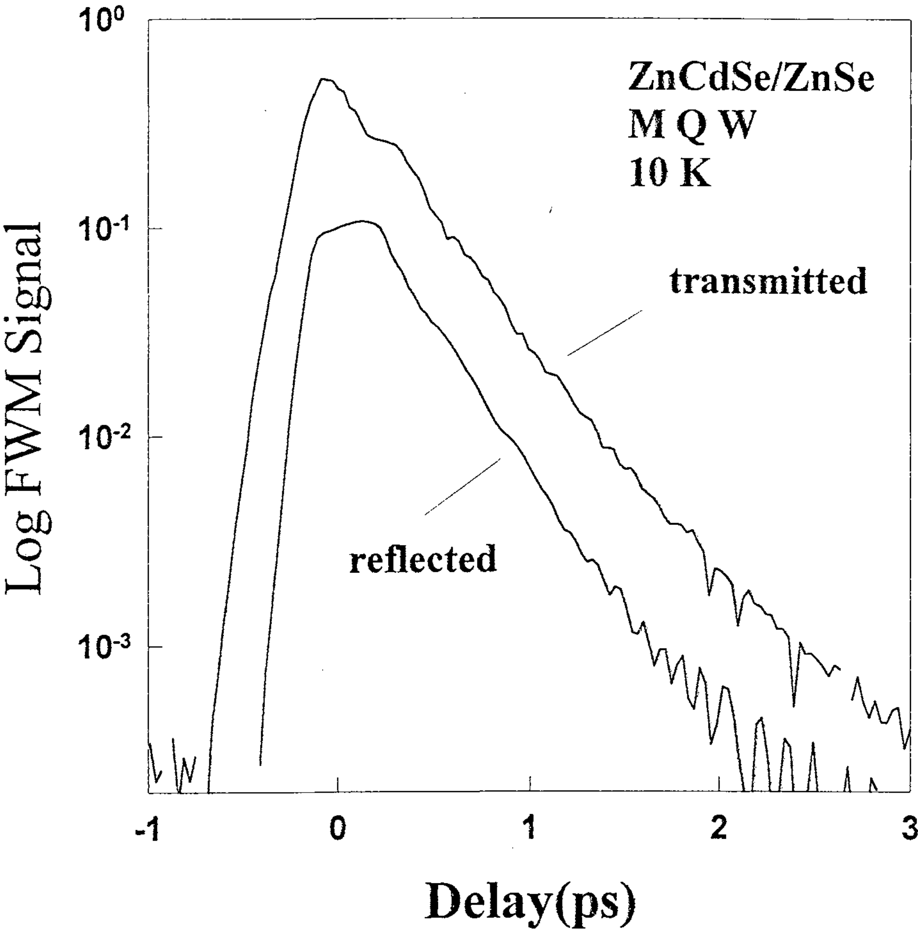

Figure 17. FWM signal for both the reflection and transmission geometries from the same sample. The decay constant is the same for either geometry. Note that the data has been scaled and that the signal intensity in reflection is comparable to that of the transmission geometry.

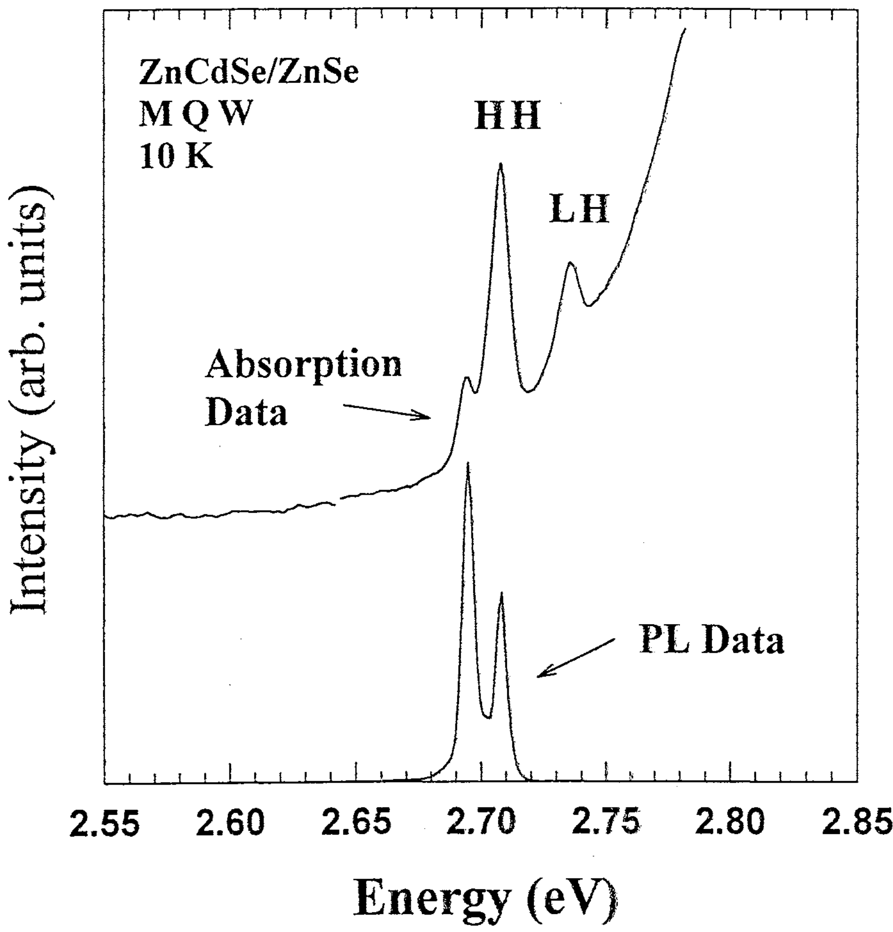

Figure 18. Absorption and Photoluminescence data for a ZnCdSe/ZnSe MQW sample. The absorption data show the heavy hole (HH) and light hole (LH) excitonic levels while the PL data show only HH excitons. The smaller peak on the lower energy shoulder of the HH exciton is due to a monolayer flucuation in the quantum well width for one of the six wells.

momentum states. Therefore, we expected FWM linewidths to follow the absorption linewidth. In general, the narrow linewidths from this linear data indicate that the sample is of high optical quality.

Extremely High Order Signals

Wave mixing signals have been observed from the third order up to the thirteenth order from a ZnCdSe/ZnSe MQW sample. Fig. 19 shows a photograph of the diffracted signals from the 6 period $Zn_{0.88}Cd_{0.12}Se$/ZnSe MQW sample grown at a delay of T=200 fs between the two incident beams. The two pump beams at $\mathbf{k}_1$ and $\mathbf{k}_2$ have been attenuated for the photograph using a neutral density filter. The picture was taken at 10 K with the exciting photon energy tuned near the HH excitonic resonance of the MQW (2.71 eV) with the average power of each beam at 10 mW and beam spot diameter of 100 μm at the sample. The third order intensity was as high as 25 μW and could easily be measured with a laser power meter. The 3rd, 5th, 7th, 9th, and 11th order signals in the phase matching directions of $2\mathbf{k}_2 - \mathbf{k}_1, 3\mathbf{k}_2 - 2\mathbf{k}_1, 4\mathbf{k}_2 - 3\mathbf{k}_1, 5\mathbf{k}_2 - 4\mathbf{k}_1$,and $6\mathbf{k}_2 - 5\mathbf{k}_1$ are clearly visible. The 13th order signal, while clearly visible to the naked eye, is barely visible in Fig. 19 in the direction of $7\mathbf{k}_2 - 6\mathbf{k}_1$. The observation of strong nonlinear diffracted signals up to the 13th order is in stark contrast with GaAs MQW's where diffracted signals only up to the 5th order has been observed [89]. Considering the fact that our MQW sample is optically thin, even higher order signals are very likely to be observed in thicker MQW samples. Higher order signals were also easily observed from all other ZnSe-based samples used in this study.

Fig. 20 shows the third, fifth, and seventh order wave mixing signal intensities plotted on a log-log plot as a function of total pump beam intensity for the ZnCdSe MQW sample. Also shown in the figure are third, fifth, and seventh order functions for comparison to the data. At low power, the signal diffracted into the $2\mathbf{k}_2 - \mathbf{k}_1$direction has a third order power dependence. As the power is increased and fifth order effects begin to appear, the third order signal begins to show a power law dependence of less than three since a significant fraction of the pump photons

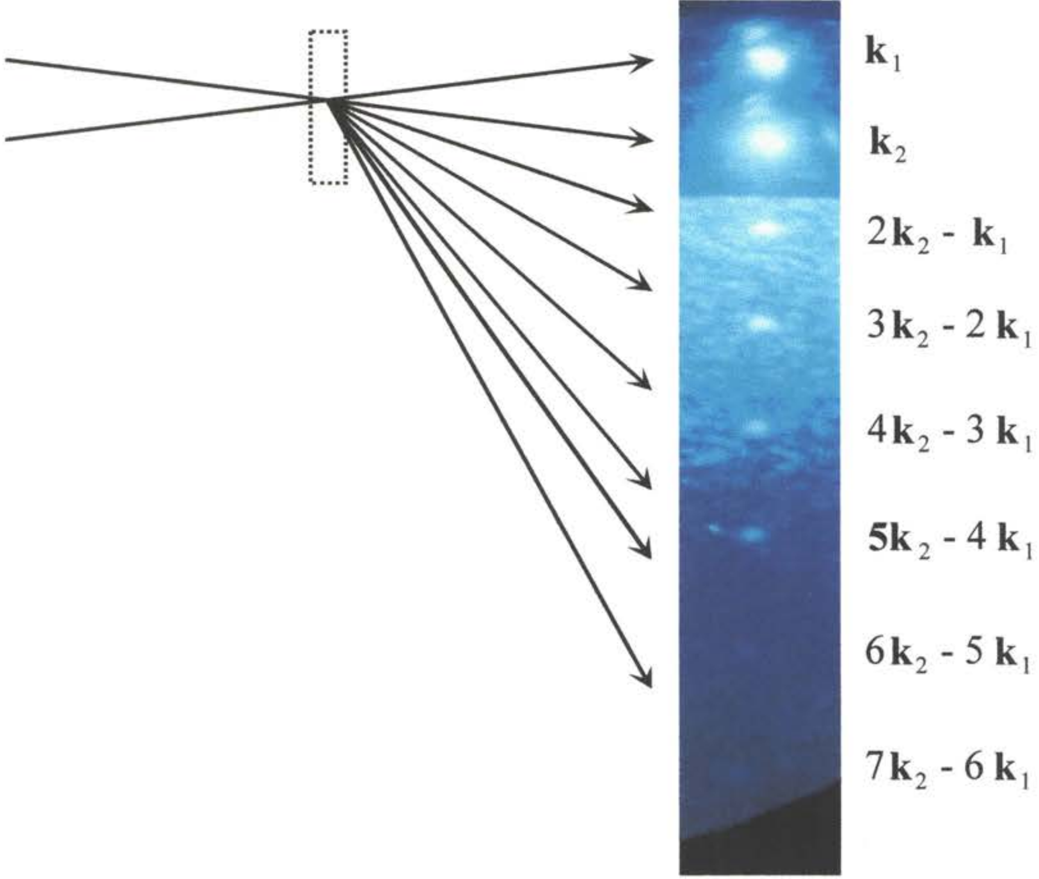

Figure 19. Photograph of higher order wave-mixing signals. The two pump beams at $\mathbf{k}_1$ and $\mathbf{k}_2$ are attenuated with a neutral density filter. Wave-mixing signals as high as the thirteenth order at $7\mathbf{k}_2 - 6\mathbf{k}_1$ have been observed.

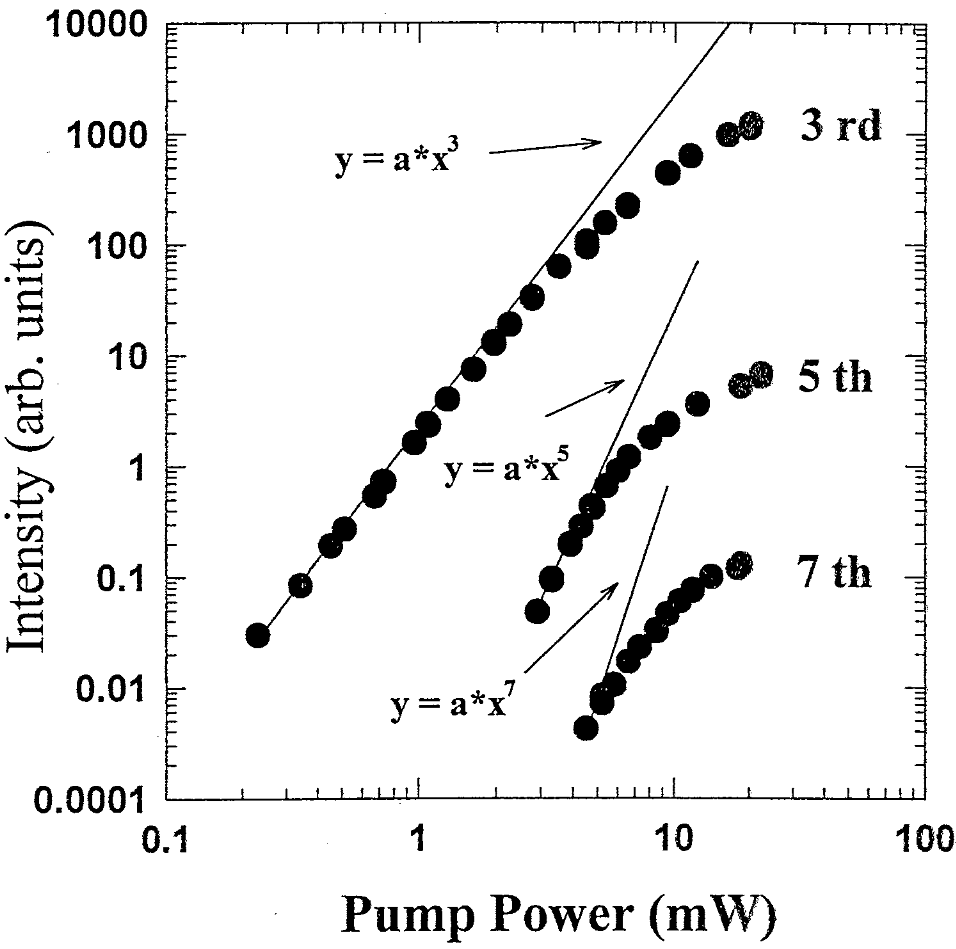

Figure 20. Third, fifth, and seventh order mixing signals shown as a function of pump power. Shown also for reference are third, fifth and seventh order dependencies on pump power. Note that in order to be in a third order regime, the pump power must be below a few mW.

are now being used to create the light scattered into the $3\mathbf{k}_2 - 2\mathbf{k}_1$ direction. For the majority of the work presented below, we are interested in the FWM signal so that we must work in a regime where fifth order effects can be neglected. It is also instructive to plot the power law dependence as a function of pump beam intensity for each order. This plot is shown in Fig. 21 for the third and the fifth order signals. This plot was made by using two points at a time to measure the slope on a log-log plot. One can see from this plot that the signals are only really third order and fifth order at very low intensities for these samples. Therefore, in practice one must always try to work in a density range as low as possible but where there is still good enough signal to noise ratio to obtain clean data.

The third, fifth, and seventh order wave mixing signals observed in the phase matched directions of $2\mathbf{k}_2 - \mathbf{k}_1$, $3\mathbf{k}_2 - 2\mathbf{k}_1$, and $4\mathbf{k}_2 - 3\mathbf{k}_1$ are plotted in Fig. 22 as functions of delay between the pump and probe, T. The laser is tuned to the HH excitonic resonance of the ZnCdSe quantum wells. It is clear from Fig. 22 that the fifth order (six-wave mixing) signal decays faster than the third order (FWM) signal, and that the seventh order signal, in turn, decays even faster as a function of T. Higher order signals decay faster because the diffraction of higher orders involves additional multiplications of polarizations, so that the decay rate increases. Spectrally-resolved FWM was also performed near zero delay by sending the higher order signals into a spectrometer as shown in Fig. 23. Also shown in the figure are the broad band excitation pulses used to create the exciton populations. It is interesting to note that the fifth and seventh order signals have the same spectral linewidth as the third order signal for both the ZnCdSe MQW and the ZnSe epilayer. An important distinction can be made at this time between time delay and real time. It is clear from Fig. 22 that higher order signals decay faster as a function of time delay. However, the spectrally resolved data shown in Fig. 23 show that the third, fifth, and seventh order wave mixing signals all have the same FWHM. This implies that the third and fifth order signals have a similar temporal evolution in real time although they decay much faster as a function of time delay. Mathematically speaking, this is because, when calculating the diffracted signal for the higher orders, additional multiplications of

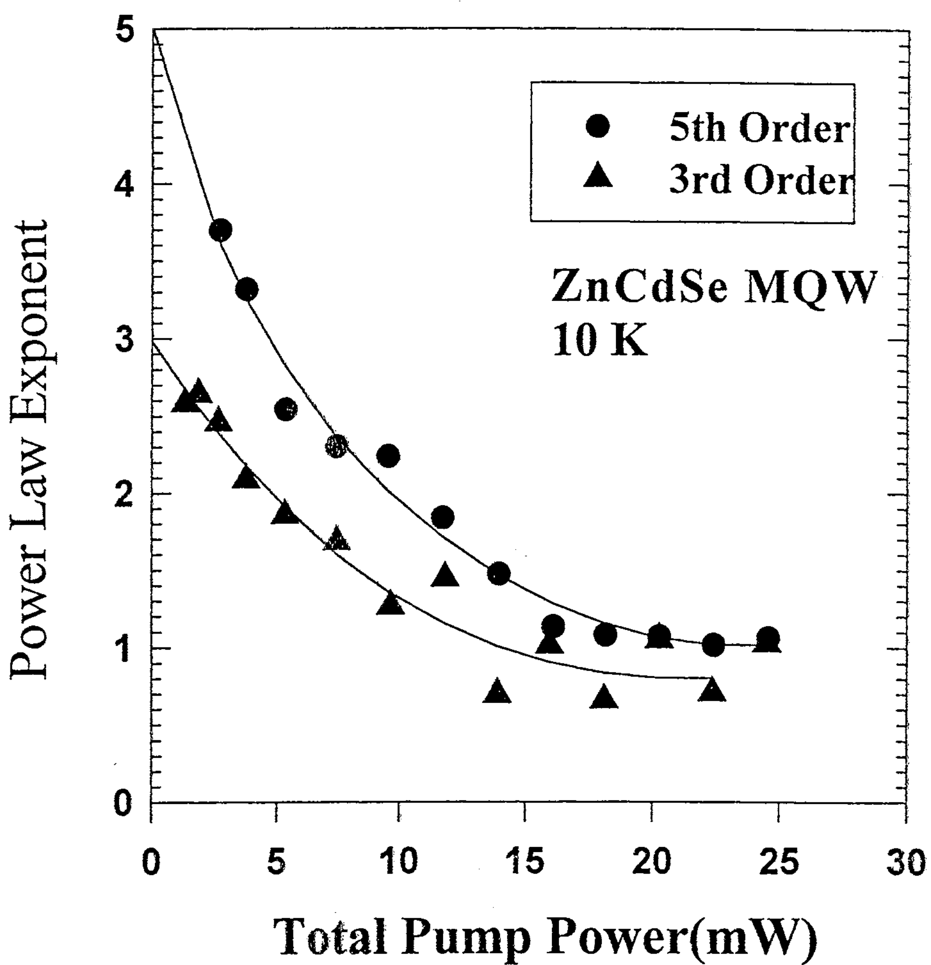

Figure 21. Power law dependence of the the third and fifth order signals. The data from Fig. 20 were fit to a power law dependence by finding the slope at each point on the curve. Note that the third order signal has a third order dependence only at very low power.

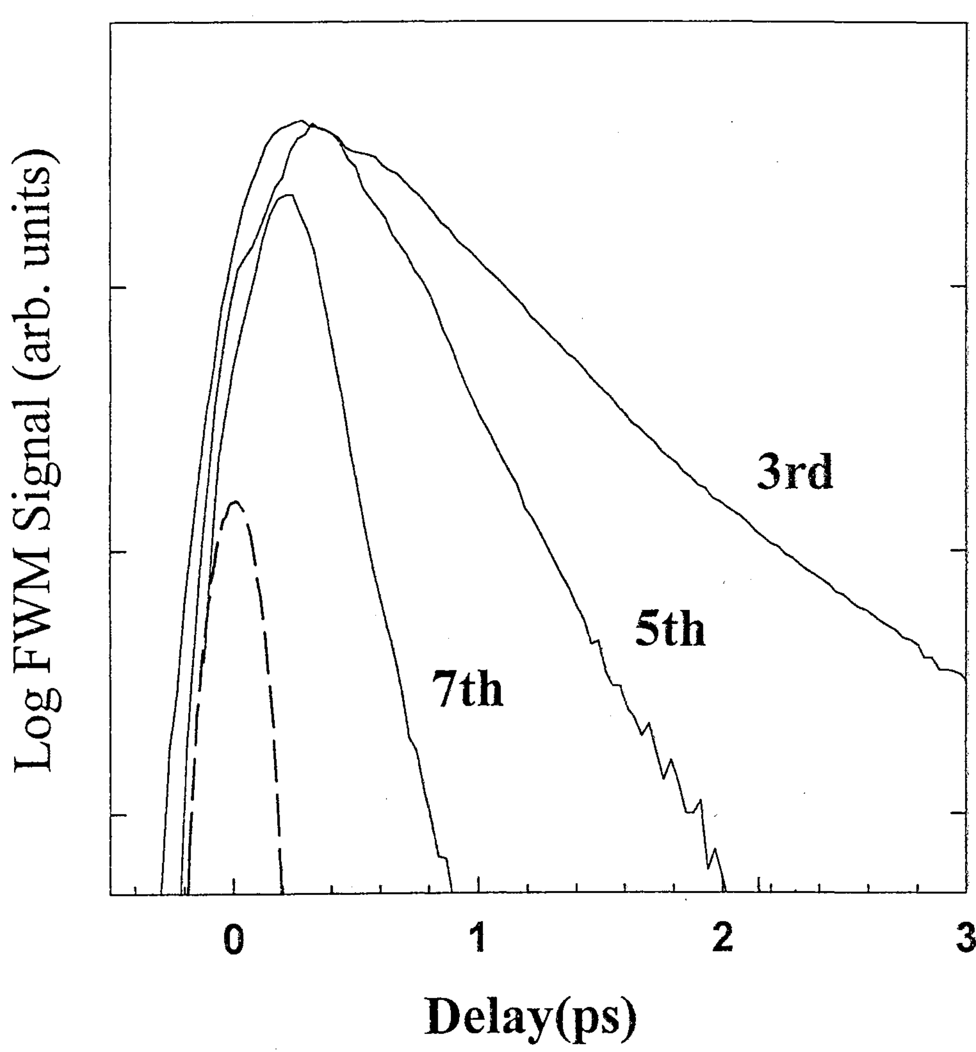

Figure 22. Higher order FWM signals plotted as a function of time delay. At a fixed power, the higher order signals decay faster then the lower order signals. The dashed line is the cross-correlation of the blue laser pulse with the red laser pulse.

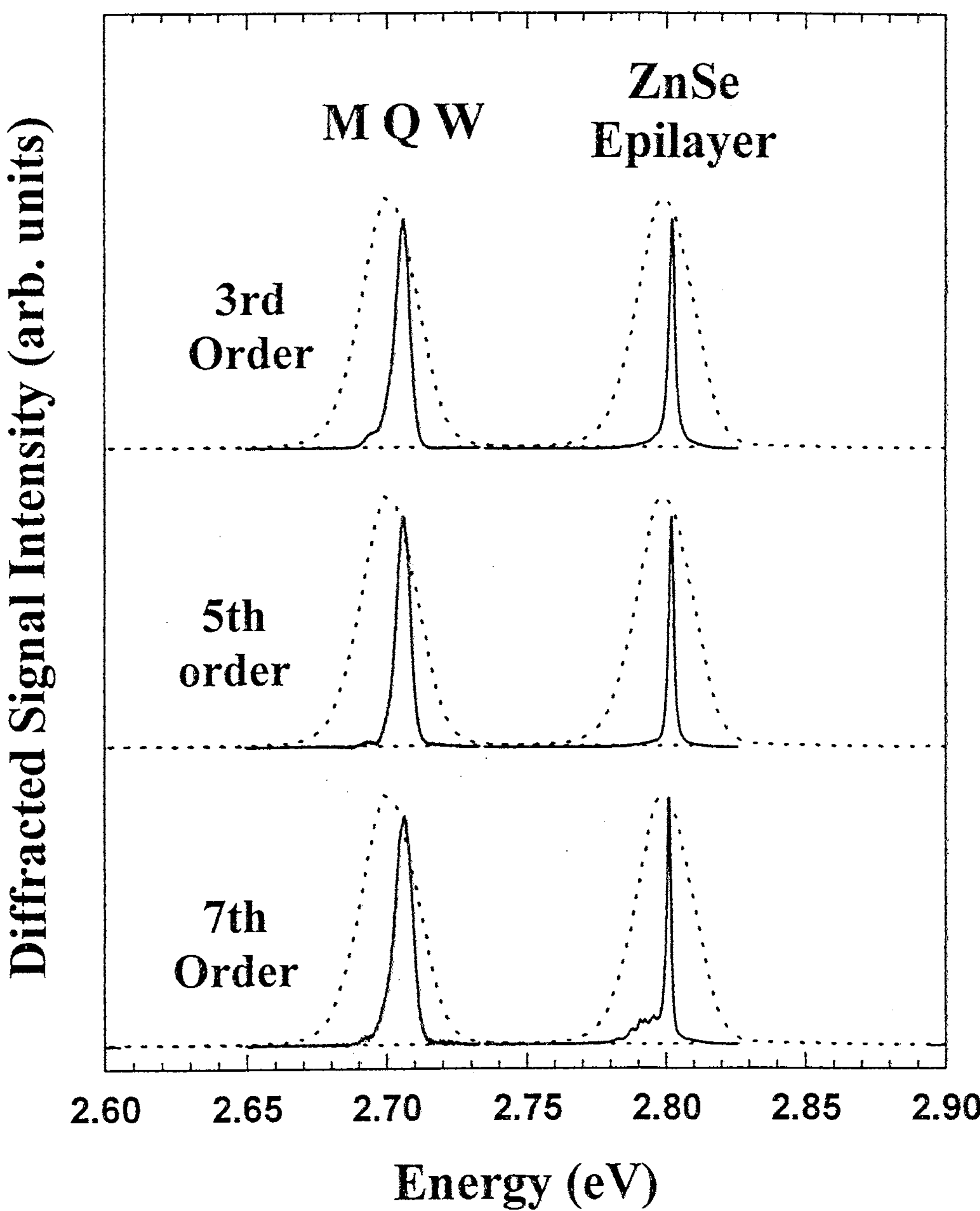

Figure 23. Spectrally-resolved FWM for the third, fifth and seventh order signals. Note that the linewidth is the same for all orders. Also shown here is the laser detuning for each of the spectra.

polarizations come into play causing the higher order signals to decrease quickly with increasing time delay. Although, the time evolution of the higher order signals has not been measured, we expect that the evolution in real time should be the same for each order. It is clear from this discussion that further study of temporal evolution of higher order signals would be very interesting.

From both experimental and theoretical points of view, it is interesting to compare relative intensity of wave mixing signals in ZnCdSe and GaAs quantum wells.We chose a GaAs MQW sample with a total well thickness 10 times larger (300 nm) than that of the ZnCdSe MQW (30 nm). The reason for choosing this particular GaAs MQW sample is two fold. First, 300 nm is a typical thickness for GaAs MQW's investigated by coherent spectroscopies, and second, the total number of photoexcited excitons (or the total number of photons absorbed), which is proportional to (FWHM of the excitonic peak, measured by linear absorption) x (peak absorption coefficient, measured by linear absorption) x (the total thickness) is roughly the same for the ZnCdSe MQW and the GaAs MQW when the incident laser powers are the same for both samples. This is consistent with the fact that there is roughly a factor of 10 difference in the penetration depths of GaAs and ZnSe at the band edge (1 μm for GaAs compared to 100 nm for ZnSe).

Fig. 24 shows the intensity of the diffracted light as a function of the order of nonlinearity for both the GaAs-based MQW sample and the ZnCdSe MQW sample. The data shown were taken at 10 K with the exciting photon energy tuned to the HH excitonic resonance of each sample (1.56 eV and 2.71 eV for the GaAs and the ZnCdSe MQW's, respectively) and with the average power of each beam at 10 mW. In the ZnCdSe MQW, the diffracted signal decreases very slowly as the order of nonlinearity increases; the signal decreases only by a factor of 5 as we go to the next higher order. In contrast, the nonlinear diffracted signals of the AlGaAs MQW are much weaker and decay faster as the order increases; the FWM signal is 16 times weaker than that of the ZnCdSe MQW, whereas the fifth order signal is 60 times weaker than the fifth order signal of the ZnCdSe MQW. The strong diffracted signals in this wide gap II-VI MQW are consistent with the elegant bond charge model of

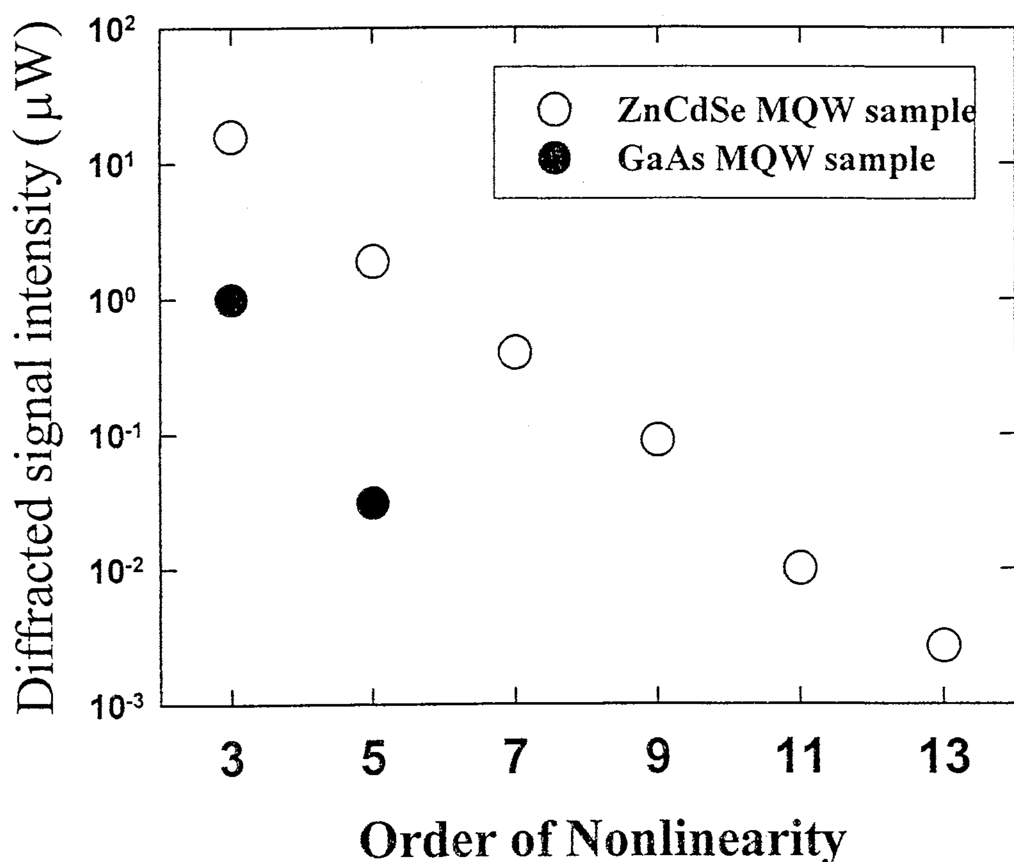

Figure 24. Comparison of signal intensities between ZnCdSe and GaAs MQW samples. The GaAs sample was chosen to have roughly the same net absorption as the ZnCdSe sample. Note that the intensity decreases much quicker with increasing order for the GaAs sample.

references [79,80,67] which predicts higher nonlinearities as the material becomes more polar. Furthermore, the stronger oscillator strength relative to GaAs quantum wells is also likely to play a role. Although more detailed studies are needed to compare the nonlinearities of GaAs and ZnSe based quantum wells, it is clear that nonlinear signals of ZnCdSe quantum wells are much stronger and easier to find, especially as the order of nonlinearity increases.

Third-Order Signal

For the remainder of this chapter we will be interested in only the third order or FWM signal. Thus, as mentioned above, we must try to work at the lowest densities possible in order to avoid higher order effects. In this section, the origin of the nonlinearity will be briefly discussed and data from an epilayer of ZnSe grown on GaAs which shows negative time delay signal will be presented. Finally, the homogeneous linewidth is studied as a function of temperature and exciton density to determine exciton-phonon and exciton-exciton scattering rates.

Origin of Nonlinearity

Since the large spectral bandwidth (20 meV full width at half maximum) of femtosecond pulses makes selective excitation difficult, the FWM signal may contain contributions from both excitons and free carriers. This is particularly true for GaAs samples where the exciton binding energy in only 4.2 meV. For the ZnCdSe MQW samples studied here, the exciton binding energy is 20 meV so that the number of free carrier created is much less than for the case of GaAs. However, due to band tailing states some free carriers are usually excited when the laser detuning is centered at the excitonic resonance. It has been shown for the GaAs material system, that free carriers are very efficient at dephasing excitons. Thus, it is important to know the origin of the FWM signal that we are detecting.

In Fig. 25, the FWM signal of the ZnCdSe MQW near zero delay is plotted against the center photon energy of the pulse. Linear absorption data is also included

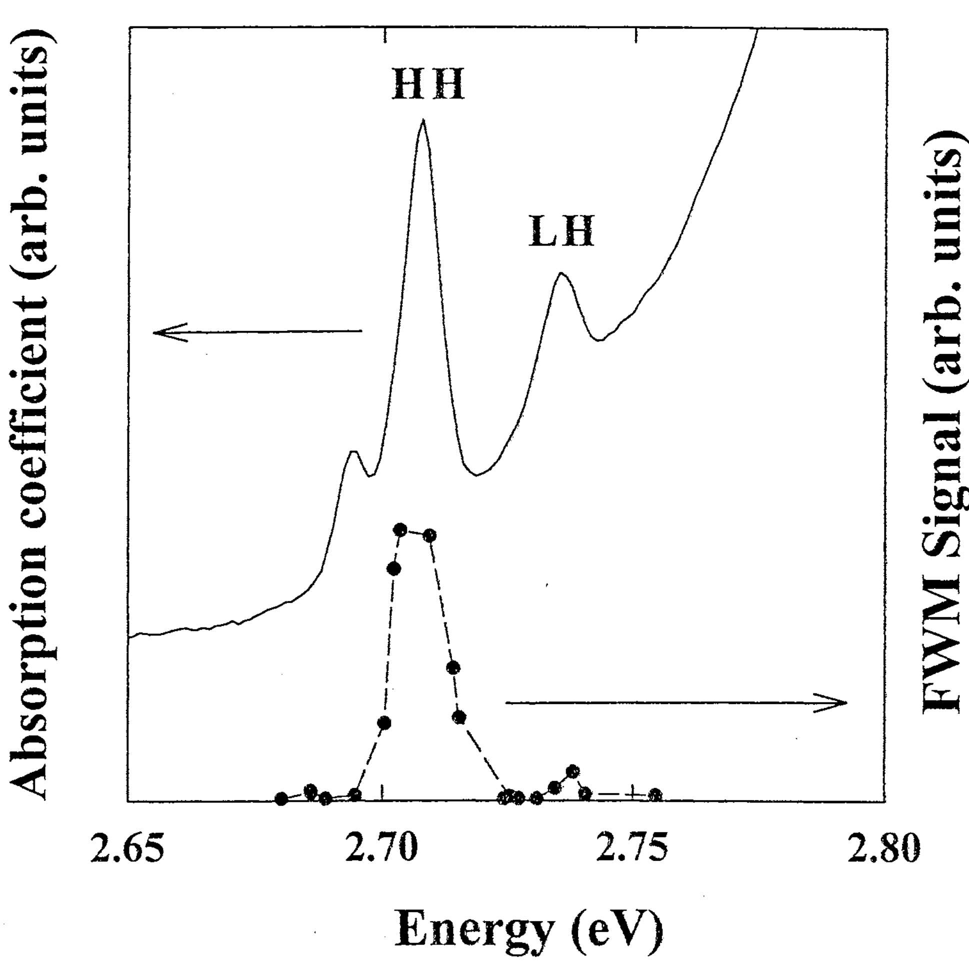

Figure 25. FWM signal as a function of center laser frequency for a ZnCdSe MQW sample. Linear absorption data is also included for reference. Note the strong resonance at the heavy hole (HH) and light hole (LH) excitons.

in the plot for reference. A very strong resonance is observed at the HH exciton at an energy of 2.71 eV and a much weaker peak is observed at an energy of 2.74 eV. The secondary peak also appears in the absorption measurements, and has been assigned to the LH exciton resonance. The strong resonance suggest that the FWM signal comes almost entirely from excitons in both bulk ZnSe and ZnCdSe quantum wells, rather than from free carriers. This is also confirmed by the SR-FWM data for both the ZnCdSe MQW and the ZnSe epilayer shown in Fig. 23. Sharp excitonic resonances with FWHM of 5 meV and 2.8 meV are observed for the MQW and bulk ZnSe epilayer, respectively. From these observations, we conclude that the excitonic contribution completely dominates FWM in ZnCdSe MQW. Higher order signals also display similar behavior, indicating that excitons dominate nonlinear diffracted signals of all orders.

The same resonance phenomenon has been observed in the FWM signal from GaAs QW's and was explained by much faster dephasing of free carriers relative to excitons [40]. This interpretation is confirmed by TI-FWM experiments on the MQW sample when the laser is tuned to the HH resonance, LH resonance or roughly at the edge of the free carrier continuum. Fig. 26 shows TI-FWM when the laser is tuned to the HH exciton (top), LH exciton (middle), or at the free carrier continuum (bottom). Much slower (more than by a factor of 10) decay of TI-FWM at the HH resonance relative to those of LH resonance or free carrier continuum is observed. Therefore, we conclude that at 10 K, there exists at least a factor of 10 difference between dephasing times of HH excitons and those of LH excitons and free carriers. By comparing the decay constant of TI-FWM at the HH resonance and the absorption width, we can readily conclude that the HH exciton is inhomogeneously broadened at 10 K. Since in an inhomogeneously broadened system, the decay constant of TI-FWM is equal to $T_2/4$ [50], T_2 for the HH exciton in Fig. 26 is 4 ps while those of the LH exciton or the free carrier continuum are less than 300 fs. It is interesting to note that the dephasing time of LH exciton is so much shorter than that of HH exciton. The relatively large separation between the HH and the LH excitons, which

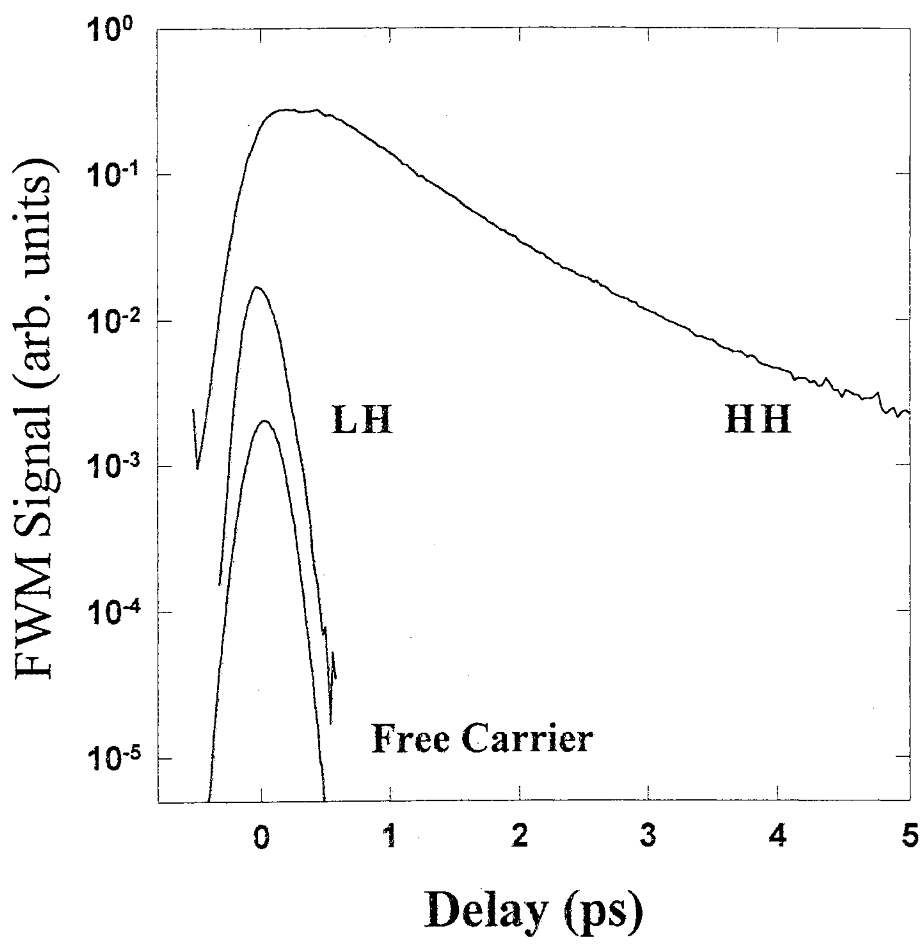

Figure 26. TI-FWM with the laser detuning centered at the HH (top curve), LH (middle curve) and Free Carrier (bottom curve) energies.

is nearly equal to 1 LO phonon energy, is a likely cause for this short dephasing time for the LH excitons.

Negative Time Delay Signal

Negative time delay signals have been observed from an epilayer of ZnSe grown by MBE on a GaAs substrate. A negative time delay signal is a signal which appears when the probe arrives at the sample before the pump. According to the non-interacting two-level model [50], in the absence of a biexcitonic contribution, negative time delay signals should not be seen. To understand negative time delay signal one must consider that even a very weak probe will necessarily induce a polarization response in a material. It is this polarization, which lives on after the probe pulse, which then interacts with the pump beam at a later time to create the negative time delay signal. Thus, at negative time delays we can have the diffraction of polarization instead of the normal diffraction of the electric field of the laser pulse. This can also be described in terms of a coherent exciton-exciton interaction as discussed in Chapter 4. In this model, an exciton interacts not only with the electric field of the laser, but also with the polarization of every other exciton which at negative time delays is created by the probe pulse. Negative time delay signals can also be due to a biexcitonic contribution to the FWM signal. However, the SR-FWM data shown in Fig. 23 show no biexcitonic contribution. Therefore, for these samples and for these experimental conditions, biexcitonic contribution to the FWM signal can be ruled out.

In Fig. 27, FWM signals from ZnSe are plotted as a function of T at several temperatures. For this sample, the relatively small line width (2.8 meV obtained from SR-FWM) makes the observation of negative time delay signals possible since negative time delay signals are only expected from homogeneously broadened samples. Therefore, the existence of negative time delay signal indicates that coherent exciton-exciton interaction plays a role in ZnSe based materials. Based on numerical solutions to the semiconductor Bloch equations [61], for ideal, homogeneously broadened excitons, the decay constant is $T_2/2$ for the positive time delay and $T_2/4$ for the

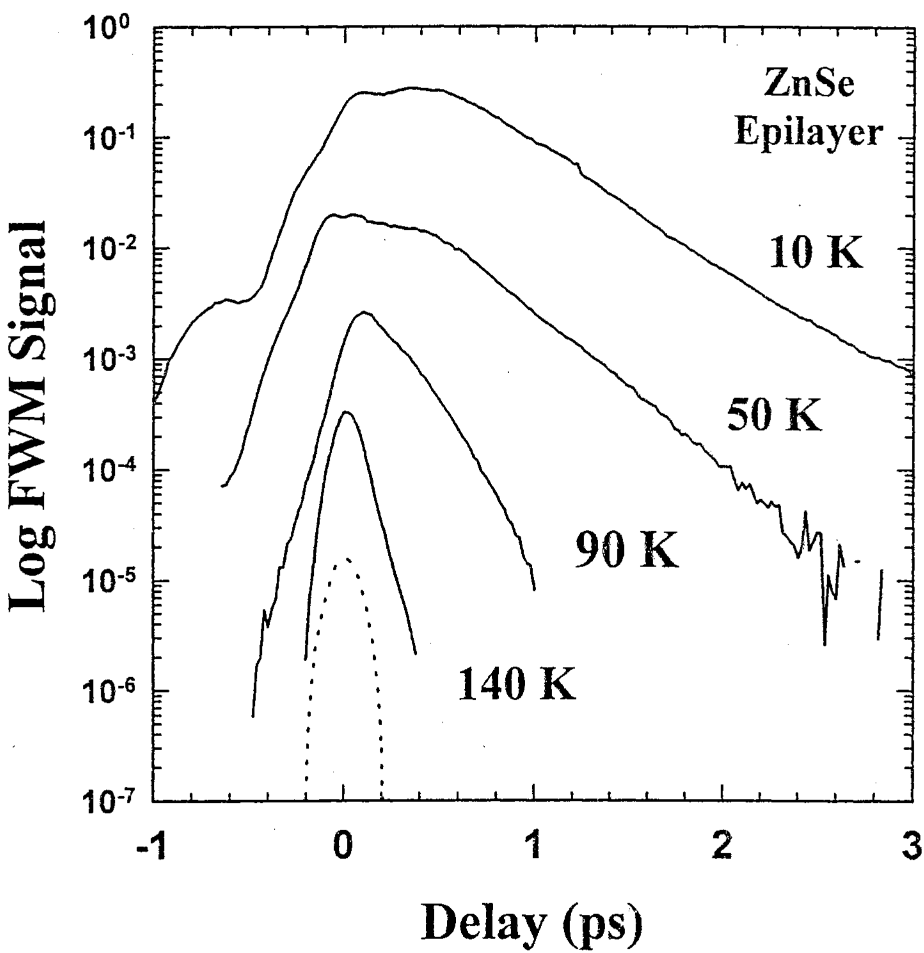

Figure 27. FWM signal as a function of temperature from an epilayer of bulk ZnSe. Note the signal at negative time delays which is due to the coherent exciton-exciton interaction.

negative time delay. Fig. 28 shows the decay constant as a function of temperature for both positive and negative time delays. Note that at low temperature the positive decay constant is several times the negative time delay constant. This is consistent with the interpretation that the system is partially homogeneously broadened. Whether or not the coherent exciton-exciton interaction is the dominant contribution in FWM, as in GaAs quantum wells, cannot be answered at this point due to relatively large inhomogeneous broadening of excitons. In the ZnCdSe quantum wells, negative time delay signals were not observable due to inhomogeneous broadening (5 meV, both from absorption and SR-FWM). However, the contribution of the exciton-exciton interaction scales with the binding energies, therefore exciton-exciton interaction is expected to play an even greater role in MQW's.

Exciton-Phonon Interaction

CT-DFWM is one of the most reliable methods for determining the homogeneous linewidth in a semiconductor. In fact, the homogeneous linewidth can even be determined in the presence of strong inhomogeneous broadening. In this subsection and the next, CT-DFWM is used to measure the homogeneous linewidth as a function of temperature and as a function of exciton density, in order to determine exciton-phonon and exciton -exciton scattering rates, respectively.

As the temperature of a sample is increased, the FWM decay time decreases rapidly due to the scattering of excitons with phonons. The exciton-phonon scattering causes the exciton to scatter from its initial momentum state and the exciton is thus dephased. In Fig. 29, FWM data from the 6x($Zn_{0.88}Cd_{0.12}Se$/ZnSe) MQW are plotted for several lattice temperatures, T_L. The data become time resolution limited at about 200 K so that one would need shorter optical pulses to determine the dephasing time for temperatures above 200 K. The data at each temperature were fit to a monoexponential decay to get the FWM decay time, τ_{FWM}. The monoexponential fit can be done for the data shown in Fig. 27 for the epilayer of ZnSe. Fig. 30 shows the FWM decay rate ($1/\tau_{FWM}$) plotted as a function of temperature for the MQW and the ZnSe epilayer. Two temperature ranges are clearly seen: at low

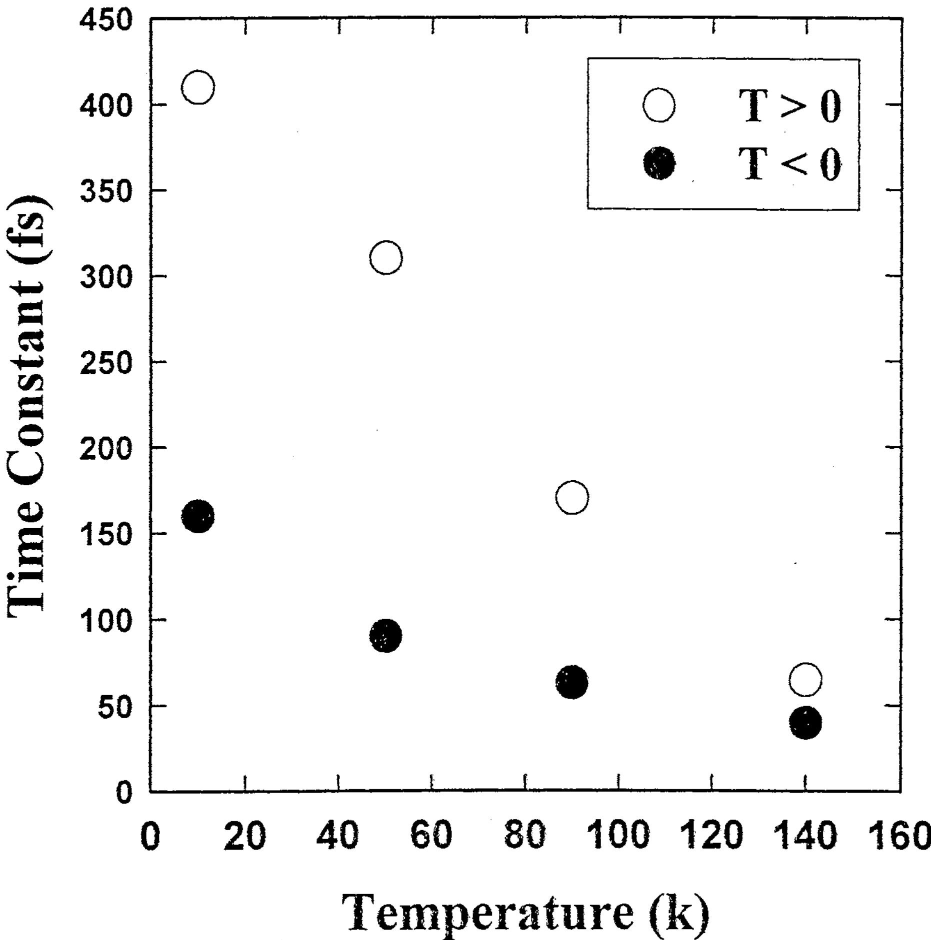

Figure 28. FWM time constants for positive (empty circles) and negative (filled circles) delay for an epilayer of ZnSe. The data in Fig. 27 were fit to monoexponential decays. Note that at 10 K the rise time is about one half the decay time as expected for the coherent exciton-exciton interaction.

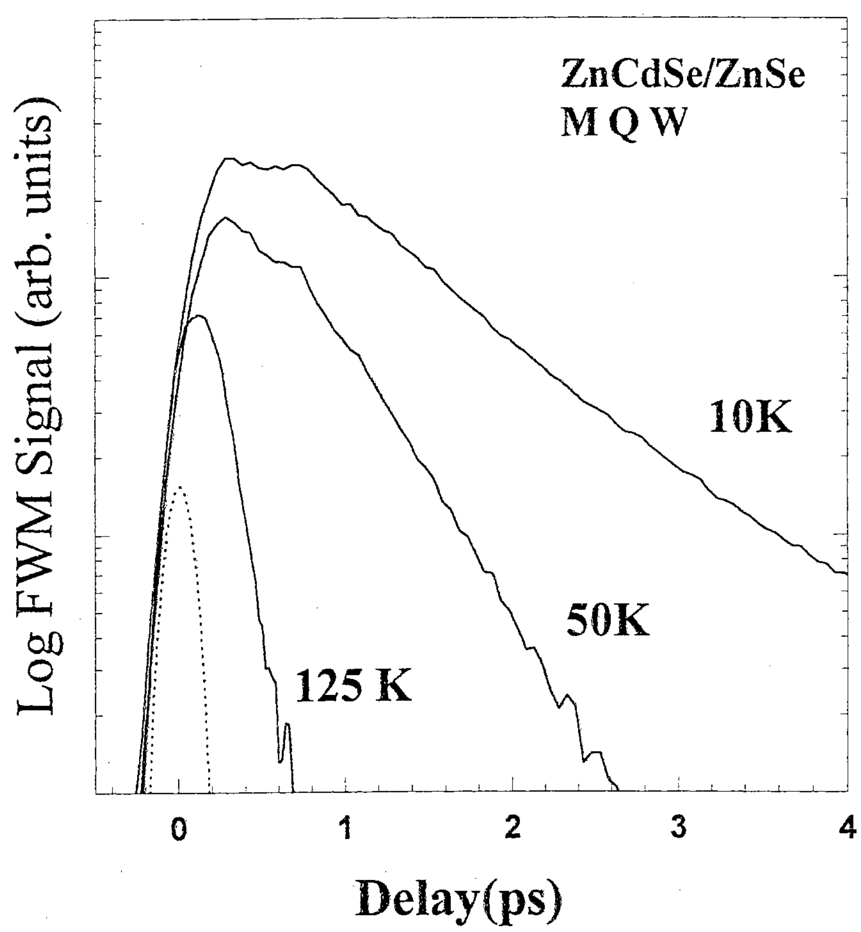

Figure 29. FWM data as a function of temperature for several representative temperatures. The dephasing time decreases with increasing temperature. This is because at higher temperatures there are more thermal phonons to scatter with the excitons and dephase them.

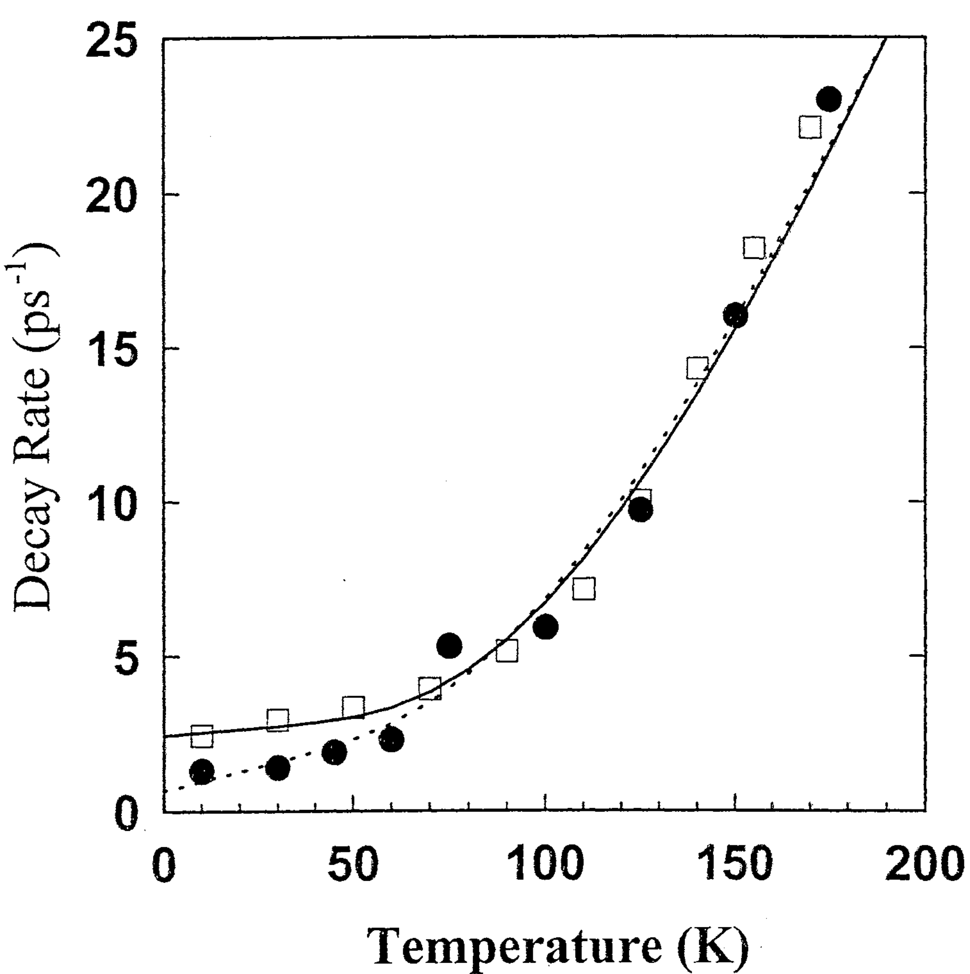

Figure 30. Decay rates of FWM for a ZnSe epilayer and a ZnCdSe MQW sample. The lines are fits to the phonon broadening equation for the bulk (solid line) and MQW (dashed line) samples.

temperatures (<100 K), the rate is roughly linear with T_L, whereas for T_L>100 K, the slope is much larger. This is an indication that below 100 K, acoustic phonon-exciton interaction dominates the dephasing, whereas at higher temperatures, the contribution by optical phonons becomes important. We fit the decay rates with the following phenomenological equation [90]:

$$1/\tau_{FWM} = A + BT_L + \frac{C}{\left\{\exp\left(\frac{E_{LO}}{k_B T_L}\right) - 1\right\}},$$

where E_{LO} is the optical phonon energy and k_B is the Boltzmann constant. Constant A represents the contribution at $T_L = 0$, from impurities or interface roughness. Since the population of acoustic phonons is linear in temperature at low temperature, BT_L represents the contribution due to acoustic phonon interaction. The last term is just a Bose-Einstein population factor times a parameter C which represents the contribution to the FWM signal from excitons scattering with optical phonons. The best fits are obtained with $A = 0.66$ ps^{-1}, $B = 0.025$ ps$^{-1}/K$, and $C = 127$ ps^{-1} for the MQW (dashed line) and $A = 2.44$ ps^{-1}, $B = 0.014$ ps$^{-1}/K$, and $C = 115$ ps^{-1} for the ZnSe epilayer (solid line). These values can be compared with much smaller values reported for a GaAs MQW [40]: $B = 0.007$ ps$^{-1}/K$, and $C = 21$ ps^{-1}. The large B and C values indicate that exciton-phonon interactions are much stronger in ZnSe and ZnCdSe quantum wells.

Exciton-phonon interaction parameters are normally presented in terms of the homogeneous linewidth in meV, however, these values have intentionally been left in terms of FWM decay rate. This is because in order to extract the homogeneous linewidth, one must know if the resonances are predominantly homogeneously or inhomogeneously broadened [50]. Since the absorption line width of excitons in the MQW sample at low temperature is 5 meV, it is clear that they are inhomogeneously broadened at low temperature when the decay constant is around 1 ps. On the other hand, the ZnSe sample, which has a smaller line width of 2.8 meV at low temperatures, has decay constants of 300 fs so that it is partly homogeneously broadened. Thus, at low temperatures, we have to multiply the time constant by 4 to deduce T_2 for the MQW, whereas multiplying the time constant of ZnSe by 2 is reasonable.

On the other hand, at high temperatures, both samples are homogeneously broadened and therefore the time constants should be multiplied by 2 to deduce T_2. From these discussions and the fittings shown in Fig. 30, the exciton-acoustic phonon and exciton-LO phonon interaction parameters for the ZnCdSe MQW sample are 8.3 μeV$/K$ and 81 meV, respectively. While for the ZnSe epilayer, the exciton-acoustic phonon and exciton-LO phonon interaction parameters are 9.2 μeV$/K$ and 75 meV, respectively. The exciton-acoustic phonon coupling constants in both samples are essentially identical, and close to the value obtained for CdTe based quantum wells using FWM [70]. The LO phonon interaction parameter for ZnCdSe MQW is comparable to the values obtained from absorption measurements in ZnCdSe MQW samples grown on GaAs with larger alloy concentration and smaller well widths [74]. The value of the exciton-LO phonon interaction for ZnSe of 75 meV is in good agreement with the lower limit given in Ref. [76] of greater than 60 meV.

The exciton-LO phonon interaction strength is expected to decrease in a quantum well if the exciton binding energy becomes larger than the LO phonon energy since the LO phonons will no longer have the energy to dissociate excitons. We observe roughly that same exciton-LO phonon interaction parameter for both the ZnCdSe MQW and the ZnSe Epilayer. Thus, our results suggest that the binding energy of HH excitons in our MQW is smaller than 1 LO phonon energy, so that the exciton-LO phonon scattering is essentially bulk-like. In our samples, a secondary peak, with a very fast dephasing time, appears 29 meV above the HH exciton. This suggests a possibility of scattering between the HH and the LH excitons. If such scattering exists, exciton-LO phonon scattering is not necessarily a definitive indication that the excitons scatter into the free carrier continuum by the absorption of one LO phonon. Exciton-LO phonon scattering, between HH and LH excitons or between n=1 and n=2 HH excitons, is a subject that needs further attention before a conclusive statement can be made on the binding energies relative to the LO phonon energy in these quantum wells.

Exciton-Exciton Interaction

It is also possible to study the homogeneous linewidth as a function of excitation density. As the density of excitons increases, the population of excitons dephases more quickly due to scattering with other excitons. This is much different than the *coherent* exciton-exciton scattering discussed earlier. For the coherent exciton-exciton scattering, an exciton is thought to interact with the coherent polarization of every other exciton. The type of exciton-exciton scattering discussed in this subsection is due to the scattering of two excitons.

In order to study exciton-exciton interaction, the exciton density must be estimated for a given laser power. One large source of error in estimating the exciton density results from inaccurate determination of the FWM focal spot size. To accurately determine our spot size, we placed a sensitive CCD detector designed for beam analysis in the focal plane of our lens where the beams overlap. A three dimensional plot of the beam profile at this position is shown in Fig. 31. The spot diameter for these experiments at FWHM was 60 μm with $1/e^2$ of the energy within a 100 μm diameter. Our beam spot was slightly elliptical with a FWHM semimajor axis of 65 μm and a FWHM semiminor axis of 55 μm. With this accurate information on the photon density, the exciton density was estimated from the linear absorption data shown in Fig. 18 for each excitation density.

Fig. 32 shows the FWM signal at several different excitation densities. The data at each density can be fit to a monoexponential decay to get the FWM decay time. By assuming inhomogeneous broadening we can get the homogeneous linewidth from the relation $\Gamma_{\text{hom}} = 2\hbar \,/\, T_2$. Fig. 33 shows the homogeneous linewidth as a function of density up to a density associated with the highest available second harmonic power. For densities lower than those shown in Fig. 33 the FWM signal was too weak to accurately determine the homogeneous linewidth. Note that the densities given are two dimensional densities appropriate for a quantum well since excitons confined to the well are expected to form a single layer of excitons. That is, there is no room for a double layer of excitons in a very thin quantum well.

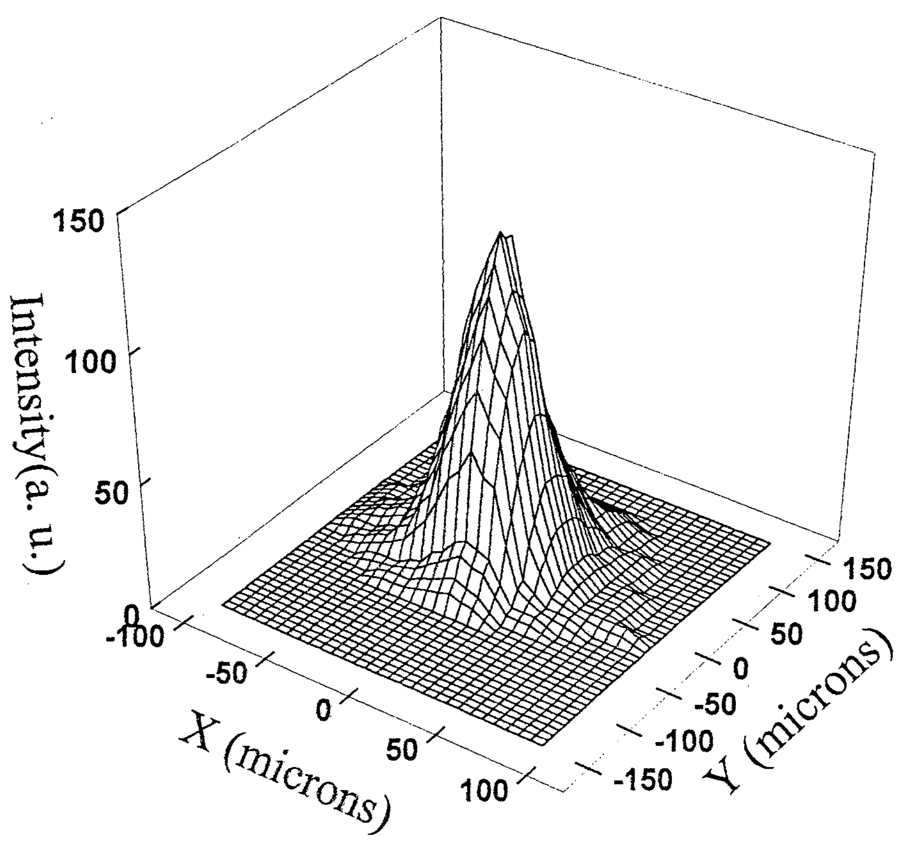

Figure 31. Laser beam profile measured with a CCD camera. In order to determine the exciton density, the laser beam focal spot size must be known.

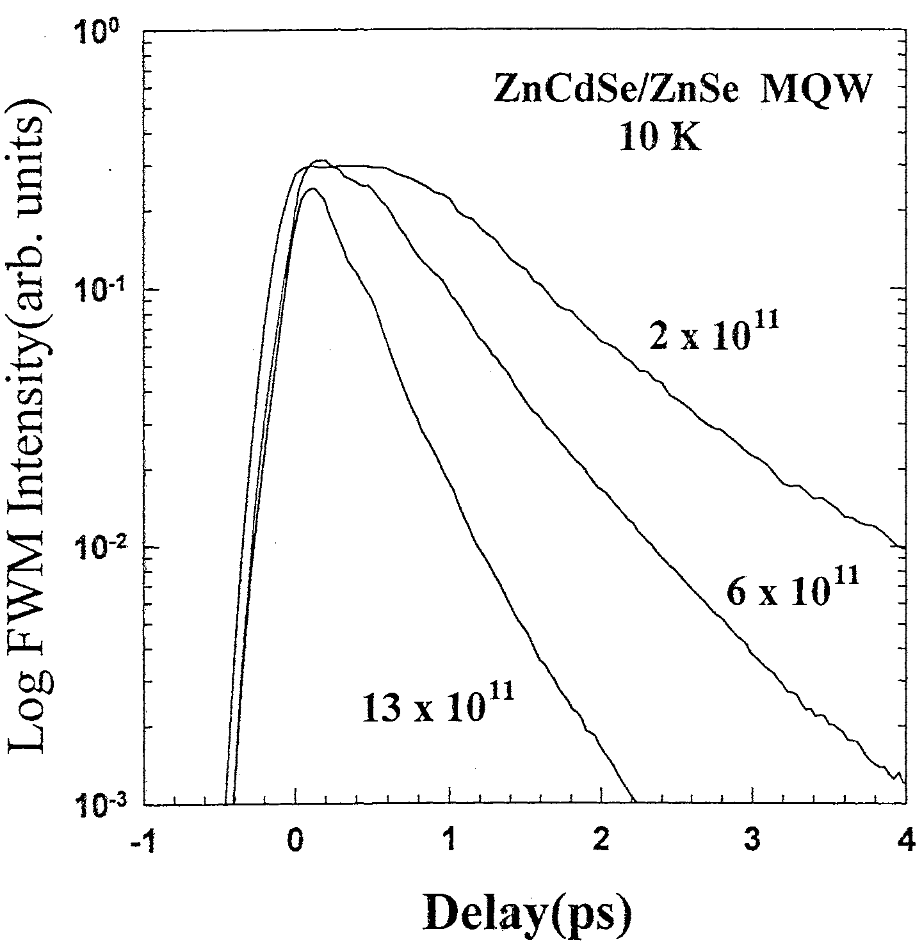

Figure 32. FWM signal plotted for several different exciton densities. Excitons dephase more quickly at higher excitation densities due to increased scattering with other excitons.

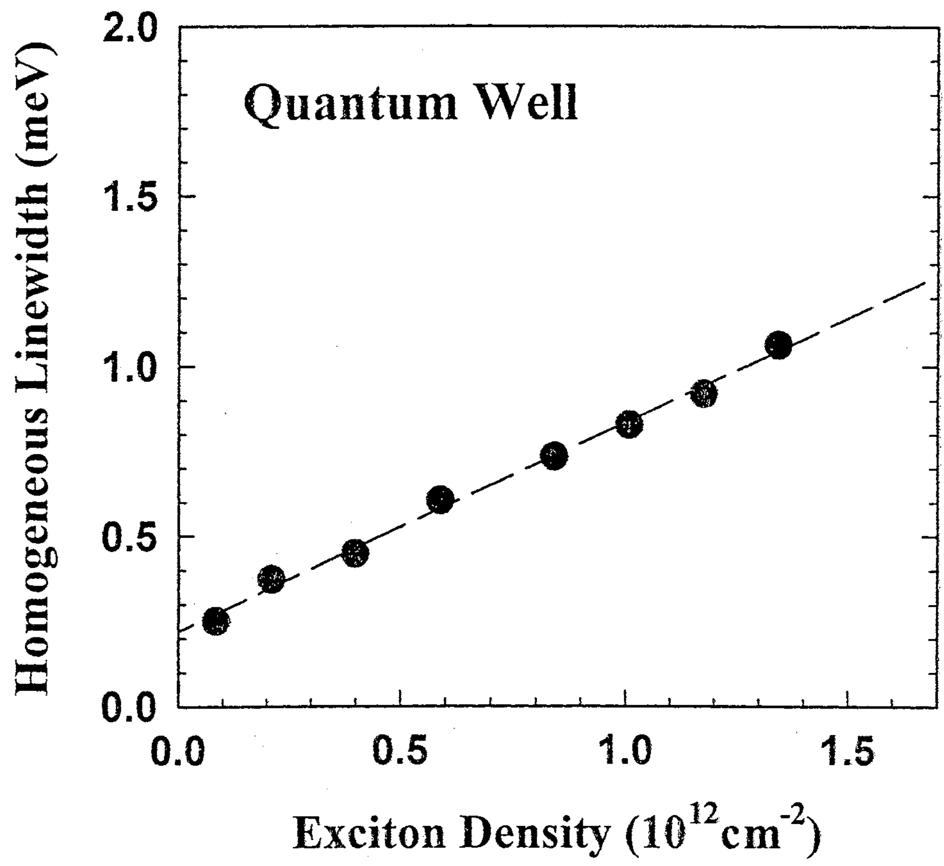

Figure 33. Homogeneous linewidth at 10 K plotted as a function of exciton density for a ZnCdSe multiple quantum well sample. The dashed line is a best fit to a linear density dependence.

The homogeneous linewidth can be well described by a linear density dependence as expected at low density [91]. The data were fit to the following functional form:

$$\Gamma_{\text{hom}}(N) = \Gamma(N=0) + \gamma_{xx} a_B^2 E_B N,$$

where $\Gamma(N=0)$ is scattering at zero density due to scattering with impurities, phonons or other carriers besides excitons. γ_{xx} is a dimensionless parameter which describes the strength of the exciton-exciton interaction, a_B is the exciton Bohr radius ($\approx$ 30), and E_B is the exciton binding energy ($\approx$ 28 meV for this sample structure). The best fit line gives a parameter of γ_{xx} = .25 for this sample. This compares favorably to similar measurements that were performed for CdMnTe/CdTe MQW samples where a value of γ_{xx} = .16 was obtained [70]. Since the differences in material properties are taken into account by the exciton Bohr radius and the exciton binding energy γ_{xx} is expected to be the same for all materials. The differences between the values for the ZnCdSe and the CdMnTe material systems can easily be accounted for by errors in determining the exciton binding energy and the Bohr radius. However, these measurements were first performed for the GaAs material system and a result of γ_{xx} = 1.5 was obtained [65]. This is a factor of four larger then for the ZnCdSe data presented here and almost a full order of magnitude larger than for the CdMnTe samples. This large difference is not yet understand. It is perhaps due to the free carriers which are generated when performing FWM on GaAS-based samples. The small exciton binding energy in GaAs makes it difficult to excite excitons without exciting free carriers. Free carrier are known to be more efficient at dephasing excitons. Therefore, free carriers may be contributing to the homogeneous linewidth in the experiments on GaAS-based materials while for materials with larger band gaps it is easier to excite excitons without free carriers. Furthermore, it is shown below that the extent to which an exciton is localized can effect the exciton scattering rates. Further experimental and theoretical work needs to be done to fully understand why different exciton-exciton interaction parameters are observed for different material systems.

Localization Study

Using CT-DFWM, interaction rates, such as exciton-acoustic phonon or exciton-exciton, can be determined by measuring the dephasing time under appropriate conditions. This dephasing time can be long for an exciton with a wave function that is confined to some spatial region, whereas an exciton with an extended wave function tends to dephases more rapidly [92]. Many experimental techniques are sensitive to exciton localization including resonant Raleigh scattering [93], wave mixing [94,95], and spectral hole burning [94,96]. In this subsection, exciton localization will be studied using femtosecond FWM.

In semiconductor QWs, well width fluctuations can lead to inhomogeneous broadening of the excitonic transition [97]. By using chemical lattice imaging, this type of well width fluctuation has been observed in GaAs/AlGaAs QWs [98]. Depending on the dimension of the well width fluctuation relative to the exciton diameter or intrinsic coherence length, excitons on the low energy side of the transition can be affected by the potential well created by the well width fluctuations [92–96,99,100]. As mentioned earlier, dephasing times are expected to increase for excitons which are localized. One mechanism for the dephasing of localized excitons is by phonon assisted migration. During this process, an exciton loses its phase coherence by absorbing or emitting an acoustic phonon while hopping to another localization site [101]. Exciton scattering rates can also be affected by exciton localization. In this study we will show that exciton-exciton scattering is much lower for excitons which are localized compared to those which are extended.

The multiple quantum well (MQW) samples used in this study were grown by molecular beam epitaxy to have six 50 layers of $Zn_{0.88}Cd_{0.12}Se$ as the well material and ZnSe for the barrier. The first sample (sample A) has a HH exciton linewidth of about 6 meV (FWHM) near zero delay as determined by spectrally resolved FWM and linear absorption data. Data from this sample has been shown in an earlier section. The second sample (sample B) has a somewhat larger FWM linewidth of about 10 meV (FWHM) near zero delay. Although the samples were grown to have

similar parameters, the heavy hole excitonic transitions in these samples differ in energy by about 45 meV. This energy difference is probably due to a slight differences in well widths and Cd concentrations between the two samples. The large linewidths of these samples as well as the relatively long decay times of FWM indicate that the HH excitonic transitions are predominantly inhomogeneously broadened.

Fig. 34 shows typical time-integrated and spectrally-integrated measurements of the diffracted intensity as a function of delay for the two different samples. These two samples have similar dephasing times, but the lineshape of the TI-FWM signal for each sample is very different. Sample A has a monoexponential decay with a decay time at 10 K of about 500 fs. This sample has only one well-defined decay time which indicates that the homogeneous linewidth is constant across the inhomogeneous linewidth. Sample B, on the other hand, consists of many decay times and cannot be fit to a single exponential, suggesting that the excitonic transition is broadened in a more complicated manner. The data for sample B can be explained by assuming that the homogeneous linewidth is changing across the inhomogeneous linewidth. This interpretation is consistent with localization due to potential fluctuations from well width variations.

To further investigate the differences in these samples, the dephasing time of the excitons was also studied for various points across the inhomogeneous linewidth. For this study the exit slit of the spectrometer was used to select a bin of energy on the inhomogeneous linewidth. For our experimental apparatus, an energy bin size of 1 meV was required to give an acceptable signal to noise ratio. Typical data for each sample are shown in Fig. 35 (a) and (b). Sample A shows very little change in the dephasing time as a function of energy. Sample B, on the other hand, shows a dramatic change in the decay rate for data above and below the exciton line center. Excitons on the high energy side have a decay time of about 200 fs, whereas excitons on the low energy side dephase with a characteristic time of 1 ps. Fig. 36 (a) and (b) show the decay rate plotted along with SR-FWM data for each sample. Although the large linewidth of sample A (6 meV) and the decay constant of 500 fs indicate that it is inhomogeneously broadened with a homogeneous linewidth of about 0.6

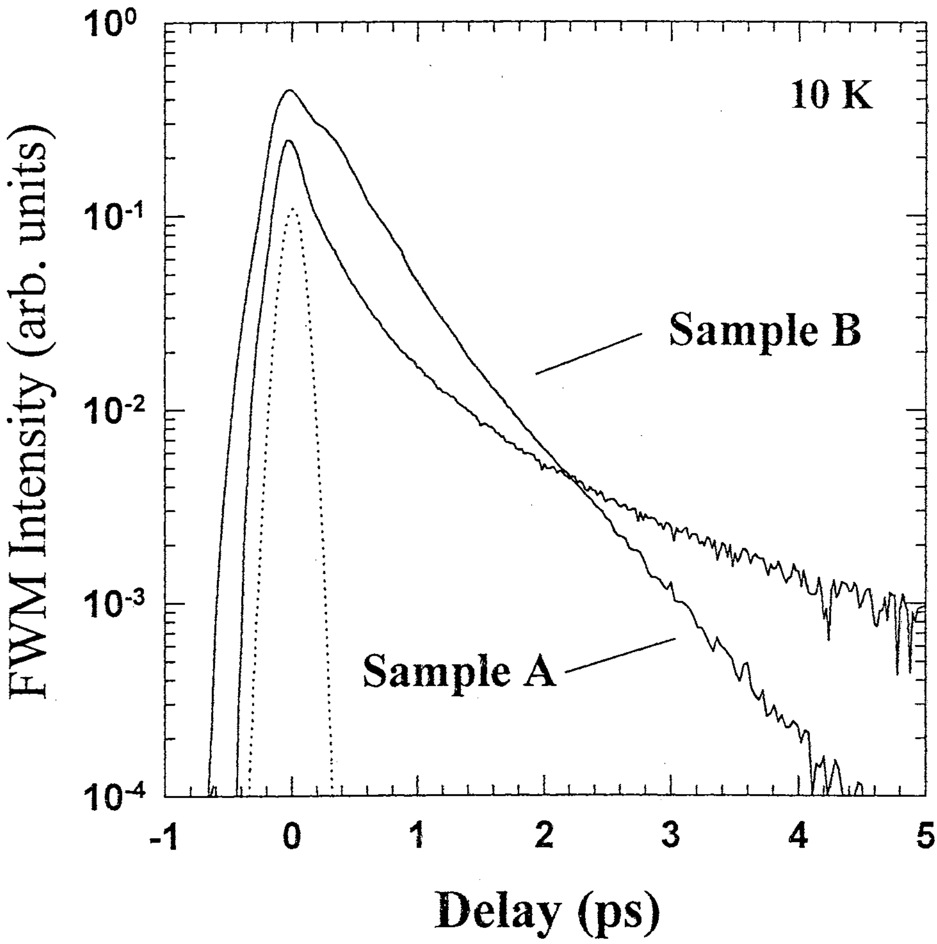

Figure 34. FWM data for samples A and B at 10 K together with the cross-correlation trace of the pulse. Sample A shows a monoexponential decay while the data from sample B consist of many decay constants.

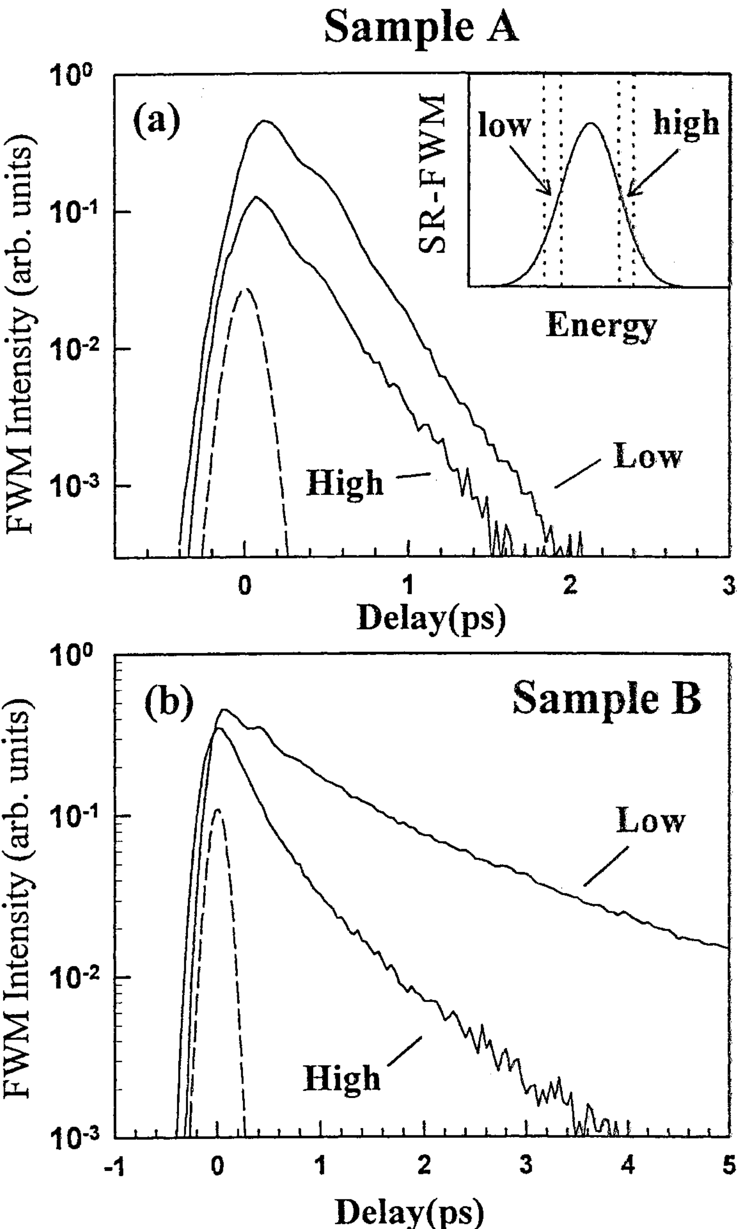

Figure 35. FWM data on the high and low energy sides of the excitonic resonance for (a) sample A and (b) for sample B. Sample A shows no change while sample B shows a large change in the decay time when going from the high to the low energy side.

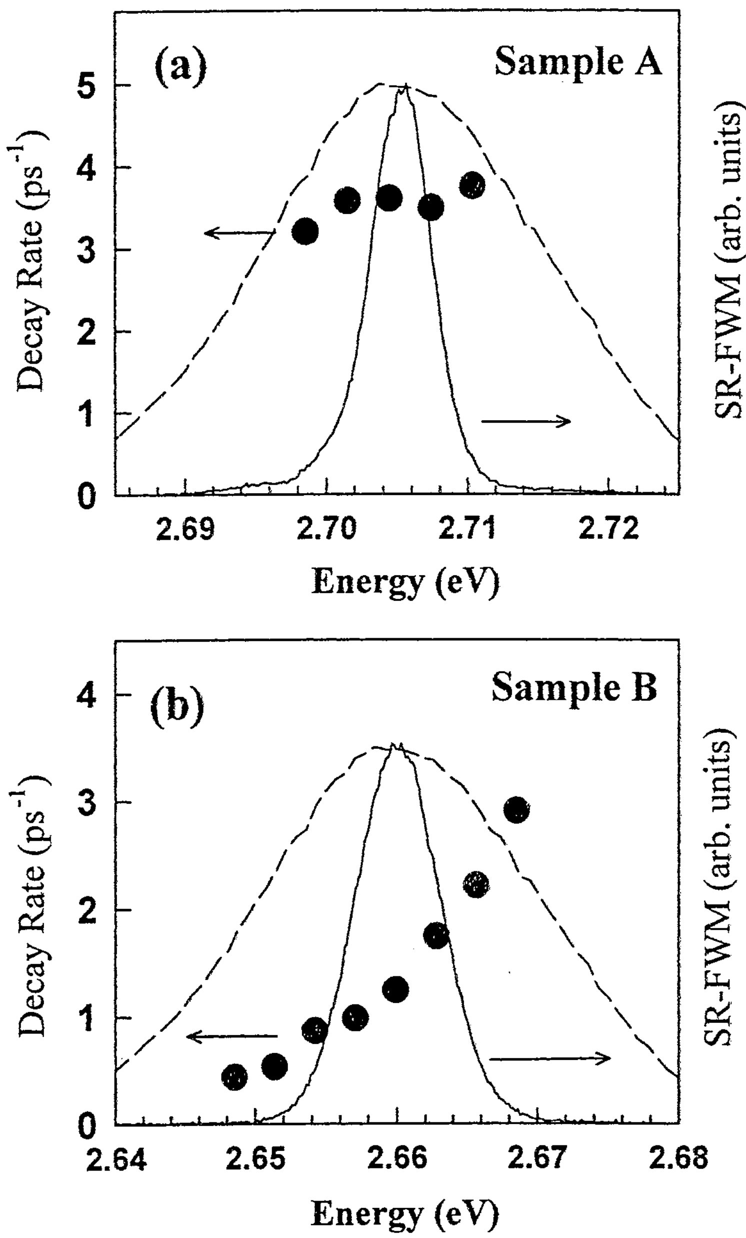

Figure 36. Decay Rates for samples (a) A and (b) B plotted as a function of photon energy together with the SR-FWM lineshapes. The dashed lines show the spectral shape of the excitation laser pulses.

meV, very little change in the dephasing time was observed as a function of energy. On the other hand, for sample B, there exists nearly a factor of ten change across the linewidth, implying that the excitons on the low energy side are more localized.

A direct comparison of data from these samples is difficult, since the samples were grown at different times, on different MBE machines, and with different sample substrates (Sample A on ZnSe; Sample B on GaAs). One possible explanation for the difference is that one sample has much larger regions where the well width is constant. Sample B, with its larger linewidth and inherent substrate-induced strain, may have potential islands which are small enough in area in the plane of the well to more effectively localize excitons. Sample A, on the other hand, may have islands that are larger in spatial extent and hence localize the excitons to a lesser degree. However, the large differences between samples makes a comparison difficult without further data from these samples.

As mentioned above, exciton scattering rates are expected to be different for localized excitons compared to excitons with more extended wave functions. For sample A, the dimensionless parameter describing exciton-exciton interaction was determined in the previous section to be $\gamma_{xx} = .25$. A similar analysis was performed on sample B to determine exciton-exciton interaction rates. Density dependent FWM was performed for sample B on the high and low energy sides of the excitonic resonance in order to determine if localization affects exciton-exciton scattering. Fig. 37 shows the homogeneous lifetime for sample B as a function of exciton density for data taken on the high and low energy side of the excitonic resonance together with the data taken from sample A. The dimensionless parameters are 0.37 and 0.04 for energies above and below line center, respectively. It is clear from this fit, that for sample B, there is almost an order of magnitude difference in the interaction rates for different positions along the exciton linewidth. These data show that excitons localized on the low energy side interact much less than the more extended excitons on the high energy side. Excitons which are more extended are expected to interact more strongly with each other. This is simply because extended excitons exist in

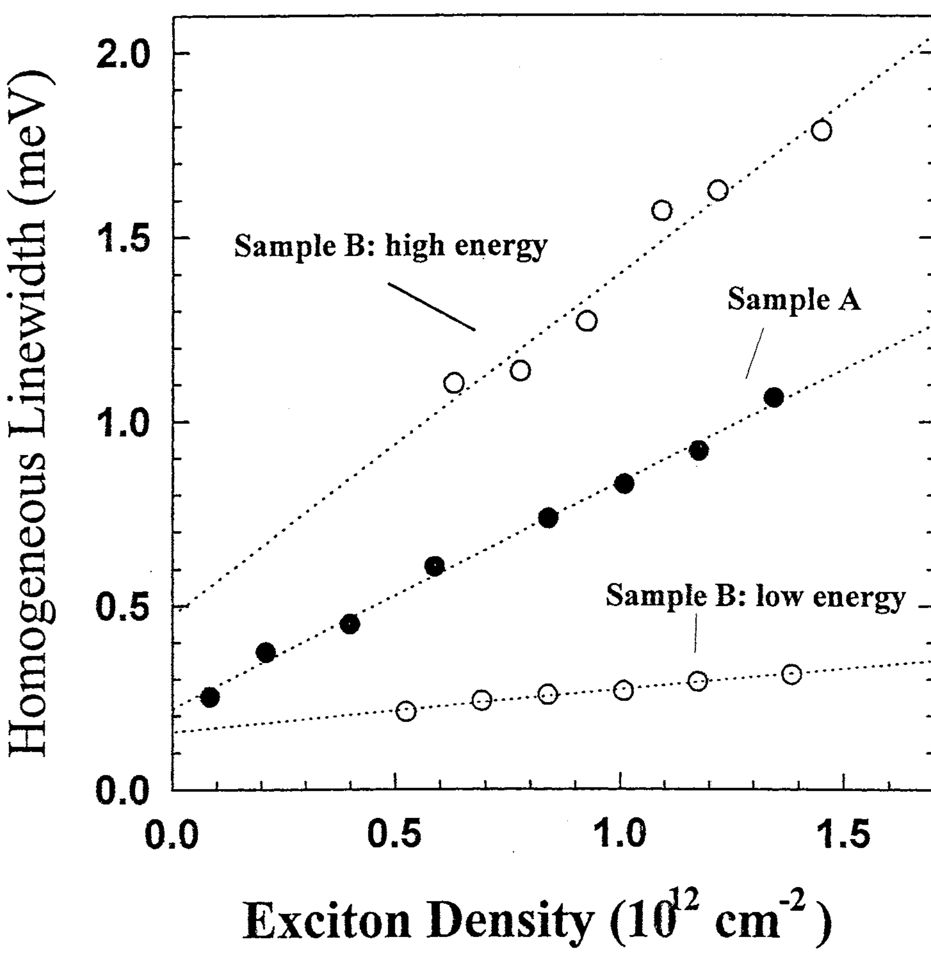

Figure 37. Homogeneous linewidth plotted as function of exciton density for Sample B for energy positions 4 meV above and below the line center. Data from sample A are shown for reference as well as the best fit lines to a linear density dependence.

a larger spatial region and therefore have a larger cross section for interaction with other excitons.

Conclusions

In conclusion, we found very strong nonlinear signals, up to the 13th order (or 14 wave mixing), in femtosecond two-beam, self-diffraction experiments on ZnSe and ZnCdSe quantum wells. The FWM for all orders is completely dominated by excitonic resonances. Negative time delay signals were observed from an epilayer of ZnSe which is attributed to the coherent exciton-exciton interaction. The coherent exciton-exciton interaction was shown to play an important role in the ZnSe material system as it does for GaAs-based materials. Exciton-LO phonon interaction was shown to be much stronger in ZnSe-based material compared to GaAs-based materials. This is due to the strong polar nature of ZnSe which gives rise to a large Frohlich interaction between LO phonons and excitons. No decrease in exciton-LO phonon interaction was observed for the MQW samples used in this work indicating that the binding energy of the excitons is smaller than the LO phonon energy of 31 meV. Exciton-exciton interaction rates were determined and compared to other material systems. The exciton-exciton scattering rate determined in this work was comparable to the CdMnTe/CdTe material system yet smaller than that determined for GaAs-based materials. Localization was also studied by performing CT-DFWM at different positions across the excitonic linewidth. For one sample, excitons were shown to be localized on the low energy side while the excitons on the high energy side had wave function that were more extended. Finally, the exciton-exciton interaction rate was shown to be much smaller for excitons which are localized.

CHAPTER VI

FOUR-WAVE-MIXING IN GaN EPILAYERS

Introduction

As mentioned in Chapter 1, GaN has been attracting a great deal of attention due to its application in blue and UV LEDs and laser diodes. Since InN, GaN, and AlN, have direct band gaps of 1.9 eV, 3.4 eV and 6.1 eV, respectively, GaN can be alloyed with In or Al to fabricate optoelectronic devices operating over an extremely large wavelength range. Due to its high chemical, thermal, and mechanical stability, GaN has great potential for use high power, high temperature electronics or in hostile environments where rugged high temperature electronic sensors are needed.

Although the optical properties of GaN were studied in the early 70s [24,102,103], in the last decade GaN grown by a variety of techniques has been studied by many research groups using linear spectroscopic techniques such as photoluminescence, photoreflection, absorption and reflection [104,28,31,105,31,33]. Comparatively little experimental work has been done on the nonlinear optical properties of GaN [106–109], and, specifically, only a few authors have presented work done on excitons in GaN in the femtosecond coherent regime [43,110].

In this chapter, the results are presented from a femtosecond coherent spectroscopic study of intrinsic free excitons in a high quality GaN epilayer. The first section is devoted to measuring the homogeneous linewidth as a function of temperature. Spectrally-resolved (SR) as well as time-integrated (TI) four-wave-mixing (FWM) measurements are performed at several temperatures in order to show that the excitons in this sample are nearly homogeneously broadened even at low temperature. Exciton-phonon interaction parameters are then derived from the temperature

dependent data. The second section describes the strong beating that has been observed in the TI-FWM signal. The beat period is shown to correspond to the energy separation between the A and B excitonic resonances. TI-FWM is performed at various positions across the A exciton linewidth in order to show that the beating is due to the creation of a true superposition state and not to, so-called, polarization interference [111]. A shift is observed in the phase of the beating when changing from collinear to cross-linear input laser polarizations. This phase shift was previously observed for heavy hole (HH)- light hole (LH) beating in a GaAs QW sample [112]. Schmitt-Rink et al. [112] solved the optical Bloch equations in the ultrashort-pulse limit in order to theoretically predict this phase shift for the GaAs material system. The results of a very similar calculation are presented here which predict the same type of phase shift for beating between the A and B excitons in wurtzite GaN.

Experiments were performed in the reflection geometry using the second harmonic of a mode-locked Ti:sapphire laser (150 fs) operating at 710 nm. The laser detuning was set to resonantly excite the excitonic resonances. Two beams with wave vectors $\mathbf{k}_1$ and $\mathbf{k}_2$ are focused onto a 100 μm spot on the sample and the FWM signal diffracted into the $2\mathbf{k}_2 - \mathbf{k}_1$ phase-matched direction is measured as a function of the delay between pulses. The details of the experimental set up are described in chapter 4. The sample used in the study was a single-crystal 7.2 μm thick epilayer of wurtzite GaN which was grown by metalorganic chemical vapor deposition on a sapphire substrate. The sample had a compensated n-type carrier concentration of less than 10^{16} cm^{-3}. The valence band degeneracy is lifted in wurtzite crystals by the crystal field splitting so that even for strain-free GaN we have three valence bands A, B, and C. For propagation of light parallel to the GaN c-axis, excitation of the C excitonic resonance is not allowed due to symmetry and we are primarily concerned with the A and B excitons. For thick GaN epilayers grown on sapphire, the substrate-induced strain is almost fully relaxed, but there is residual compressive strain due to differences in lattice parameters between the GaN and the sapphire as well as differences in coefficients of thermal expansion [113]. Thus, the splitting between the A and B excitons can vary slightly from sample to sample. For the

sample used in the study, the splitting is 7.3 meV as measured by CW reflectance and SR-FWM.

Linewidth Analysis

In Fig. 38, TI-FWM data are shown at three different temperatures (T=10, 70, and 190 K). The laser was tuned near resonance with the B exciton, and the weak beating at 10 K is a result of the excitation of a small A exciton component. At 190 K, the FWM signal is nearly time-resolution limited. The decay time at each temperature was fit to a single exponential decay to determine the decay rate as a function of temperature. The homogeneous linewidth can be determined from the relation $\Gamma_{hom} = 2\hbar/T_2$, where T_2 is the pure dephasing time. In order to determine T_2, we need to know if the resonances are predominantly homogeneously or inhomogeneously broadened. This is because the FWM decay time τ_{FWM} is equal to $T_2/2$ in the homogeneously broadened limit and $T_2/4$ in the inhomogeneously broadened limit [50]. As discussed below, SR-FWM is used to show that the excitonic resonances studied here are nearly homogeneously broadened. Fig. 39 shows the homogeneous linewidth plotted as a function of temperature assuming homogeneous broadening. Initially, the rate is linear with T, but begins to be superlinear starting from about 150 K. This indicates the dominance of the acoustic phonons as the scattering mechanisms for the dephasing of excitons at low temperature. At higher temperature, it is expected that optical phonons begin to contribute. We fit the homogeneous linewidth data in Fig. 2b to the following standard formula [90,40]:

$$\Gamma\left(T_L\right) = \Gamma_0 + \gamma_{ph} \cdot T_L + \frac{\Gamma_{LO}}{\left[\exp\left(\dfrac{E_{LO}}{k_B T_L}\right) - 1\right]} \tag{59}$$

where Γ_0, γ_{ph}, and Γ_{LO} are constants to be determined from the fit, and E_{LO} and k_B are, respectively, the optical phonon energy of GaN (91.7 meV) and Boltzmann's constant. The best fit is the solid line in Fig. 1b, achieved with the fitting parameters: $\Gamma_0 = 2.4$ meV, $\gamma_{ph} = 16$ meV/K, and $\Gamma_{LO} = 390$ meV. These values are much larger than those for GaAs and GaAs quantum wells [40]. This is not so surprising, for GaN

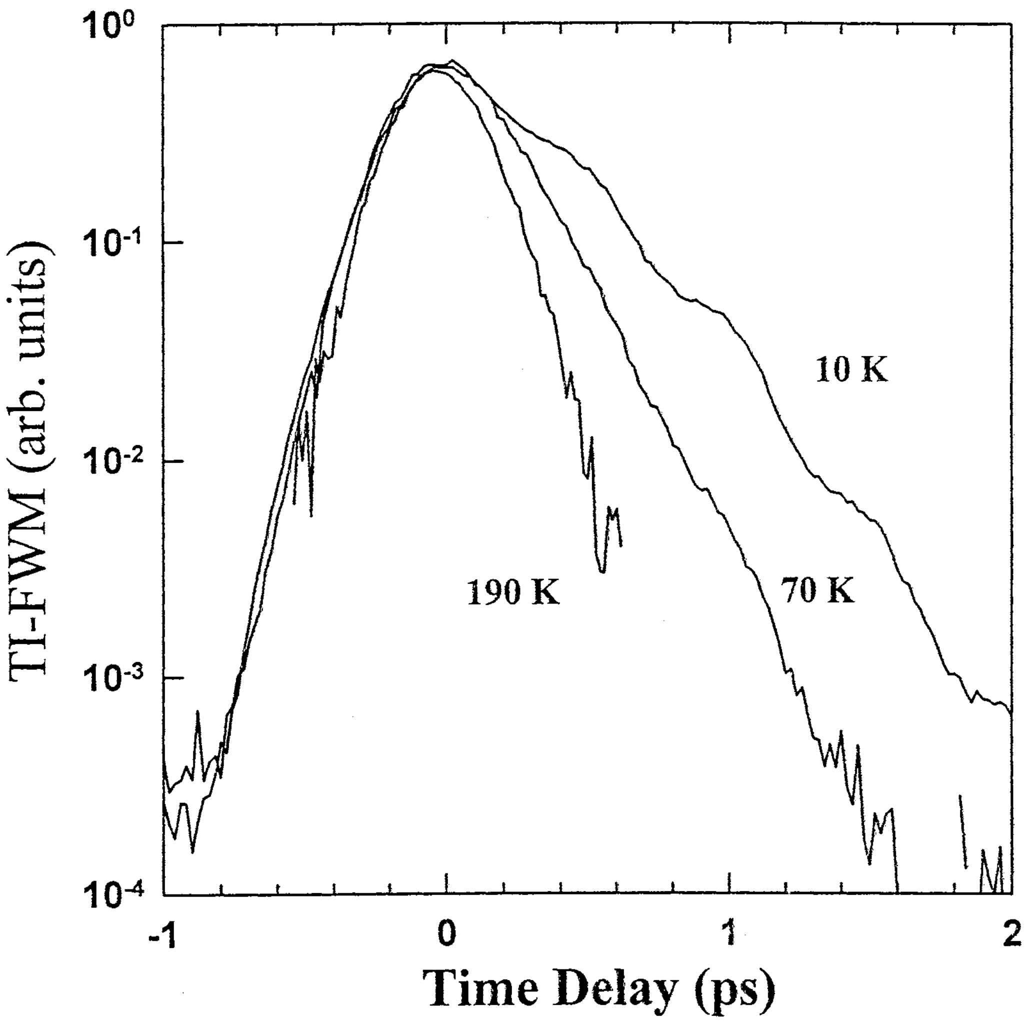

Figure 38. Time-integrated four-wave-mixing (TI-FWM) signal in the reflection geometry near the B exciton resonance at 10, 70, and 190 K for a 7.2 μm epilayer of GaN grown on Sapphire.

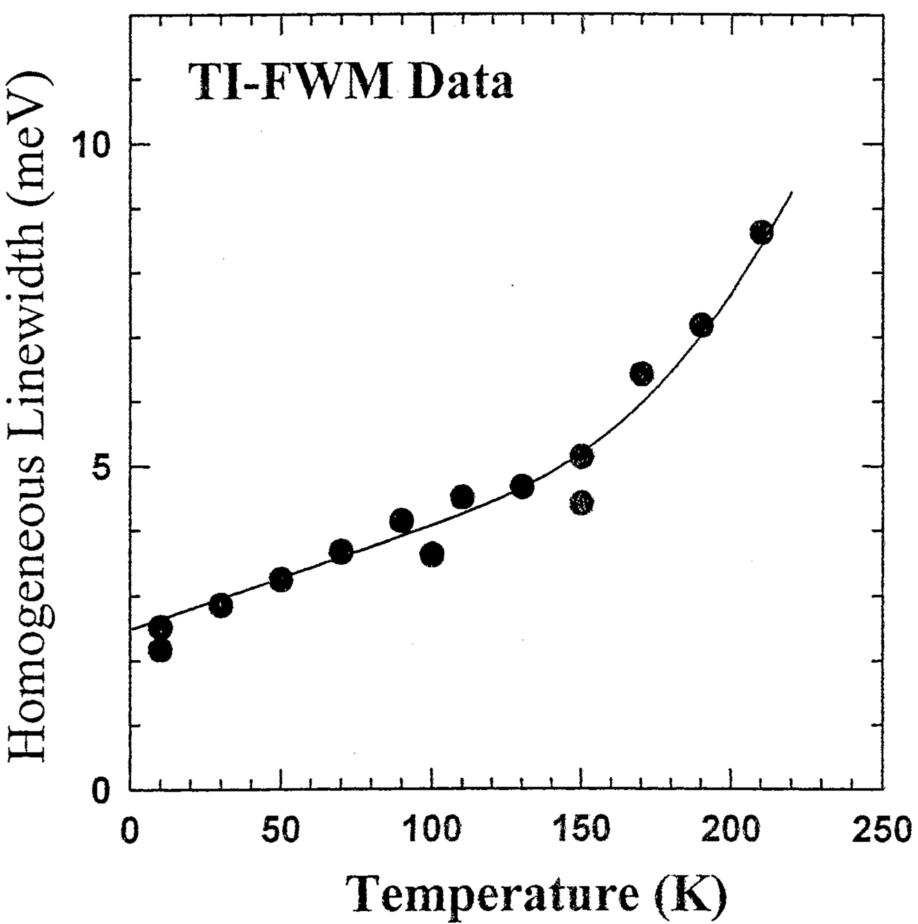

Figure 39. Homogeneous linewidth derived from TI-FWM data plotted as a function of temperature. The solid line is a least-squares fit to Eq.(59).

has larger effective masses for both electrons and holes in comparison with GaAs, and thus a much larger density of states. On the other hand,The density of states of GaN is comparable to that of ZnSe and ZnCdSe quantum wells, whereas Γ_{LO} is still much larger than that of ZnSe and related materials [41]. This is an interesting point, for the density of states of ZnSe as well as its polarity are comparable to those of GaN. The much larger Γ_{LO} for GaN should in part be due to the much larger E_{LO} of GaN in comparison to ZnSe (91 vs 30 meV). In addition, it is possible that a larger deformation potential interaction, which may account for a significant fraction of Γ_{LO} in addition to the Fröhlich interaction, is responsible for the larger Γ_{LO}.

To determine whether the excitons are homogeneously or inhomogeneously broadened, we performed SR-FWM. The advantage of SR-FWM is that it can give the exciton linewidths without any background, which plagues the analysis of absorption experiments. In addition, for high quality, relatively thick epilayer samples, it is virtually impossible to perform absorption. In Fig. 40, SR-FWM data at zero delay are plotted at several temperatures. Both the A and B excitons are clearly present, and the SR-FWM data shown in Fig. 40 represent a very clear demonstration of the A and the B excitons without the interference of bound excitons that make the interpretation of photoluminescence spectra difficult. The SR-FWM linewidth at 10 K, the lowest temperature of our experiments, is about 2.5 meV for the B exciton, and about 2.1 meV for the A exciton. From TI-FWM and the fit shown in Fig. 1a, the homogeneous linewidth in the low temperature limit is about 2.4 meV assuming homogeneous broadening, and 1.2 meV assuming inhomogeneous broadening. Therefore, even in the low temperature limit, the minimum homogeneous linewidth of our excitons is about half the total linewidth observed in SR-FWM. On the other hand, the observed linewidth is nearly equal to what is expected in the homogeneously broadened limit. At higher temperature, there is no doubt that the excitons we probe by FWM are predominantly homogeneously broadened. From these observations, we conclude that our excitons can be considered mostly homogeneously broadened even at low temperature.

Fig. 41 shows the SR-FWM linewidth of the B exciton obtained from a fit to

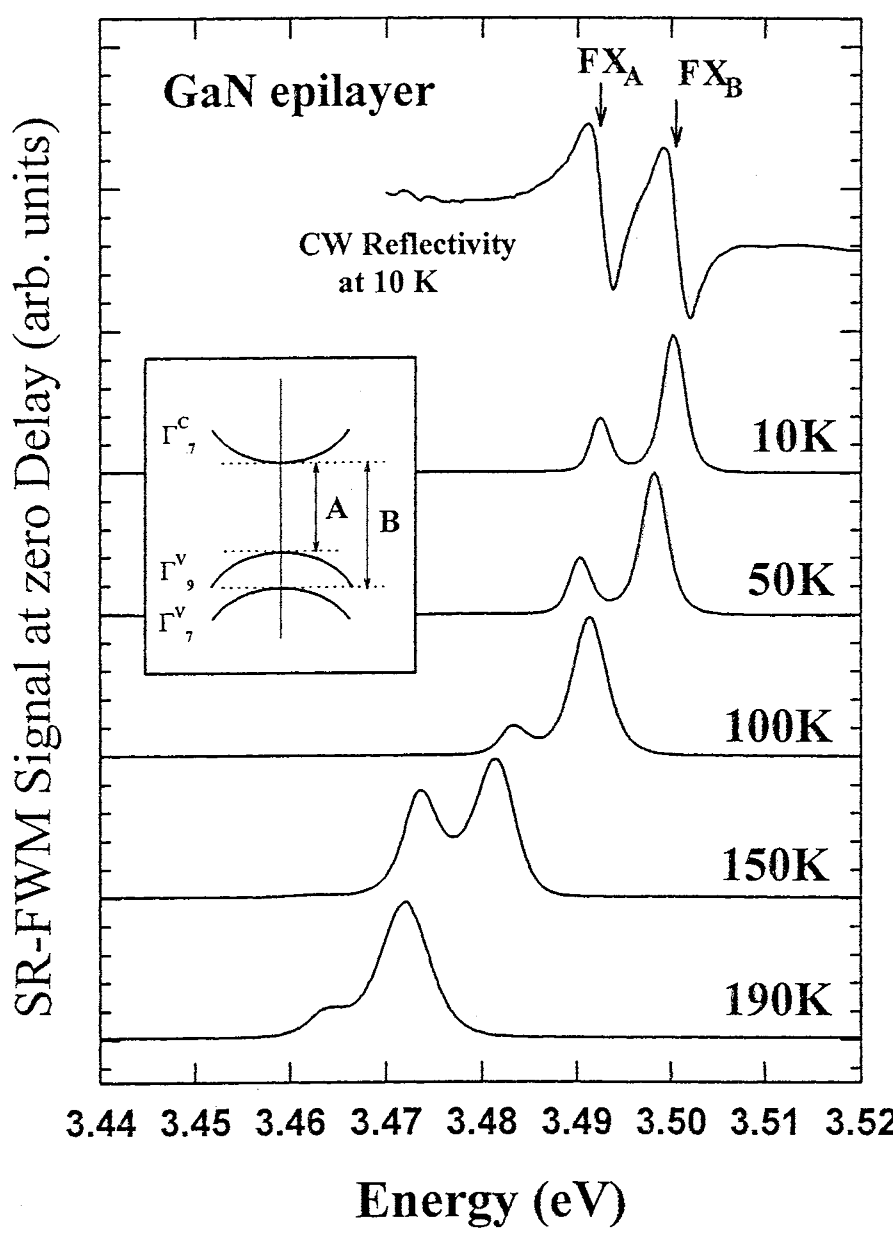

Figure 40. Spectrally-resolved four-wave-mixing (SR-FWM) from the A and B excitonic resonances near zero delay at 10, 70, 140, and 190 K. The inset shows the excitonic band structure with the A and B transitions labeled.

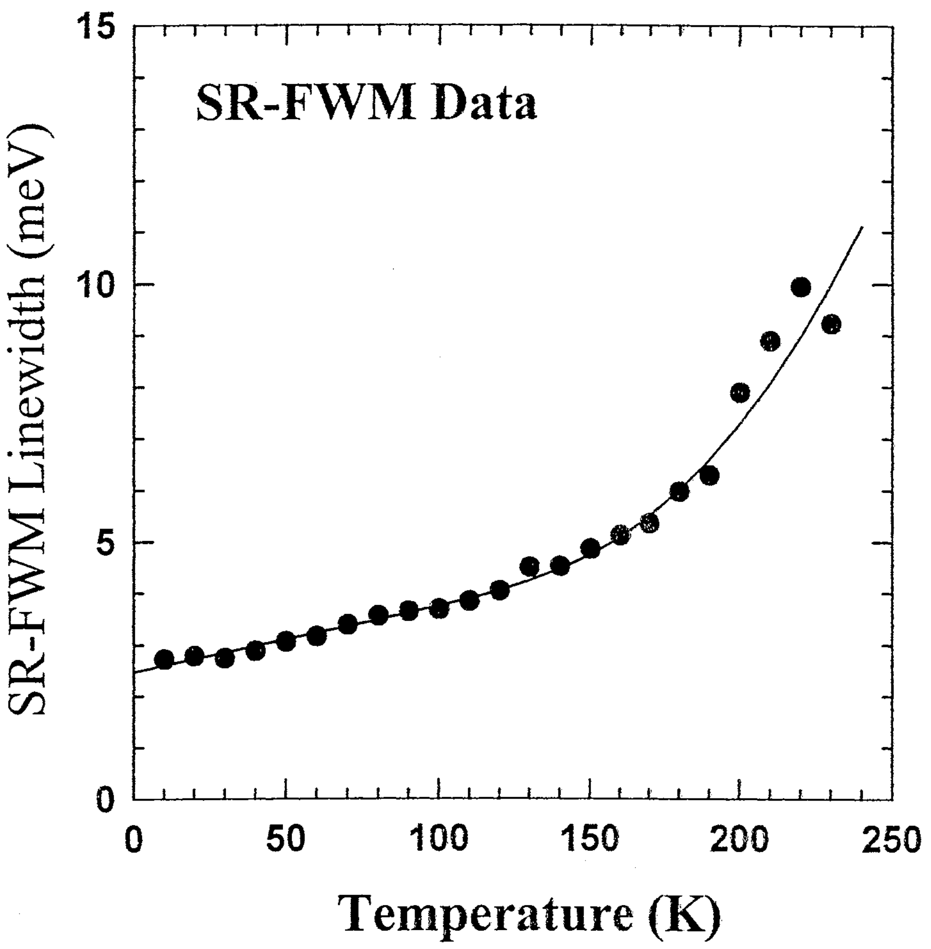

Figure 41. Spectrally-resolved four-wave-mixing (SR-FWM) linewidth of the B exciton plotted as a function of temperature. The solid line is a least-squares fit to Eq.(59).

the temperature dependent data presented in Fig. 40. The solid curve is a fit to the phonon broadening equation (Eq. 59) where the fit parameters are given by Γ_0 = 2.5 meV, γ_{ph} = 13 μeV/K, and Γ_{LO} = 470 meV. Since the time-resolved data of Fig. 38 becomes time-resolution limited above 210 K, the SR-FWM data give more reliable values of the exciton-phonon coupling constants, especially Γ_{LO}. Note, however, that the values from both SR-FWM and TI-FWM are quite close. Linear absorption measurements presented in chapter 3 give values of Γ_0 = 10 meV, γ_{ph} = 15 μeV/K, and Γ_{LO} = 375 meV which are also very close. The values obtained from a fit to absorption data contain the most error since a large background of free carrier absorption must be subtracted. For SR-FWM measurements, on the other hand, it is know that the excitonic contribution is several orders of magnitude larger than the free carrier contribution. Therefore, the values obtained from SR-FWM measurements are the most reliable and indicate that the exciton-phonon coupling constants in GaN are quite large.

The relatively fast scattering at low temperature is most likely due to scatterings with macroscopic variations in sample quality or impurity scattering. On the other hand, since the total linewidth is roughly the sum of the homogeneous and the inhomogeneous broadenings [114], we can put the upper limit to the inhomogeneous broadening in our sample caused by variations in sample quality. For both the A and the B excitons, it is less than 1.5 meV, and most likely in the range of a few tenths of an meV. Therefore, with further reduction of the defect density, achieving GaN exciton linewidths of less than 1 meV should be possible.

Quantum Beating

We now discuss the quantum beating between the A and the B excitons observed by TI and SR-FWM. As shown in Fig. 42, when we tune the laser roughly in the middle of the A and B exciton, well defined beating, whose period coincides with $(E_B - E_A)/h$, is observed (E_A , E_B = energy of the A and the B excitons observed in SR-FWM, respectively). However, the beating observed in TI-FWM in itself does not imply the existence of charge oscillation between energy levels in

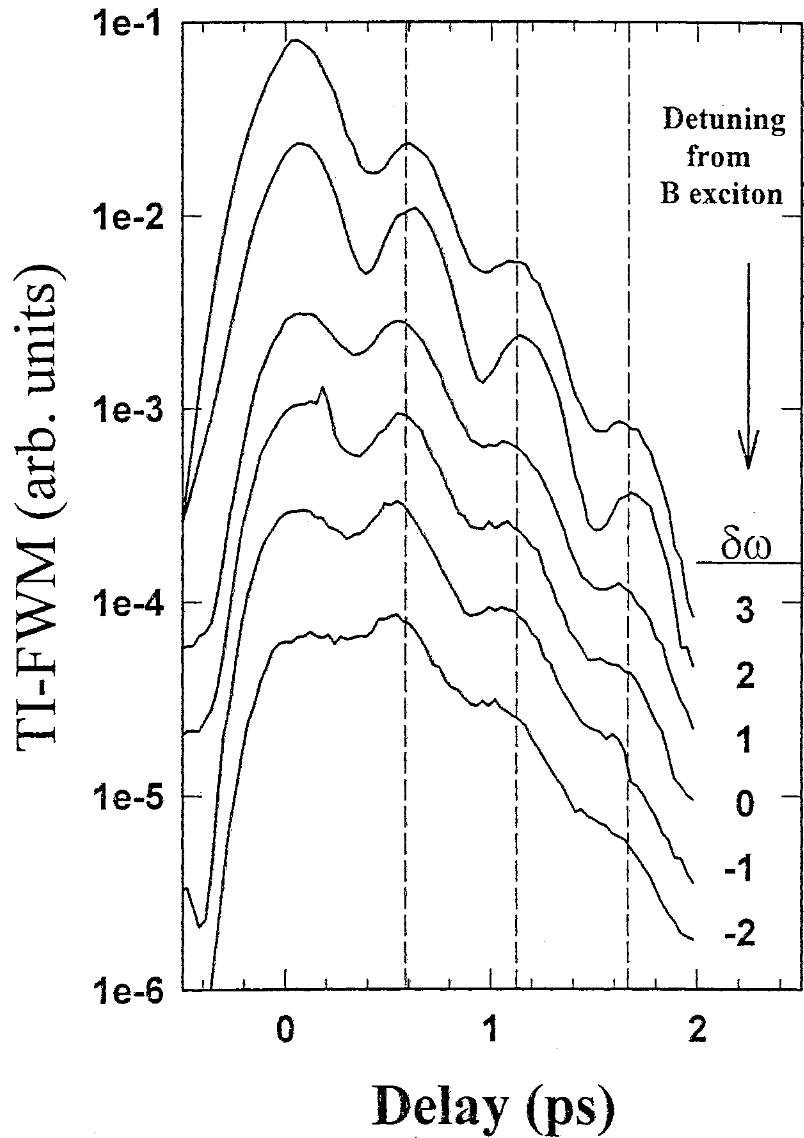

Figure 42. Time-integrated four-wave-mixing (Ti-FWM) data at 10 K for different detunings $\delta\omega = \hbar\ (\omega_d - \omega_2)$ around the B exciton where ω_d is the detection frequency. Different detunings are offset for clarity.

a coherent superposition of A and B excitons. The beating may be due to the, so called, polarization interference where the polarizations of two independent two-level systems interfere in the detector. There are two ways to experimentally determine whether the beats are due to true quantum beats or to polarization interference. One way is to perform time-resolved (TR) FWM measurements in order to determine the evolution of the FWM in time. By analyzing the TR-FWM data it is possible to distinguish between polarization interference and quantum beats [115]. A second way, which is far simpler, is to use spectrally resolved FWM at several positions across the linewidth [111]. This method, which is described in greater detail below, is used in this study to show that the beats are due to true quantum beats.

In Fig. 42, TI-FWM is plotted as a function of delay for several different energy positions across the B exciton resonance. In order to perform this measurement, a spectrometer was placed in front of the photomultiplier tube to select a small energy bin of width about 1 meV. The delay is then scanned so that we can measure FWM from only that 1 meV energy bin. The spectrometer can then be moved to a new position and the optical delay scanned at that new spectrometer position. This is how the data in Fig. 42 was taken. According to a simple theory [111], if the phase of the quantum beats changes as the detection position moves through the center of one of the resonances, then the beating is due to polarization interference. However, if there is no phase change, then the beats are due to true quantum beats. The phases are completely in synch at all the detection energies, which indicates that the beating we observe in TI-FWM is indeed due to exchange of population between levels of a coherent superposition of the A and B excitonic resonances.

Having established the quantum nature of the beating observed in TI-FWM, we now turn our attention to the polarization dependence of the quantum beat. The beating behavior has been studied as a function of as a function of input laser polarization and a phase change of π has been observed when changing from a collinear polarization geometry to a cross-linear geometry as shown in Fig. 43. This type of phase change has been observed previously for beating between the HH and the LH

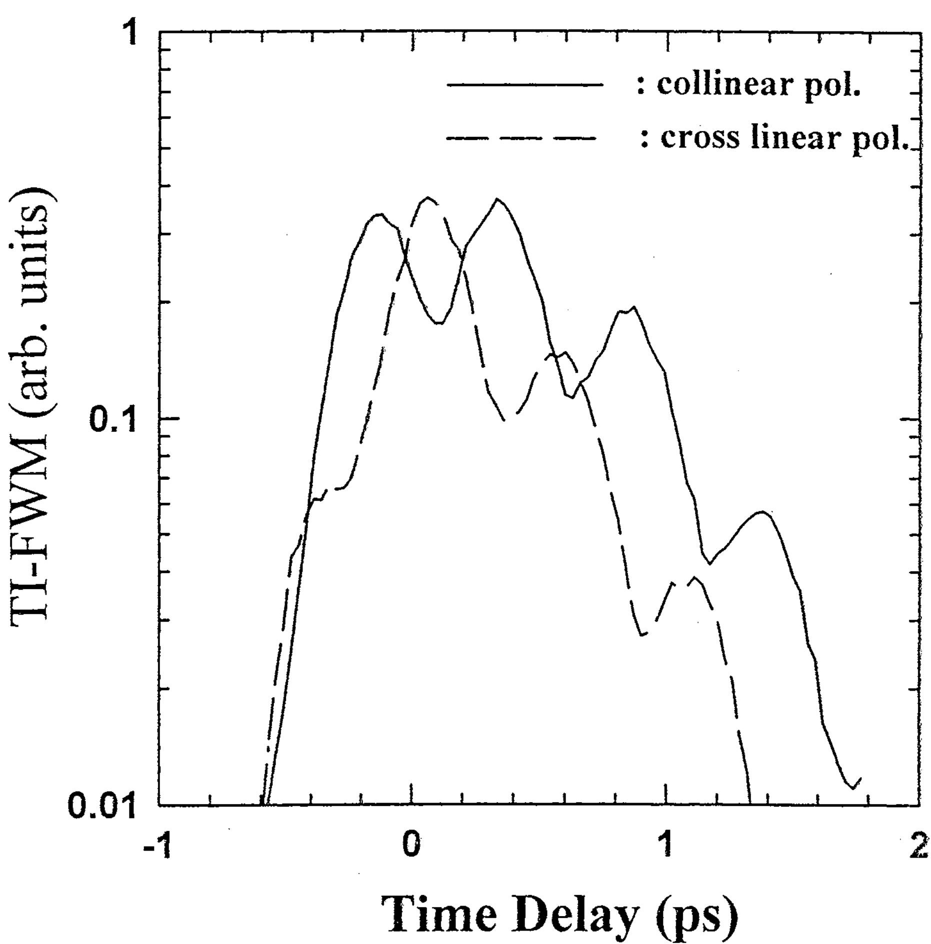

Figure 43. Time-integrated four-wave-mixing (TI-FWM) signal at 10 K for collinear (solid line) and cross-linear (dashed line) polarization geometries.

excitons in a GaAs quantum well sample [112]. The phase change can be understood based on a calculation performed in Ref. [112]. The calculation begins with the optical Bloch equations and uses third-order perturbation theory to calculate the polarization $P^{(3)}(2\mathbf{k}_2 - \mathbf{k}_1)$ which is diffracted into the phase-matched direction $2\mathbf{k}_2 - \mathbf{k}_1$. In this paper, we present the results of a calculation based on Ref. [112], but applied to wurtzite GaN. We present only an outline of the calculation and the reader is directed to Refs. [112] and [14] for further details. The appropriate eigenvectors for GaN valence and conduction bands were determined by diagonalizing the $\mathbf{k} \cdot \mathbf{p}$ Hamiltonian as done previously by S.L. Chuang et al. [14]. We find that the only change to Eq.(10) of Ref. [112] is that the 1/3 and 1/9 prefactors are replaced by $1/(1+\eta^2)$ and $1/(1+\eta^2)^2$, where $\eta = \left(2/\sqrt{3}\right)(\Delta_{so}/E_2)$, Δ_{so} is the spin-orbit split-off energy, and E_2 is the B valence band energy. Using the calculation parameters from Ref. [14], η = -0.5 for GaN while η = - 1.4 for GaAs. Thus we can reproduce the results of Ref. [112] as well as extend the calculation to GaN. Fig. 44 shows the calculated FWM signal in the ultrashort-pulse limit for collinear and cross-linear polarization geometries. Thus, a phase shift of π is also predicted for GaN.

Conclusion

In conclusion, femtosecond coherent spectroscopy has been performed on excitons in a high quality GaN epilayer grown on a sapphire substrate. By the combined analysis of the TI-FWM and SR-FWM, we found that our excitons are nearly homogeneously broadened even at low temperature. We have deduced the exciton-phonon interaction rates, and observed a beating in TI-FWM which we identified as quantum beating between the A and the B excitons. Finally, we observed a clear phase shift of π between the quantum beats in the collinear and the cross-linear polarization geometries. We have performed a calculation based on a third order perturbational solution of the optical Bloch equations in the ultrashort-pulse limit which predicts this phase shift for beating in wurtzite GaN.

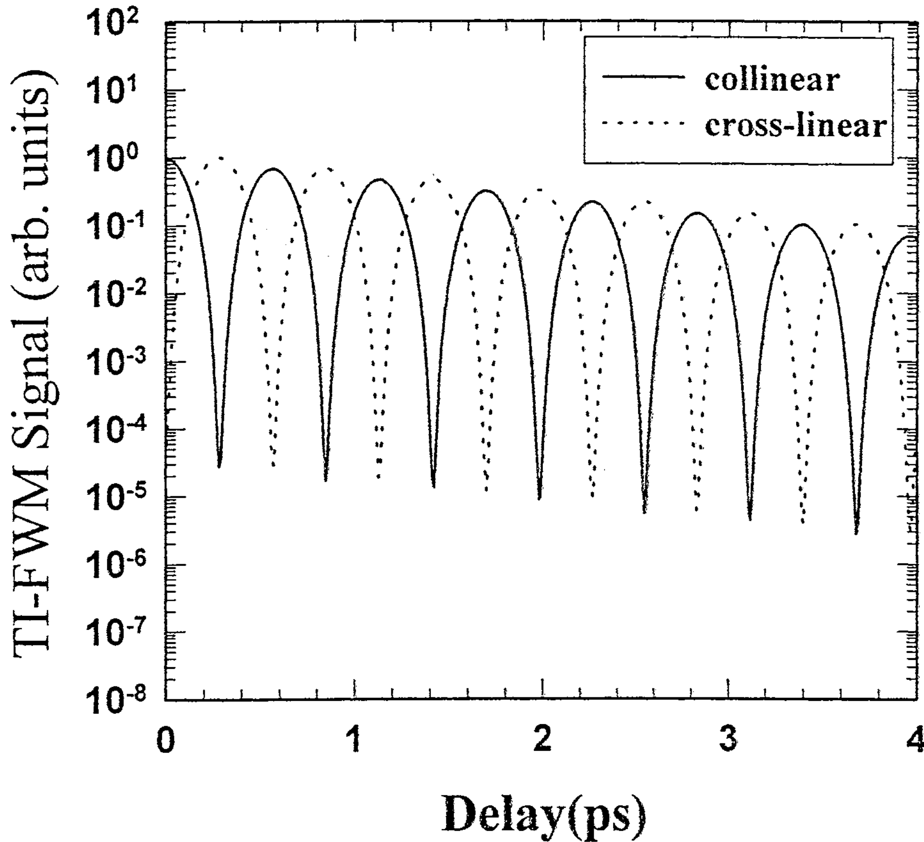

Figure 44. Calculated four-wave-mixing signal in the ultrashort pulse limit for collinear (solid line) and cross-linear (dashed line) polarization geometries.

CHAPTER VII

FEMTOSECOND OPTICAL PUMPING AND PUMP-PROBE MEASUREMENTS IN GaN EPILAYERS

Introduction

Optical pumping measurements provide a non-invasive method of studying the stimulated emission (SE) and lasing properties of a semiconductor sample. Electrical contacts do not need to be attached to the sample so that problems associated with non-Ohmic contacts are avoided. This measurement is usually performed prior to actual device fabrication in order to determine if a given material is a good candidate for a laser diode. SE measurements give information on the mechanism which causes gain in the semiconductor and can be used to measure the gain. Another way to measure gain is through the use of pump-probe absorption measurements. In pump-probe absorption, the changes in the absorption spectrum due to a strong pump pulse are monitored by using a weak probe pulse. For very strong pumping of high quality samples, it is possible to observe negative absorption or gain. Pump-probe absorption using ultrafast laser pulses is a very good way to study ultrafast band edge carrier dynamics.

In this chapter, high energy femtosecond laser pulses from an amplified Ti:Sapphire are used to study the material properties of GaN epilayers. In the first section, stimulated emission measurements are discussed. A new SE peak has been observed which is not observed under nanosecond pumping. In the second section, femtosecond pump-probe measurements are performed on the same GaN epilayers. Although no net gain was observed, the ultrafast carrier dynamics at the band edge provide useful information relating to the lasing mechanism.

Stimulated Emission Measurements

Fig. 45 (a) shows side pumping stimulated emission data for pumping densities near the SE threshold. The data look very similar to that observed from nanosecond pumping measurements. The broad peak on the high energy side is due to scattered pump light from the broad femtosecond pulses as well as GaN luminescence. Fig. 45 (b) shows the emission intensity as a function of the pump fluence. The threshold fluence for SE is 50 $\mu J/cm^2$. Fig. 46 (a) shows the emission at medium powers and 46 (b) shows the emission at high pump powers. As the pump intensity is increased, the SE peak begins to broaden and then shift. At about 10 times the SE threshold, a second peak appears at lower energy which shifts out rapidly with increasing pump power.

The origin of this peak is still not known with certainty. This peak is only observed at 10 K and not at room temperature. The two peaks merge with increasing temperature at about 150 K. Thus, it is not known if there is only one peak at room temperature or if there are two peaks which are broadened together. The gain which produces stimulated emission at low power is most likely to be exciton-exciton related. This is because the large exciton binding energy of 21 meV allows excitons to exist to higher densities before the Mott transition occurs. Once the density of excitons is large enough for the excitons to fill most of the space in the semiconductor, the system is thought to undergo a transition to an electron-hole plasma. We expect that, in the density range where there is only one peak, the carrier density is high enough to already be in a plasma state. Thus, the second peak may be due to an excited state of the plasma or to emission from another band. More experimental and theoretical work needs to be done in order to determine the mechanism which causes gain for the second peak.

Pump-Probe Measurements

Although the optical properties of GaN have been vigorously studied for the last decade, very little information is known about how the band edge absorption changes

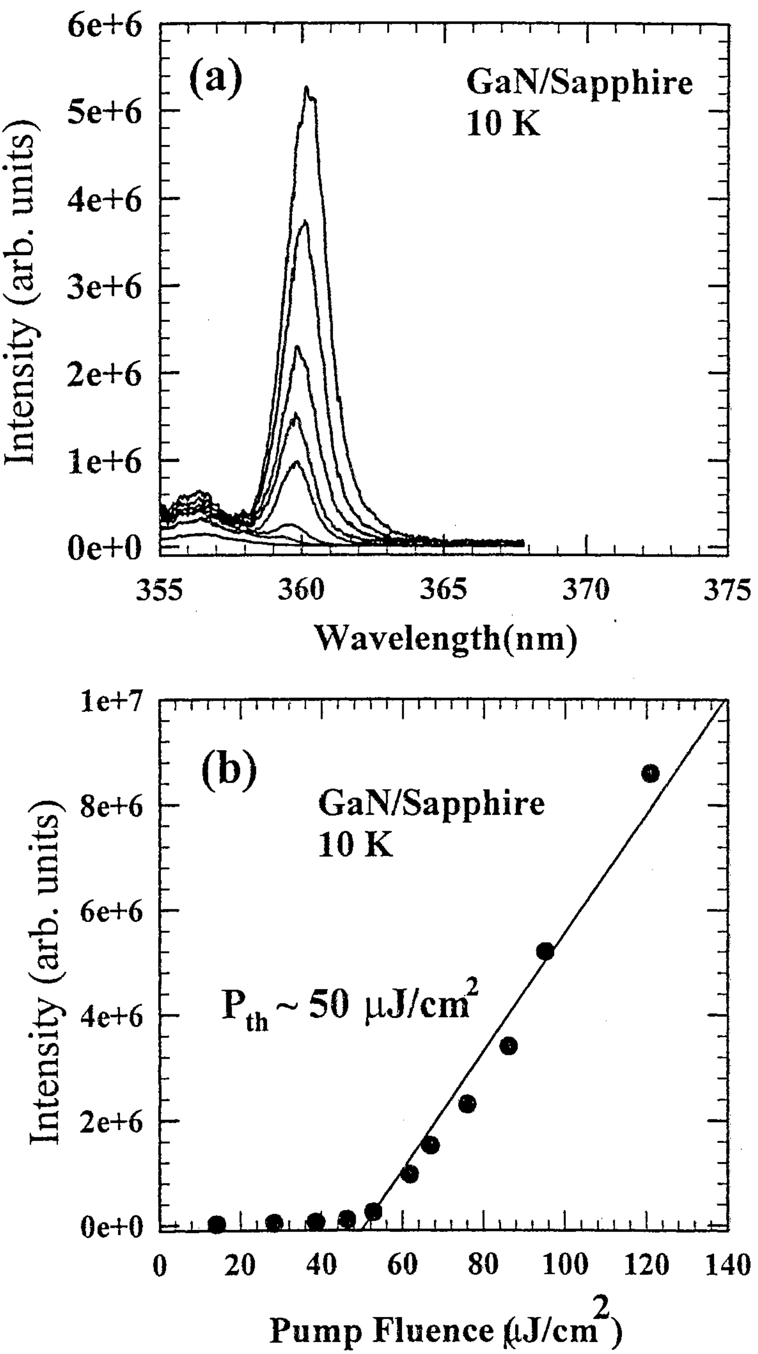

Figure 45. (a) Stimulated emission spectra at several pumping fluences at 10 K for an epilayer of GaN/sapphire (b) Emission intensity as a function of pump fluence for the same data. The threshold fluence is 50 $\mu J/cm^2$.

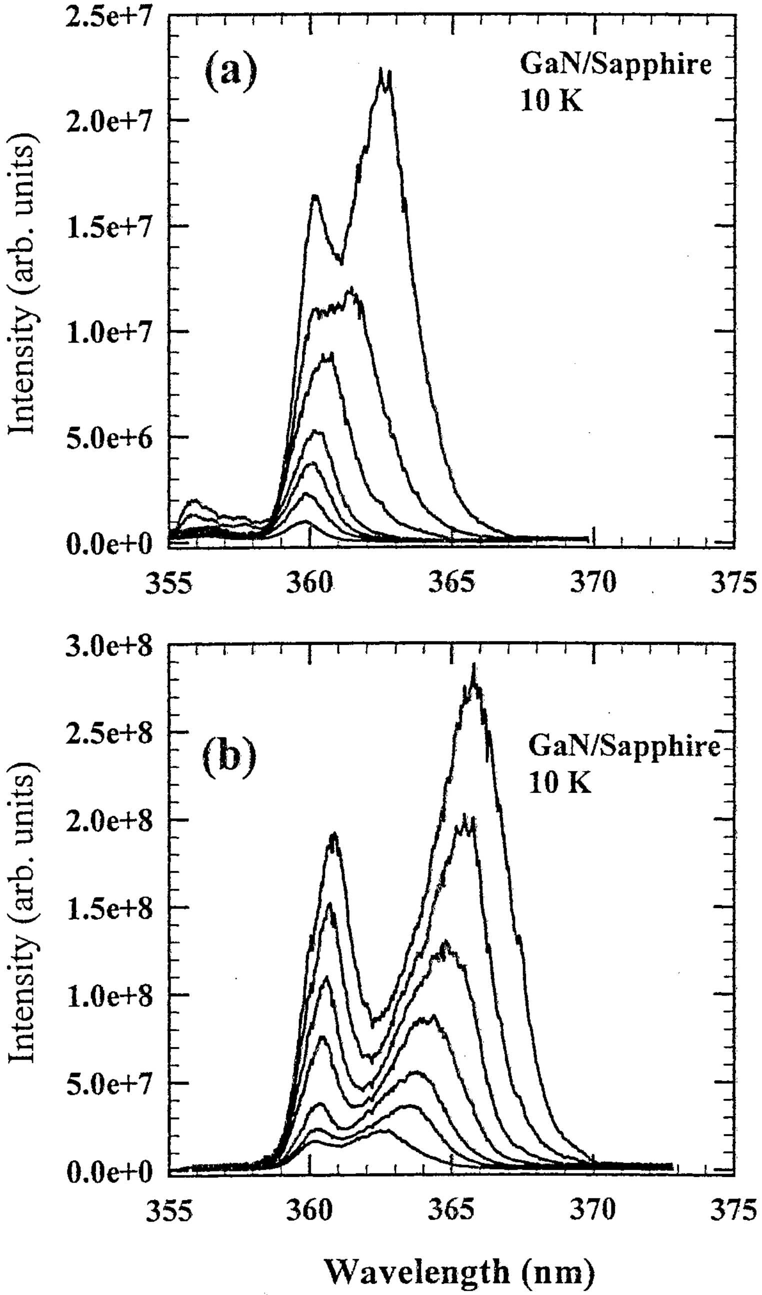

Figure 46. Femtoseond stimulated emision at (a) medium and (b) high powers. A second stimulated emission peak appears at about 10 times the stimulated emission threshold.

with increasing carrier density. Recently, pump-probe measurements were performed on epilayers of GaN under nanosecond excitation [116]. The power density required for exciton saturation was measured for both reflection and transmission experiments, and a large below band gap induced absorption was observed. However, absorption changes under high excitation conditions have not been measured on an ultrafast time scale. In this section, the results of femtosecond pump-probe experiments will be presented which show the time-evolution of exciton saturation and recovery.

Previously, high density pump-probe experiments were performed under both resonant and non-resonant pumping conditions for a wide variety of material systems including bulk GaAs [117–120], GaAs QWs [121–123], and CdZnTe/ZnTe QWs [77]. For pumping well above the gap in GaAs based materials, band gap renormalization occurs instantaneously. The carriers relax to the band edge after several picoseconds and the absorption is saturated due to screening and band-filling effects. Gain from an electron-hole plasma can be observed just below the unpumped gap several picoseconds after excitation [120,122]. The band edge absorption then recovers over hundreds of picoseconds with a time that is determined by the radiative and non-radiative lifetimes of the excited carriers.

Under near-resonant pumping conditions, we observe induced absorption at zero delay below the unpumped gap due to band gap renormalization. The above gap absorption saturates first, but recovers quickly as carriers relax down to the band edge. Strong excitonic saturation caused by plasma screening from free carriers is then observed near zero delay. The saturation of the excitonic resonance is followed by a large below-gap induced absorption caused by a transient electron-hole plasma. Fast recombination channels rapidly capture carriers so that the induced absorption quickly vanishes. This results in no net gain being observed in our samples. After 1 ps, the absorption recovers to an intermediate value which is associated with excitonic phase space filling. The absorption then recovers slowly with a characteristic time of $\approx$20 ps.

The GaN samples used in this study were grown by metalorganic chemical vapor deposition on sapphire substrates. Low power absorption data from these

samples has already been published [124]. The 10 K data for the 0.38 μm thick epilayer are shown for reference in Fig. 47. For this study, carriers were excited using pulses from an amplified Ti:Sapphire laser. The pulses were amplified using a three-stage dye amplifier which was pumped by the second harmonic of a 10 Hz, nanosecond Nd:YAG laser. This system produced 350 fs pulses at 702 nm with an energy of 300 μJ. One half of the second harmonic (351 nm) was used to excite carriers above the band gap of GaN while the other half was focused onto a 3 mm thick piece of quartz to create a broad-band continuum probe source (see Fig. 48). The probe beam was focused to a 150 μm diameter at the sample and the transmitted light was collected and focused into a spectrometer with an attached CCD detector. The pump beam was focused onto the sample with a larger spot diameter of 250 μm diameter in order to reduce effects associated with the transverse beam profiles. The optical delay between pump and probe could be controlled accurately using a computerized stepper motor delay stage.

Fig. 47 shows the band edge absorption spectra at 10 K for several pump fluences together with the CW absorption data for the 0.38 μm sample. Well-resolved A and B resonances could be observed under low pumping conditions, however, for the data shown here, the A and B resonances are merged due to the broadening of the resonances with pump power and the difficulty of obtaining clean, high resolution data at 10 Hz. These spectra were taken with a delay of 1 ps between pump and probe. At this time delay, the initial transient effects (discussed below) are gone and the carriers have relaxed down to the band edge. The excitonic resonances decrease with increasing pump fluence and the onset of saturation at 20 μJ/cm^2 is shown in the inset of Fig. 47. At the highest pump density, the absorption above the excitonic resonances also begins to saturate. For a sample thickness of 0.38 μm and an absorption coefficient of 1.2 x 10^5 cm^{-1} at the exciton, our sample is optically thick. Therefore, the excited carrier density is not uniform throughout the 0.38 μm sample thickness. The large lattice mismatch between the sapphire substrate and the GaN epilayer makes it very difficult to grow high quality thin samples and we found that thinner samples exhibited much lower optical quality as judged by

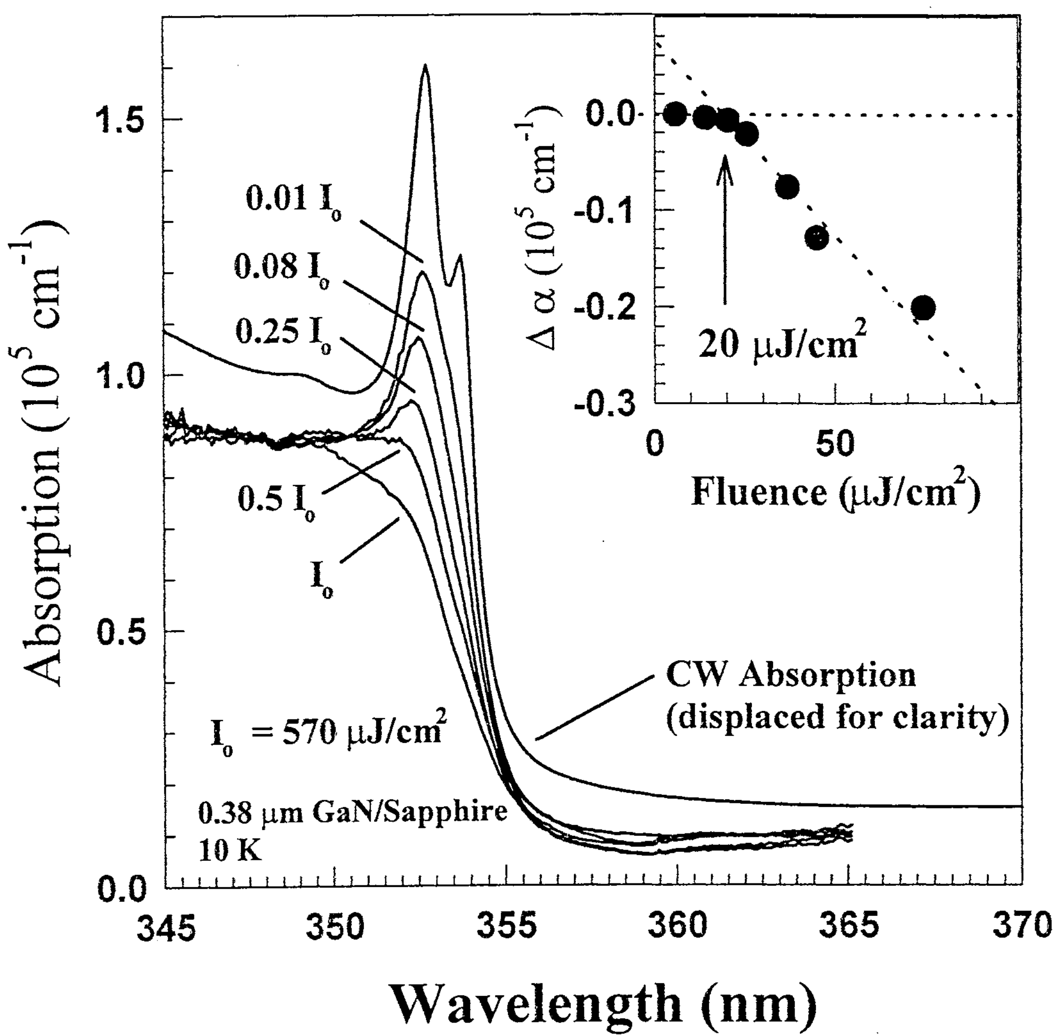

Figure 47. Absorption spectra at 10 K as a function of pump fluence shown together with low power CW absorption data from the same sample. The CW absorption spectra has been displaced for clarity. The inset shows the onset of saturation at 20 μJ/cm^2.

photoluminescence and absorption measurements. Although the carrier distribution is not constant throughout the sample thickness, the density of induced carriers can still be estimated. At the onset of saturation, the average density of carriers in the first 0.1 μm is estimated to be about 1 x 10^{18} cm^{-3} while the maximum density of this study is about 1 x 10^{20} cm^{-3}.

Fig. 48 shows the band edge absorption as a function of time delay for a pump fluence of 160 μJ/cm^2. The excitonic resonance saturates in 1 ps and recovers slowly over the next 100 ps. The inset shows the change in the absorption coefficient at the peak of the excitonic resonance as a function of time delay. The resonances recover with characteristic times of 17 ps and 23 ps for pump fluences of 160 μJ/cm^2 and 730 μJ/cm^2, respectively. The longer recovery time at higher pump densities can be explained by considering that the injected carrier densities are not uniform throughout the sample thickness. For epilayers of GaAs, it was found that thin samples exhibited a very fast absorption recovery ($<$ 50 ps) while the recovery in thicker samples occurred on a much slower time scale ($\approx$1 ns) [119]. The thin samples recover faster due to fast non-radiative surface recombination while carriers in thicker samples must decay with the bulk radiative lifetime, which is on the order of nanoseconds. For this study, it is expected that under low pumping conditions, carriers are mainly created in a thin layer near the surface and can recombine via fast surface recombination. However, under very strong pumping conditions, the absorption is saturated further into the sample thickness so that higher carrier densities are created deeper into the epilayer. Carriers located in the interior region of the sample must recombine via slower, bulk-like radiative recombination, and thus, a slower recovery is observed at higher pump fluences.

Fig. 49 shows the absorption spectrum as a function of delay in a very small region near zero delay for a pump fluence of 750 μJ/cm^2. The absorption spectrum at zero delay shows a dip in the absorption near 351 nm due to a hole-burning effect of the pump pulse. The carriers created at 351 nm quickly thermalize and relax towards the band edge causing the hole at 351 nm to disappear. After 375 fs, transient induced transparency is observed below the band gap at $\approx$356 nm. The ultrafast

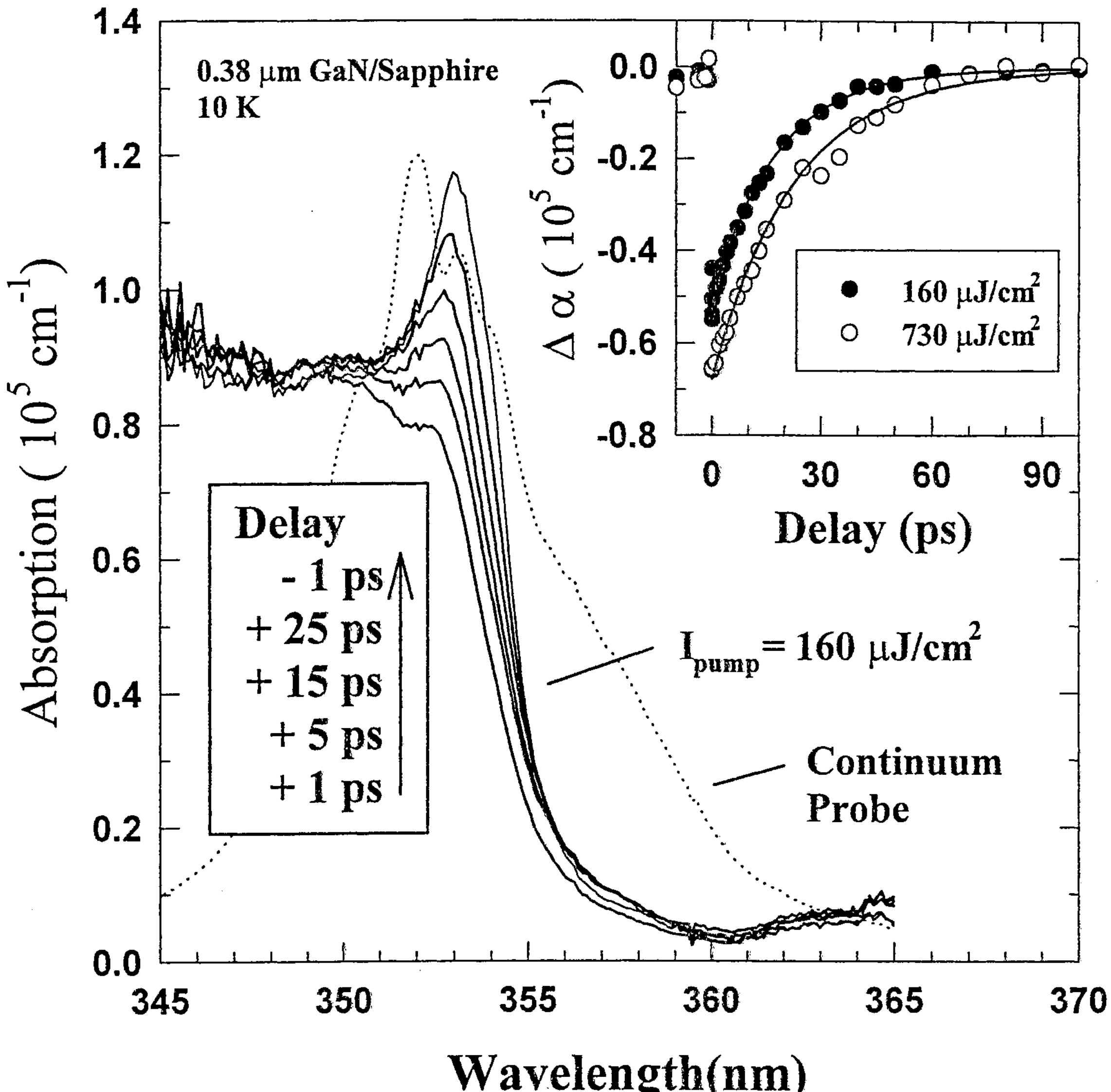

Figure 48. Absorption spectra as a function of delay between the laser pump and white-light continuum probe (dashed line) for a pump fluence of 160 μJ/cm^2. The inset shows the absorption saturation at the peak of the excitonic resonance at 160 μJ/cm^2 (full circles) and 730 μJ/cm^2 (open circles).

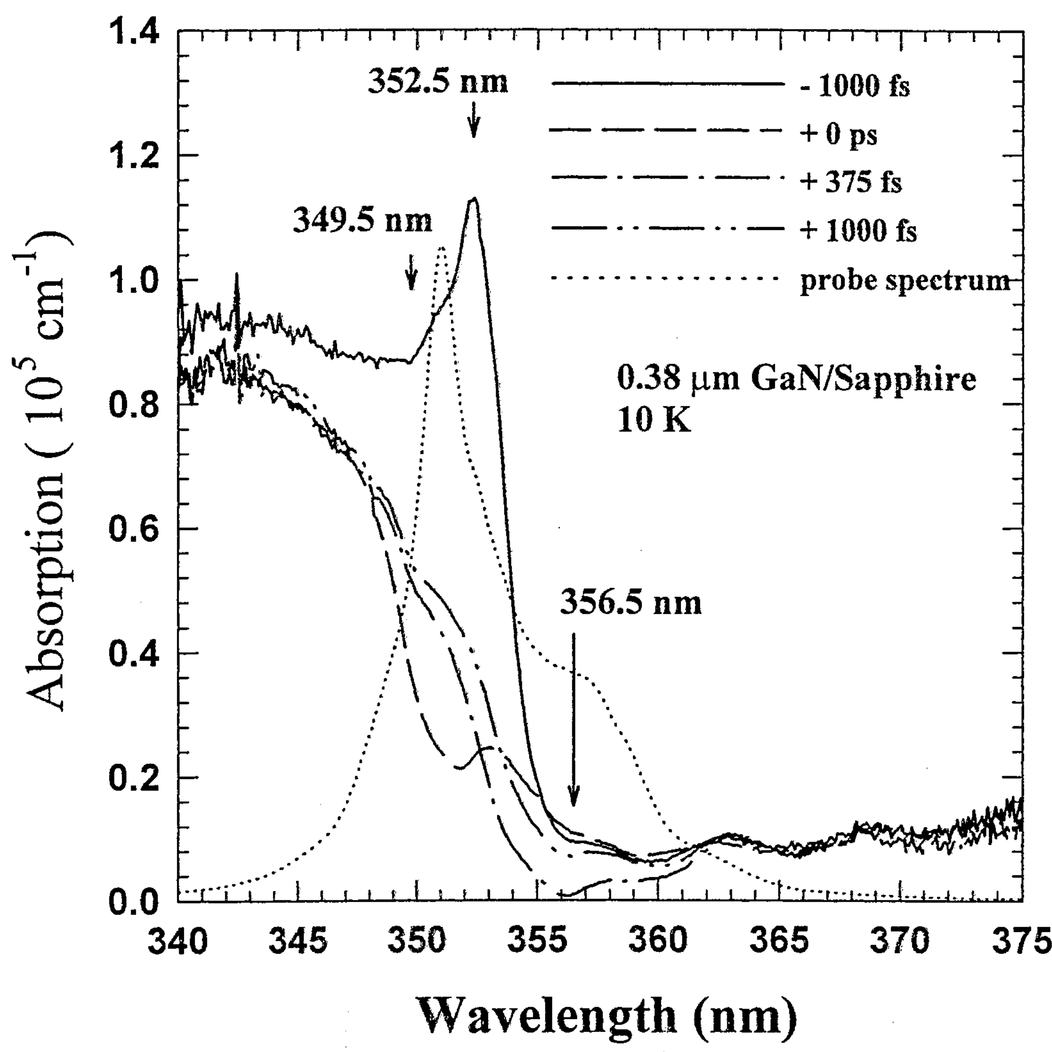

Figure 49. Absorption spectra as a function of delay for a pump fluence of 750 $\mu J/cm^2$ showing the ultrafast near-zero-delay dynamics. Note the induced transparency at 356.5 nm.

dynamics near zero delay are much more clear in Fig. 50 where the absorption value is plotted as a function of delay. Curves are shown for detection at the excitonic resonance (352.5 nm), as well as above (349.5 nm) and below (356.5 nm) the excitonic resonance, corresponding to the arrows in Fig. 49. The above-gap absorption saturates first and then recovers quickly as carriers relax towards the band edge. The excitonic absorption saturates next and recovers after 1 ps to an intermediate value which is associated with excitonic phase-space filling. The below-gap data shows induced absorption during the first few hundred femtoseconds due to band gap renormalization. The induced absorption changes to a strong induced transparency which shows maximum transparency at 375 fs. This strong induced absorption recovers faster than the time resolution of the experiment to the intermediate level associated with band filling.

The most striking feature observed in this work is the strong transient induced transparency observed below the unpumped gap. This induced transparency is most likely caused by a transient electron-hole plasma. Such non-equilibrium electron-hole plasmas have been observed in CdS and CdTe samples under strong optical pumping conditions [125]. The induced transparency occurs just after the excitonic resonance is most strongly screened. Thus, a transient electron-hole plasma is providing some gain in a thin layer near the surface while it screens the excitonic resonance. The plasma state disappears quickly due either to fast non-radiative recombination at the surface or to stimulated emission in the plane of the sample, acting to quickly remove excited carriers.

There are several reasons to believe that we have created a transient electron-hole plasma in our samples. Pump-probe measurements in GaAs epilayers have demonstrated that gain can occur as fast as 280 fs after excitation which is consistent with our observation of strong induced transparency after 375 fs. The induced transparency is most likely due to gain in a very thin layer at the surface of the sample combined with absorption from band tailing states further into the sample. For the relatively thick sample used in this study, the highest carrier density occurs in a thin layer near the surface. No attempt was made to correct for reflection losses

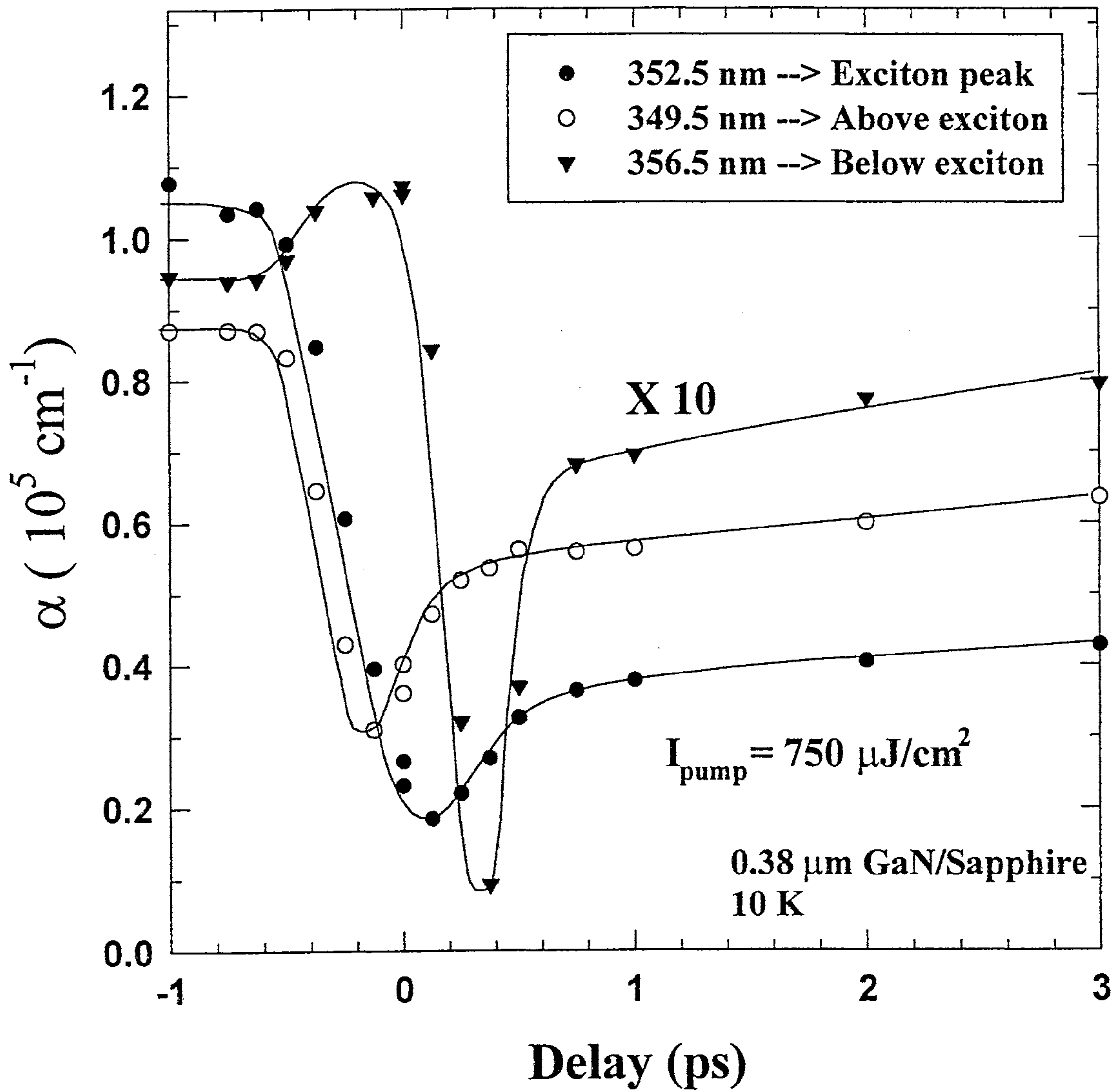

Figure 50. Absorption as a function of delay for the three wavelengths denoted with arrows in Fig. 49. Note the induced absorption below the band-gap at zero delay followed by induced transparency which reaches a maximum transparency at 400 fs. The solid lines are guides for the eye.

from the GaN surface. Although no net gain was observed, if reflection losses were accounted for and it was assumed that the change in absorption came from the first 50 nm of the epilayer, then one could estimate a gain as high as 10^4 cm^{-1}. Such a high gain must be due to an electron-hole plasma. The gain disappears quickly due to fast non-radiative recombination or stimulated emission in the plane of the sample. It is known from time-resolved photoluminescence measurements that the luminescence decay time of the exciton is dominated by non-radiative recombination channels [126]. Therefore, it is reasonable to expect that for samples with a lower defect density, the plasma state will persist longer and gain will be observed in transmission for GaN as it has been for GaAs-based samples.

Conclusions

In conclusion, we have performed transient absorption measurements of a 0.38 μm thick epilayer of GaN under conditions of strong optical pumping. Exciton saturation is shown to occur within 1 ps and recovery with a characteristic time constant of $\approx$20 ps. This recovery was shown to be slower at higher pump fluences since high carrier densities are created deeper inside the sample where slower bulk-like recombination occurs. Induced absorption was also observed below the band gap due to band gap renormalization. This induced absorption quickly changes to induced transparency which is due to a transient electron-hole plasma. The transient plasma state also acts to strongly screen the excitonic resonance during the first 1 ps, while the saturation at longer time delay is attributed to excitonic phase-space filling.

CHAPTER VIII

THz SPECTROSCOPY OF SEMICONDUCTOR SAMPLES

The rapid development of ultrafast picosecond and femtosecond laser systems during the last decade has paved the way for spectroscopic studies in the submillimeter rage. This wavelength region has been and remains to be a difficult region of the electromagnetic spectrum to access. However, femtosecond laser pulses can be used to generate and detect radiation in the THz range ($\approx 100\ \mu m$). THz radiation experiments can be performed using dipole antennas as both the emitter and the detector [127,128]. THz radiation can also be emitted via optical rectification of ultrafast laser pulses in semiconductors or electro-optic (EO) crystals [129–131]. The detection bandwidth of a dipole antenna is normally below 5 THz. This bandwidth limitation has led researchers to use free-space EO sampling to detect THz radiation [132–136]. The detection bandwidth using this technique has been shown to be as high as 37 THz [132]. THz spectroscopy can be a very sensitive tool for measuring material properties. Imaging systems based on both antennas [137] and EO sampling [134] have been demonstrated. While antennas are easier to use, one must perform a point by point scan in order to get a full THz image. On the other hand, while EO sampling is a more complicated technique, it should be possible to produce full images without scanning point by point. THz Spectroscopy has also been used to study the ultrafast coherent properties of GaAs quantum well samples. THz emission from quantum beats has been observed which provides direct evidence of charge transfer between energy levels of the quantum well [138–140]. In this chapter, mechanisms for the generation and detection of THz radiation using femtosecond laser pulses will be discussed.

Generation of THz Radiation

THz radiation can be generated via two main mechanisms: photoconduction and optical rectification. Photoconduction relies on femtosecond laser pulses to create current surges which generate the THz electric field. Optical rectification occur via a second order or higher process in an EO crystal where the electric field of a femtosecond pulse is rectified to a transient DC field which roughly follows the electric field envelope of the optical pulse. These mechanisms will be discussed in further detail below.

Photoconduction

A typical dipole antenna is shown in Fig. 51. An electrical bias is applied to the coplanar strips. A femtosecond pulse then creates carriers in the 5 μm gap so that an ultrafast transient surface current will flow. It is this current which generates the THz radiation. The emission bandwidth is limited by the transit time of carriers across the gap or the recombination time of the carriers. The gap width is made small to reduce the transit time and a photoconductive material with a fast carrier recovery time is chosen. Two main materials are used as the photoconductor: silicon grown on sapphire (SOS) or low temperature grown GaAs (LT-GaAs). Si is grown on sapphire and then ion implantation is used to damage the Si so that the carrier recovery time with be fast. Similarly, it has been shown that GaAs grown at low temperatures can have a very fast carrier lifetime and is thus suitable for use in antenna fabrication. Since the radiation is generated in a 5 μm region and has a wavelength of 100 μm, diffraction plays a major role in distributing the radiation over a large solid angle. A Si lens is usually used to help collimate the THz radiation. THz radiation can also be emitted from unbiased semiconductor samples [141,142] by simply focusing femtosecond laser pulses onto the sample. Although the sample has no external bias, photoexcited carriers will still accelerate in the surface field causing THz radiation.

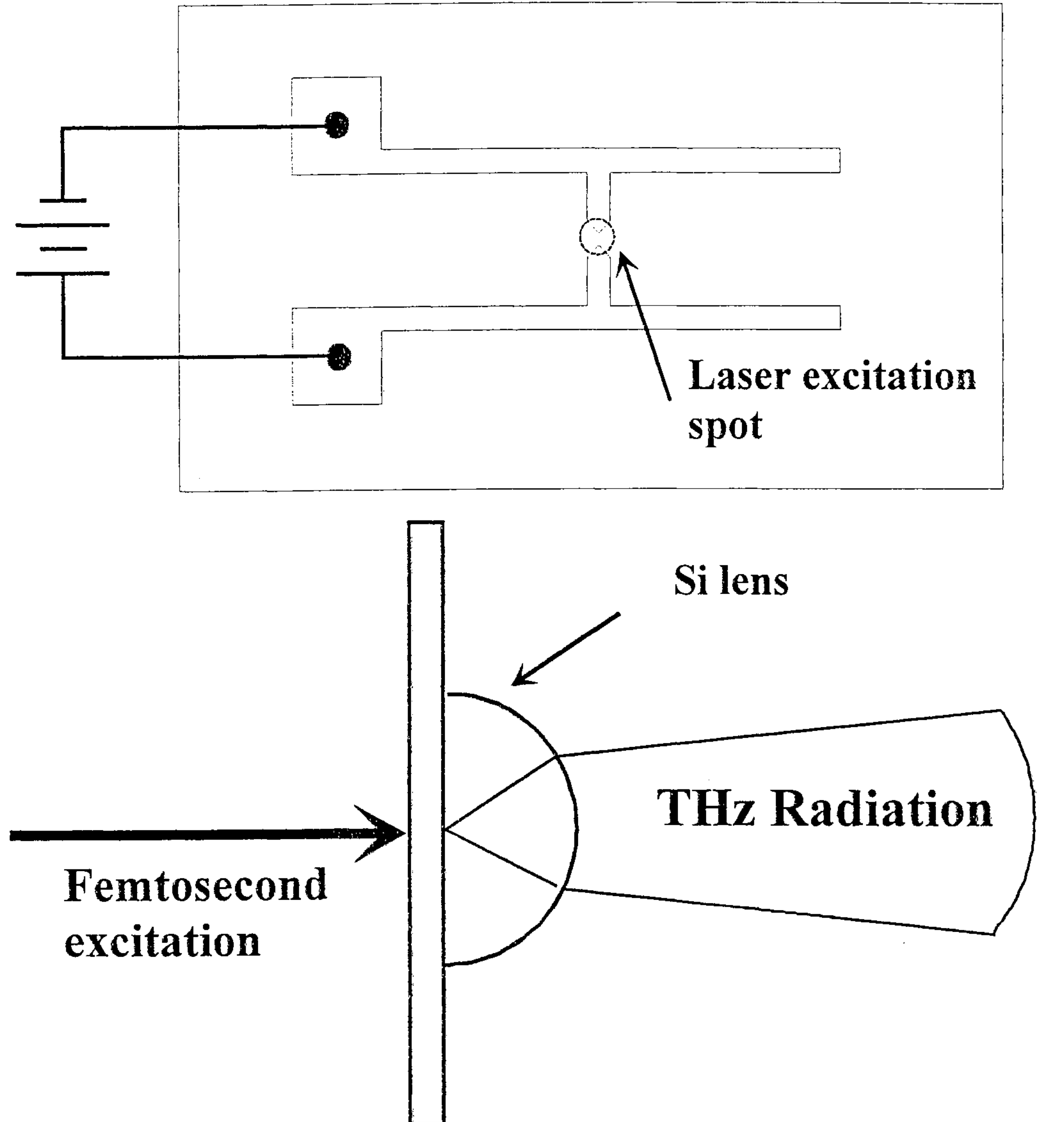

Figure 51. Schematic diagram of a photoconducting antenna. An antenna can be used for either emission or detection. When used for emission the electrical contacts are used to apply a bias voltage and the laser beam acts as the pump. When the antenna is used as a detector, the electrical contacts measure picoamp level current and the applied laser pulse acts as a gate pulse.

Optical Rectification

As mentioned above THz radiation can be generated via optical rectification [130,131]. This process can be thought of as nearly degenerate difference frequency generation. This produces a very broadband pulse of very low frequency which is in the THz region. The process is very different from the photoconduction generation of THz radiation. This process relies on having a large enough nonlinear susceptibility and large enough laser flux to directly convert the laser energy into THz radiation. This process does not require the acceleration of charged carriers. When researchers study optical rectification from semiconductors, the laser beam is sent in perpendicular to the surface and collect THz radiation out the back side in order to avoid the THz radiation generated via photoconduction [131].

Detection of THz Radiation

THz radiation can be detected via electro-optic sampling or through the use of a photoconducting dipole antenna.

Electro-Optic Sampling

The experimental set up for electro-optic sampling is shown in Fig. 52. The figure shows an unbiased semiconductor at 45 degrees to the incident pump beam which is acting as a photoconductive emitter. THz radiation is emitted in the direction of the reflected pump beam. Off-axis parabolic mirrors are used to collimate the THz radiation and to focus it onto the ZnTe EO crystal. A 2 μm thick pellicle is used as a beam splitter to insert the weak probe pulse into the path of the THz radiation. Since the Pellicle is only 2 μm thick the shift in the path of the THz radiation is less than 1 μm and is negligible on the scale of THz optics (100 μm wavelength). The THz radiation and the probe pulse must be overlapped spatially and temporally in the ZnTe crystal. The electric field of the THz radiation causes birefringence in the ZnTe crystal which is measured by the weak probe beam.

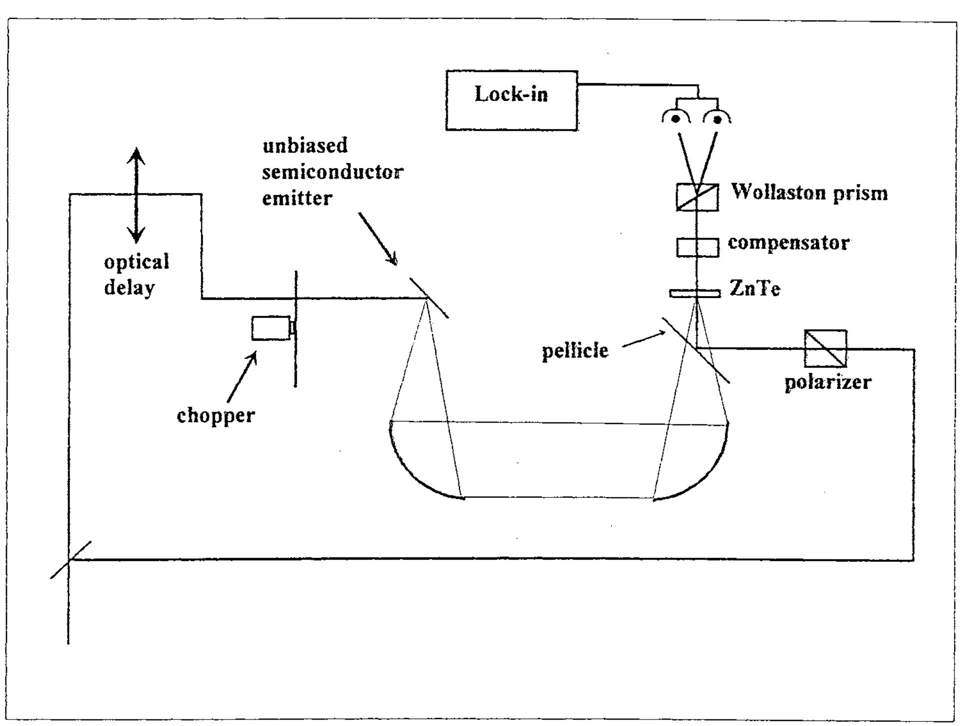

Figure 52. Experimental set up for electro-optic sampling.

The alignment of the system will now be described. A polarizer is placed in the probe beam path before the pellicle in order to make good linearly polarized light. The probe beam then bounces off the pellicle and travels through the ZnTe EO crystal. A Barak compensator is then used as a $\lambda/4$ waveplate to make circularly polarized light. An Wollaston prism is then used to analyze the probe beam into vertical and horizontal polarizations. The purpose of the $\lambda/4$ waveplate is to create a balanced detector system. If we send almost equal intensity into two identical detectors and look for a small change in the signal, then we get greater sensitivity than can be achieved with one detector alone. The balancing scheme reduces the effects of laser power fluctuations. The change in the polarization state of the probe beam will be less than one part in 10^4. Therefore, polarizers with the highest available extinction ratios must be used and efforts must be made to reduce noise caused by vibrations. One big source of noise is the pellicle itself as it is very sensitive to any sounds in the room. It is possible to remove the pellicle and replace it with high resistivity Si, but this makes the alignment much more difficult since the THz beam path changes when travelling through the Si wafer.

Antenna Detection

An antenna can be used as either an emitter or a detector. When used as a detector, a weak probe pulse is used as a gating beam to create carriers in the antenna gap. These carriers are then swept out of the region by the electric field of the THz radiation and can be measured as a current on the picoamp scale. A typical set up is shown in Fig. 53. Two different types of experiments are possible. The sample being studied may be the semiconductor emitter as in the case for THz studies charge oscillations in quantum wells. Alternatively, an emitter-detector system can generate and detect THz radiation and a material of interest can be placed in the THz beam in order to study the absorption or reflection of THz radiation.

Fig. 54 shows THz radiation generated from an unbiased InGaAs sample at 10 K. The radiation was detected using an LT-GaAs antenna. The data show three replicas of the main waveform due to reflections in the GaAs substrate of the THz

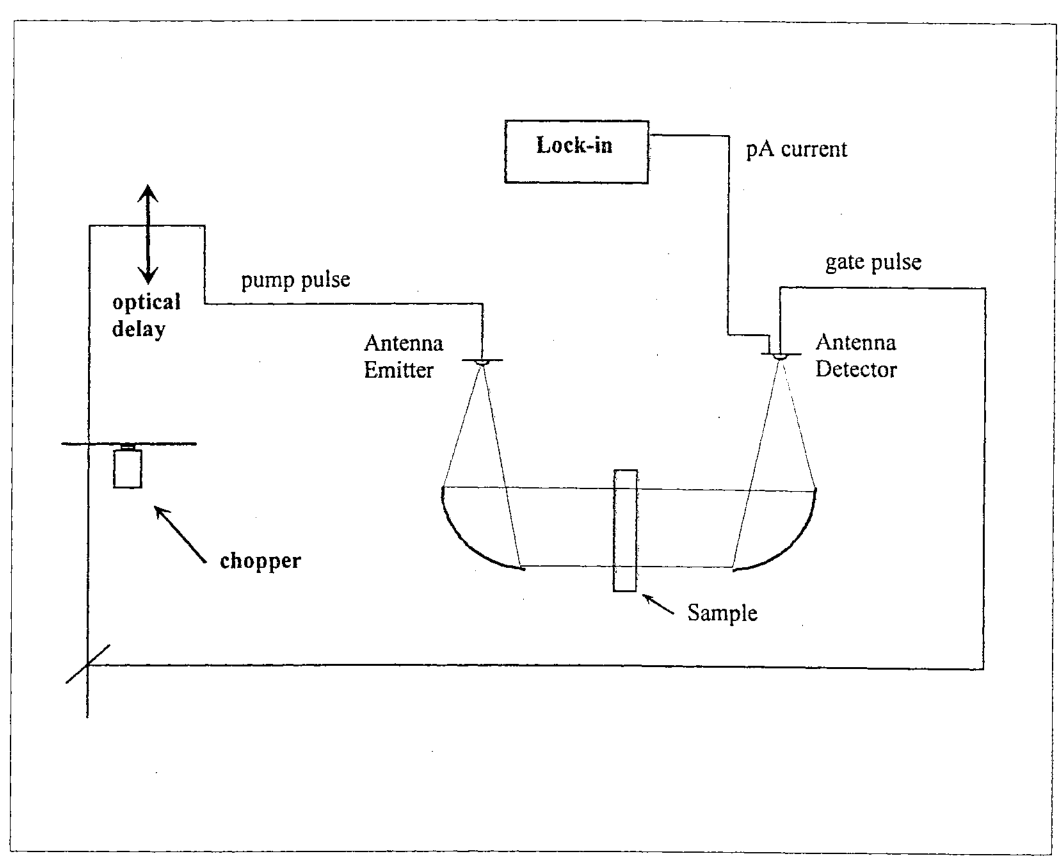

Figure 53. Experimental set up using antennas for both emission and detection.

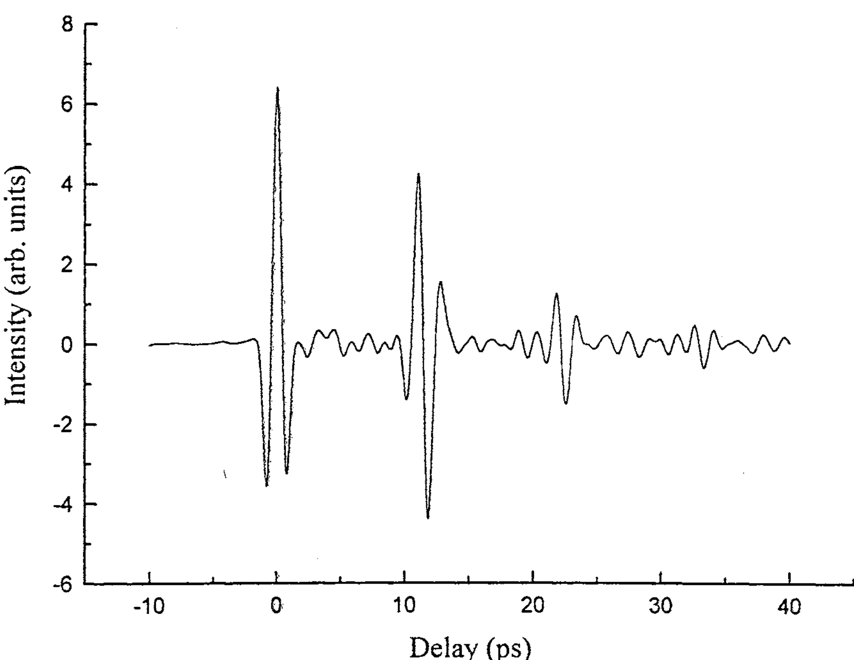

Figure 54. THz radiation emitted from an unbiased InGaAs sample using an antenna for detection. Note the three replicas of the main waveform which are due to reflections.

antenna. The small ripple observed between reflections is due to the absorption of THz radiation by water vapor in the air. The frequency spectrum of the data in Fig. 54 can be determined by performing a fast Fourier transform. The data are shown in Fig. 55. The frequency goes out to slightly larger than 1 THz. The bandwidth of the antenna is limited by the antenna geometry and the recombination time of the carriers in the LT-GaAs substrate of the antenna. This emitter-detector combination can be used to perform spectroscopy at frequencies as high as 1.2 THz.

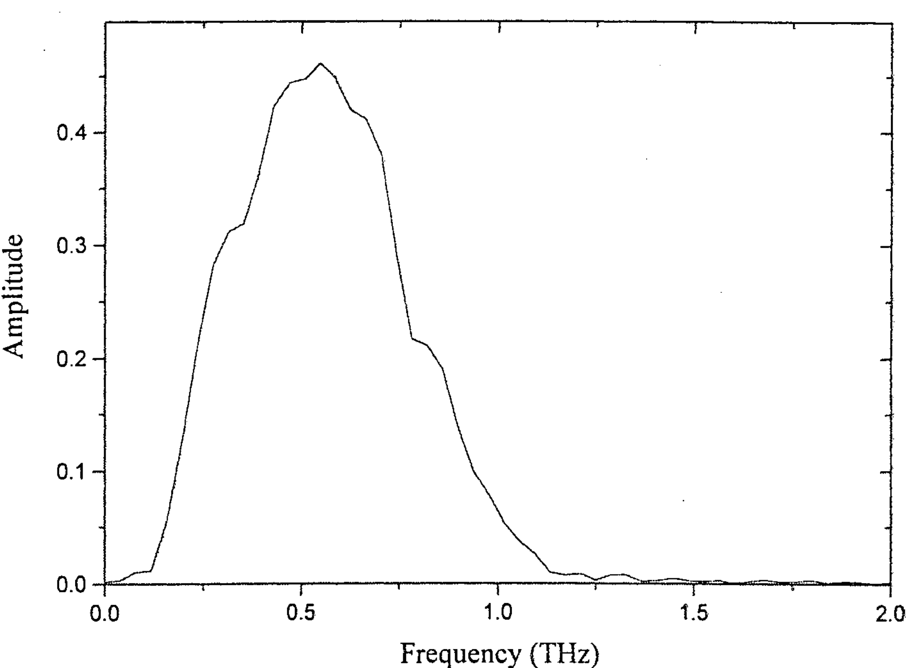

Figure 55. Frequency spectrum of the THz data from InGaAs. Note that the detection bandwidth is limited by the antenna structure and the recombination lifetime of cariers in the LT-GaAs.

CHAPTER IX

CONCLUSIONS

Wide band gap semiconductors are technologically very important materials due to their applications in blue and ultraviolet light emitting devices. Although commercially viable semiconductor lasers based on InGaN have been produced, very little is know about the ultrafast optical properties of wide band gap semiconductors. This thesis serves to extend the extensive ultrafast work which has been done in the GaAs material system to ZnSe and GaN. The work presented in this thesis is the very first coherent spectroscopic study performed for both ZnCdSe multiple quantum wells and the GaN material system.

The studies performed in the ZnSe material system have shown that many body effects play a significant role in the carrier dynamics on a femtosecond time scale. Extremely high order nonlinear wave mixing signals have been observed from a ZnCdSe multiple quantum well sample. Exciton-phonon interaction rates were measured for an epilayer of ZnSe and a ZnCdSe multiple quantum well sample. The interaction rates were shown to be stronger for ZnSe than for the GaAs quantum wells. This is due to the more polar nature of ZnSe which causes an enhancement of the Fröhlich interaction between excitons and phonons. Exciton-exciton interaction rates were also determined and it was shown that localization of excitons causes a decrease in the exciton-exciton interaction. This can be understood on the basis of an exciton cross section argument. Localized excitons are confined to a smaller region of the crystal and hence have less of an opportunity to interact with other excitons.

The optical properties of GaN was studied using linear absorption, femtosecond four-wave-mixing, and high carrier density pump-probe absorption measurements.

Excitonic features due to the A, B and C excitonic transitions were identified for the first time in absorption. LO phonon-assisted absorption was observed from epilayers of GaN. Temperature dependent four-wave-mixing was used to measure exciton-phonon interaction rates. Very large exciton-phonon interaction rates were observed. Quantum beats were also observed between the A and B excitonic transitions. The phase of the quantum beats was shown to change by 180 degrees when changing from the collinear to cross-linear polarization geometries. This change is theoretically modelled by solving the optical Bloch equations. Finally, amplified femtosecond pulses were used to measure exciton absorption saturation and recovery. Excitonic absorption was shown to saturate after a few hundred femtoseconds and recover with a characteristic time of $\approx$ 20 ps.

In order to make efficient optoelectronic devices and ultrafast modulators, one has to understand the basic carrier dynamics in a semiconductor. Much work is still needed in order to understand carrier dynamics in wide band gap semiconductors. For example, very little is known about how alloy fluctuations and crystal defects affect the carrier dynamics in wide gap materials. InGaN laser diodes operate as efficient light emitters even though the defect density is many orders of magnitude higher than would be allowable for device operation in the GaAs material system. Most semiconductor theories model only perfect crystal lattices so it would be interesting to learn how this large defect density affects the ultrafast optical properties. It would also be very interesting to perform ultrafast spectroscopy on InGaN and AlGaN alloys as these materials attract more and more attention.

BIBLIOGRAPHY

1. M.A. Haase, J. Oiu, J.M. Depuydt, and H. Cheng, Appl. Phys. Lett. **59**, 1272 (1991).

2. R.M. Park, M.B. Troffer, C.M. Rouleau, J.M. Depuydt, and M.A. Haase, Appl. Phys. Lett. **57**, 2127 (1990).

3. S. Tanaguchi, T. HIno, S. Itoh, K. Nakano, N. Nakayama, A. Ishibashi, M. Ikeda, Electronics Letters **32**, 552 (1996).

4. I. Akasaki, H. Amano, Y. Koide, K. Hiramatsu, and N. Sawaki, J. Cryst. Growth **98**, 209 (1989).

5. S. Nakamura, M. Senoh. S. Nagahama, N. Iwasa, T. Yamada, T. Matsushita, H. Kiyoku, and Y. Sugimoto, Jpn. J. Appl. Phys. **35**, L74 (1993).

6. S. Nakamura, M. Senoh, S.-I. Nagahama, N. Iwasa, T. Yamada, T. Matsushita, H. Kiyoku, Y. Sugimoto, T. Kozaki, H. Umemoto, M. Sano, and K. Chocho, Jpn. J. Appl. Phys. **36**, 1568 (1997).

7. C. Kittel, *Introduction to Solid State Physics*, John Wiley and Sons, 1986.

8. K. Boer, *Survey of Semiconductor Physics*, Van Nostrand Reinhold, New York, 1990.

9. This figure was taken from the Navel Research Laboratory home page at http:/cst-www.nrl.navy.mil/lattice/index.html.

10. S. Adachi and T. Taguchi, Phys. Rev. B **43**, 9569 (1991).

11. This figure was taken from the Navel Research Laboratory home page at http:/cst-www.nrl.navy.mil/lattice/index.html.

12. W.R.L. Lambrecht, B. Segall, J. Rife, W.R. Hunter, and D.K. Wickenden, Phys. Rev. B **51**, 13516 (1995).

13. Yu.M. Sirenko, J.B. Jeon, K.W. Kim, M.A. Littlejohn, and M.A. Stroscio, Phys. Rev. B **53**, 1997 (1996).

14. S.L. Chuang and C.S. Chang, Phys. Rev. B **54**, 2491 (1996).

15. R. Elliot, Phys. Rev. **108**, 1384 (1957).

16. R. Knox, *Solid State Physics*, volume 5, Academic Press, 1963.

17. G. Hite, D.T.F. Marple, M. Aven, and B. Segall, Phys. Rev. **156**, 850 (1967).

18. G.G. Macfarlane, T.P. McLean, J.E. Quarrington, and V. Roberts, Phys. Rev. **111**, 1245 (1958).

19. G.G. Macfarlane, T.P. McLean, J.E. Quarrington, and V. Roberts, Phys. Rev. **108**, 1377 (1957).

20. M. Sturge, Phys. Rev. **127**, 768 (1962).

21. D. Sell, Phys. Rev. B **6**, 3750 (1972).

22. D.G. Thomas and J.J. Hopfield, Phys. Rev. **128**, 2135 (1962).

23. E. Gutsche and J. Voigt, *Proceedings of the Inter. Conf. II-VI Semicond.*, Benjamin, New York, 1967.

24. R. Dingle, D.D. Sell, S.E. Stokowski, and M. Ilegems, Phys. Rev. B **4**, 1211 (1971).

25. W. Shan, X.C. Xie, J.J. Song, and B. Goldenberg, Appl. Phys. Lett. **66**, 3492 (1996).

26. W. Shan, B.D. Little, A.J. Fischer, J.J. Song, B. Goldenberg, W.G. Perry, M.D. Bremser, and R.F. Davis, Phys. Rev. B **54**, 16369 (1996).

27. W.Shan, T.J. Schmidt, R.J. Hauenstein, J.J. song, and B. Goldenberg, Appl. Phys. Lett. **66**, 3492 (1995).

28. S. Chichibu, H. Okumura, S. Nakamura, G. Feuillet, T. Azuhata, T. Sota, and S. Yoshida, Jpn. J. Appl. Phys. **36**, 1976 (1997).

29. S. Chichibu, T. Azuhata, T. Sota, and S. Nakamura, J. Appl. Phys. **79**, 2784 (1996).

30. A. Shikanai, T. Azuhata, T. Sota, S. Chichibu, A. Kuramata, K. Horino, and S. Nakamura, J. Appl. Phys. **81**, 417 (1997).

31. C.F. Li, Y.S. Huang, L. Malikova, and F.H. Pollak, Phys. Rev. B **55**, 9251 (1997).

32. H. Amano, N. Watanabe, N. Koide, and I. Akasaki, Jpn. J. Appl. Phys. **32**, L1000 (1993).

33. M. Manasreh, Phys. Rev. B **53**, 16425 (1996).

34. H. Haug and S.W. Koch, *Quantum Theory of the Optical and Electronic Properties of Semiconductors*, World Scientific, New Jersey, 1990.

35. R. Planel, A. Bonnot, and C. Benoit a la Guillaume, Phys. Stat. Sol. (b) **58**, 251 (1973).

36. D. Behr, J. Wagner, J. Schneider, H. Amano, and I. Akasaki, Appl. Phys. Lett. **68**, 2404 (1996).

37. B. Monemar, J.P. Bergman, I.A. Buyanova, W. Li, H. Amano, and I.Akasaki, MRS Internet Journal: Nitride Semiconductor Research **1**, 2 (1996).

38. D.S. Chemla, D.A. Miller, P.W. Smith, A.C. Gossard, and W. Wiegmann, IEEE J. Quantum Electron. **QE-20**, 265 (1984).

39. Y. Varshni, Physica **34**, 149 (1967).

40. D.S. Kim, J. Shah, J.E. Cunningham, T.C. Damen, W. Schaefer, M. Hartmann, and S. Schmitt-Rink, Phys. Rev. Lett. **68**, 1006 (1992).

41. A.J. Fischer, D.S. Kim, J. Hays, W. Shan, J.J. Song, D.B. Eason, J.Ren, J.F. Schetzina, H. Luo, J.F. Schetzina, Z.Q. Zhu, T. Yao, J.F. Klem, W. Schaefer, Phys. Rev. Lett. **73**, 2368 (1994).

42. J. Petalas, S. Logothetidis, S. Boultadikis, M. Alouani, and J.M. Wills, Phys. Rev. B **52**, 8082 (1995).

43. A.J. Fischer, W. Shan, G.H. Park, J.J. Song, D.S. Kim, D.S. Yee, R. Horning, B. Goldenberg, Phys. Rev. B **56**, 1077 (1997).

44. D. P. H.J. Eichler, P. Gunter, *Laser Induced Dynamic Gratings*, Springer-Verlag Berlin, 1986.

45. P.C. Becker, H.L. Fragnito, C.H. Brito Cruz, R.L. Fork, J.E. Cunningham, J.E. Henry, C.V. Shank, Phys. Rev. Lett. **61**, 1647 (1988).

46. K. Leo, E.O. Goebel, T.C. Damen, J. Shah, S. Schmitt-Rink, W. Schaefer, J.F. Mueller, K. Koehler, and P. Ganser, Phys. Rev. B **44**, 5726 (1991).

47. L. Schultheis, J. Kuhl, A. Honold, and C.W. Tu, Phys. Rev. Lett. **57**, 1797 (1986).

48. C. Cohen-Tannoudji, *Frontiers in Laser Spectroscopy*, Amsterdam: North-Holland, 1977.

49. S. Feneuville, Rep. Prog. Phys. **40**, 1257 (1977).

50. T. Yajima and Y. Taira, J. Phys. Soc. Jpn. **47**, 1620 (1979).

51. L. Allen and J.H. Eberly, *Optical Resonance and Two-Level Atoms*, Wiley, New York, 1975.

52. P. Butcher and D. Cotter, *The Elements of Nonlinear Optics*, Cambridge University Press, Cambridge, 1990.

53. M. Levenson and S. Kano, *Introduction to Nonlinear Laser Spectroscopy*, Academic Press, San Diego, 1988.

54. C. Cohen-Tannoudji, B. Diu, and F. Laloe, *Quantum Mechanics*, volume 1, John Wiley and Sons, New York, 1977.

55. Y. Shen, *The Principles of Nonlinear Optics*, John Wiley and Sons, New York, 1984.

56. S. Schmitt-Rink, D.S. Chemla, and D.A.B. Miller, Phys. Rev. B **32**, 6601 (1985).

57. M. Lindberg and S.W. Koch, Phys. Rev. B **38**, 3342 (1988).

58. M. Lindberg and S.W. Koch, J. Opt. Soc. Am. B **5**, 139 (1988).

59. M. Lindberg, R. Binder, and S.W. Koch, Phys. Rev. A **45**, 1865 (1992).

60. Y.Z. Hu, R. Binder, S.W. Koch, S.T. Cundiff, H. Wang, D.G. Steel, Phys. Rev. B **49**, 14382 (1994).

61. M. Wegener, D.S. Chemla, S. Schmitt-Rink, W. Shaefer, Phys. Rev. A **42**, 5675 (1990).

62. K. Leo, E.O. Goebel, T.C. Damen, J. Shah, S Schmitt-Rink, W. Shaefer, J.F. Mueller, K. Koehler, and P. Ganser, Phys. Rev. B **44**, 5726 (1991).

63. H. Wang, K. Ferrio, D.G. Steel, Y.Z. Hu, R. Binder, S.W. Koch, Phys. Rev. Lett. **71**, 1261 (1993).

64. L. Schultheis, J. Kuhl, A. Honold, and C.W. Tu, Phys. Rev. Lett. **57**, 1635 (1986).

65. A. Honold, L. Schultheis, J. Kuhl, and C.W. Tu, Phys. Rev. B **40**, 6442 (1989).

66. C. Stafford, S. Schmitt-Rink, W. Schaefer, Phys. Rev. B **41**, 10000 (1990).

67. B. Levine, Phys. Rev. B **7**, 2600 (1973).

68. T. Saiki, K. Takeuchi, M. Kuwata-Gonokami, T. Mitsuyu, and K. Ohkawa, Appl. Phys. Lett. **60**, 192 (1992).

69. J. Baumberg, D.D. Awschalom, N. Samarth, H. Luo, and J.K. Furdyna, Phys. rev. Lett. **72**, 717 (1994).

70. R. Hellmann, M. Koch, J. Feldmann, S.T. Cundiff, G.O. Goebel, D.R. Yakovlev, A. Waag, and G. Landwehr, Phys. Rev. B **48**, 2847 (1993).

71. R.P. Stanley, J. Hegarty, R. Fischer, J. Feldmann, E.O Goebel, R.D. Feldmann, and R.F. Austin, Phys. Rev. Lett. **67**, 128 (1991).

72. H. Schwab, V.G. Lyssenko, and J.M. Hvam, Phys. Rev. B **44**, 3999 (1991).

73. G. Noll, U. Siegner, S.G. Shevel, and E.O. Goebel, Phys. Rev. Lett. **64**, 792 (1990).

74. N. P. et al., Appl. Phys. Lett. **61**, 3154 (1992).

75. S. Adachi and T. Taguchi, Phys. Rev. B **43**, 9569 (1991).

76. N. P. et al., Phys. Rev. B **45**, 6037 (1992).

77. P. B. et al., Phys. Rev. Lett. **68**, 1876 (1992).

78. R.A. Soref and H.W. Moos, J. Appl. Phys. **35**, 2152 (1964).

79. F.W. Scholl and C.L. Tang, Phys. Rev. B **8**, 1973 (1973).

80. C.L. Tang and C. Flytzanis, Phys. Rev. B **4**, 2520 (1971).

81. J. K. et al., Adv. Solid State Phys. **29**, 157 (1990).

82. D.S. Kim, J. Shah, J.E. Cunningham, T.C. Damen, S. Schmitt-Rink, and W. Schaefer, Phys. Rev. Lett. **68**, 2838 (1992).

83. K. Leo, M. Wegener, D.S. Chemmla, E.O. Goebel, T.C. Damen, S. Schmitt-Rink, and W. Schaefer, Phys. Rev. Lett. **65**, 1340 (1990).

84. D.S. Kim, J. Shah, T.C. Damen, W. Shaefer, F. Jahnke, S. Schmitt-Rink, K. Koehler, Phys. Rev. Lett. **69**, 2725 (1992).

85. S. Weiss, M.-A. Mycek, J.-Y. Bigot, S. Schmitt-Rink, and D.S. Chemla, Phys. Rev. Lett. **69**, 2685 (1992).

86. B.F. Feuerbacher, J. Kuhl, and K. Ploog, Phys. Rev. B **43**, 2439 (1991).

87. S. Bar-Ad and I. Bar-Joseph, Phys. Rev. Lett. **66**, 2491 (1991).

88. R. R. et al., Solid State Commun. **81**, 51 (1992).

89. S. Wu, X.-C. Zhang, and R.L. Fork, Appl. Phys. Lett. **61**, 919 (1992).

90. J. Lee, E. Koteles, and M.O. Vassell, Phys. Rev. B **33**, 5512 (1986).

91. G. Manzke, K. Henneberger, and V. May, Phys. Stat. Sol. **139**, 233 (1987).

92. L. Schultheis, A. Honold, J. Kuhl, K. Koehler, and C.W. Tu, Phys. Rev. B **34**, 9027 (1986).

93. J. Hegarty, M.D. Sturge, C. Weisbuch, A.C. Gossard, and W. Wiegmann, Phys. Rev. Lett. **49**, 930 (1982).

94. J. Hegarty and M.D. Sturge, J. Opt. Soc. Am. B **2**, 1143 (1985).

95. H. Wang and D.G. Steel, Appl. Phys. A **53**, 514 (1991).

96. J. Hegarty and L. Goldner, Phys. Rev. B **30**, 7246 (1984).

97. C. Weisbuch, R. Dingle, A.C. Gossard, and W. Weigmann, Solid State Commun. **38**, 709 (1981).

98. A. Ourmazd, D.W. Taylor, and J. Cunningham, Phys. Rev. Lett. **62**, 933 (1989).

99. S.T. Cundiff, H. Wang, and D.G. Steel, Phys. Rev. B **46**, 7248 (1992).

100. M.D. Webb, S.T. Cundiff, and D.G. Steel, Phys. Rev. B **43**, 12658 (1991).

101. T. Takagahara, Phys. Rev. B **32**, 7013 (1985).

102. B. Kosicki, R.J. Powell, and J.C. Burgiel, Phys. Rev. Lett. **24**, 1421 (1970).

103. K. Osamura, K. Makajima, Y. Murkami, P. Shingu, and A. Ohtsuki, Solid State Commun. **11**, 617 (1972).

104. J.J. Song and W. Shan, *Group III Semiconductor Nitride Compounds:Physics and Applications*, Oxford University Press, London, 1997.

105. G.D. Chen, M. Smith, J.Y. Lin, A. Salvador, B.N. Sverdlov, A. Botchkarev, and H. Morkoc, J. Appl. Phys. **79**, 2675 (1996).

106. B. Taheri, J. Hays, and J.J. Song, Appl. Phys. Lett. **68**, 587 (1996).

107. D. Kim, I.H. Libon, C. Voelkmann, Y.R. Shen, and V. Petrova-Koch, Phys. Rev. B **55**, R4907 (1997).

108. J. Miragliotta and D.K. Wickenden, Phys. Rev. B **53**, 1388 (1996).

109. I. Catalano, A, Cingolani, M. Lugara, and A. Minafra, Optics Comm. **23**, 419 (1977).

110. C.-K. Sun, F. Vallee, S. Keller, J.E. Bowers, and S.P. Denbaars, Appl. Phys. Lett. **70**, 2004 (1997).

111. V.G. Lyssenko, J. Erland, I. Balsev, K.-H. Pamtke, B.S. Razbirin, and J.M. Hvam, Phys. Rev. B **48**, 5720 (1993).

112. S. Schmitt-Rink, D. Bennhardt, V. Heuckeroth, P. Thomas, P. Haring, G. Maidorn, H. Bakker, K. Leo, D.S. Kim, J. Shah, and K. Koehler, Phys. Rev. B **46**, 10460 (1992).

113. W. Shan, R.J. Hauenstein, A.J. Fischer, J.J. Song, W.G. Perry, M.D. Bremser, R.F. Davis, and B. Goldenberg, Phys. Rev. B **54**, 13460 (1996).

114. S. Rudin, T. Reinecke, and B. Segall, Phys. Rev. B **42**, 11218 (1992).

115. M. Koch, J. Feldmann, G. von Plessen, E.O. Goebel, P. Thomas, and K. Koehler, Phys. Rev. Lett. **69**, 3631 (1992).

116. T.J. Schmidt, J.J. Song, Y.C. Chang, R. Horning, and B. Goldenberg, Appl. Phys. Lett. , (to be published) (1998).

117. J. Shah, R.F. Leheny, and W. Wiegmann, Phys. Rev. B 4, 1577 (1977).

118. C.V. Shank, R.L. Fork, R.F. Leheny, and J. Shah, Phys. Rev. Lett. **42**, 112 (1979).

119. G.W. Fehrenbach, W. Schaefer, and R.G. Ulbrich, J. Lumin. **30**, 154 (1985).

120. T. Gong, P.M. Fauchet, J.F. Young, and J.P. Kelly, Phys. Rev. B **44**, 6542 (1991).

121. W.H. Knox, R.L. Fork, M.C. Downer, D.A.B. Miller, D.S. Chemla,C.V. Shank, A.C. Gossard, and W. Wiegmann, Phys. Rev. Lett. **54**, 1306 (1985).

122. C.V. Shank, R.L. Fork, R. Yen, J. Shah, B.I. Greene, A.C. Gossard, and C. Weisbuch, Solid State Commun. **47**, 981 (1983).

123. G. Coli, A. Passaseo, D. Greco, R. Cingolani, M. Tagliaferri, P. DiTrapani, and A. Andreoni, Appl. Phys. Lett. **71**, 915 (1997).

124. A.J. Fischer, W. Shan, J.J. Song, Y.C. Chang, R. Horning, and B. Goldenberg, Appl. Phys. Lett. **71**, 1981 (1997).

125. A.A. Klochikhin, B.S. Razbirin, D.K. Nelson, T. Amand, M. Brousseau, J. Collet, A. Cornet, and M. Pugnet, Phys. Stat. Sol. (b) **147**, 727 (1988).

126. W. Shan, X.C. Xie, J.J. Song, and B. Goldenberg, Appl. Phys. Lett. **67**, 2512 (1995).

127. M. Van Exter, D. Grischkowsky, IEEE Trans. Microwave Theory Tech. **38**, 1684 (1990).

128. D. Grischkowsky, S. Keiding, M. Van Exter, and Ch. Fattinger, J. Opt. Soc. Am. B **7**, 2006 (1990).

129. S.L. Chuang, S. Schmitt-Rink, B.I. Greene, P.N. Saeta, and A.F.J. Levi, Phys. Rev. Lett. **68**, 102 (1992).

130. A. Rice, Y. Jin, F. Ma, X.-C. Zhang, Appl. Phys. Lett. **64**, 1324 (1994).

131. X.-C. Zhang, Y. Jin, and X.F. Ma, Appl. Phys. Lett. **61**, 2764 (1992).

132. Q. Wu and Z.-C. Zhang, Appl. Phys. Lett. **71**, 1285 (1997).

133. Q. Wu and X.-C. Zhang, Appl. Phys. Lett. **67**, 3523 (1995).

134. Q. Wu, T.D. Hewitt, X.-C. Zhang, Appl. Phys. Lett. **69**, 1026 (1996).

135. C. Winnewisser, P. Uhd Jepsen, M. Schall, V. Schyja, and H. Helm, Appl. Phys. Lett. **70**, 3069 (1997).

136. A. Nahata, A.S. Weling, and T. Heinz, Appl. Phys. Lett. **69**, 2321 (1996).

137. ATT Bell Labs, Electronic Engineering Times **852**, 39 (1995).

138. P.C.M. Planken, M.C. Nuss, I. Brener, K.W. Goossen, M.S.C. Luo, S.L. Chuang, L. Pfeiffer, Phys. Rev. Lett. **69**, 3800 (1992).

139. P.C.M. Planken, I. Brener, M.C. Nuss, M.S.C. Luo, S.L. Chuang, L.N. Pfeiffer, Phys. Rev. B **49**, 4668 (1994).

140. H.G. Roskos, M.C. Nuss, J. Shah, K. Leo, D.A.B. Miller, A.M. Fox, S. Schmitt-Rink, K. Koehler, Phys. Rev. Lett. **68**, 2216 (1992).

141. M. Li, F.G. Sun, G.A. Wagoner, M. Alexander, and X.-C. Zhang, Appl. Phys. Lett. **67**, 25 (1995).

142. X.-C. Zhang, B.B. Hu, J.T. Darrow, and D.H. Auston, Appl. Phys. Lett. **56**, 1011 (1990).

APPENDICES

APPENDIX A

CALCULATION OF THE THIRD ORDER POLARIZATION

In this appendix, we will calculate the third order polarization diffracted into the $2\vec{k}_2 - \vec{k}_1$ direction and show how this can be used to find T_2. For the case of a semiconductor where $T_1 \gg T_2$, we can relate the homogeneous linewidth to T_2 by the relation $\Gamma_h = 2\hbar/T_2$.

The third order perturbation theory used to describe the results of CT-DFWM experiments was first calculation by Yajima and Taira [50]. The development here will follow their derivation and notation, but with more elaboration. Since we are developing this within the framework of the two-level model, we begin with the same Hamiltonians

$$\hat{H}_o = \begin{bmatrix} E_a & 0 \\ 0 & E_b \end{bmatrix}, \quad \hat{\rho} = \begin{bmatrix} \rho_{aa} & \rho_{ab} \\ \rho_{ba} & \rho_{bb} \end{bmatrix}, \tag{60}$$

$$\hat{H}_I = \begin{bmatrix} 0 & -e\vec{r}_{ab} \cdot \vec{E}(t) \\ -e\vec{r}_{ba} \cdot \vec{E}(t) & 0 \end{bmatrix} \equiv \begin{bmatrix} 0 & Hab \\ H_{ba} & 0 \end{bmatrix}, \tag{61}$$

$$\hat{\rho} = \begin{bmatrix} \rho_{aa} & \rho_{ab} \\ \rho_{ba} & \rho_{bb} \end{bmatrix}, \tag{62}$$

$$\left[\hat{H}_R, \hat{\rho}\right]_{bb} = -i\hbar\frac{\rho_{bb}}{T_1}, \tag{63}$$

$$\left[\hat{H}_R, \hat{\rho}\right]_{aa} = i\hbar\frac{\rho_{aa}}{T_1} = i\hbar\frac{(1-\rho_{bb})}{T_1}, \tag{64}$$

$$\left[\hat{H}_R, \hat{\rho}\right]_{ab} = -i\hbar\frac{\rho_{ab}}{T_2}, \tag{65}$$

$$\left[\hat{H}_R, \hat{\rho}\right]_{ba} = -i\hbar\frac{\rho_{ba}}{T_2}. \tag{66}$$

Plugging these into Eqn.(??), we arrive at the following equations of motion:

$$i\hbar\frac{d\rho_{aa}}{dt} = H_{ab}\rho_{ba} - \rho_{ab}H_{ba} - i\hbar\frac{\rho_{aa}}{T_1}, \tag{67}$$

$$i\hbar\frac{d\rho_{bb}}{dt} = H_{ab}\rho_{ba} - \rho_{ab}H_{ba} - i\hbar\frac{\rho_{bb}}{T_1}, \tag{68}$$

$$i\hbar\frac{d\rho_{ba}}{dt} = i\hbar\frac{d\rho^*_{ab}}{dt} = E_b\rho_{ba} - \rho_{ab}E_a + H_{ba}\rho_{aa} - \rho_{bb}H_{ba} - i\hbar\frac{\rho_{ba}}{T_2}. \tag{69}$$

These can be written more compactly using $\rho_D \equiv \rho_{aa} - \rho_{bb}$ and $\hbar\Omega_{ba} = E_b - E_a$:

$$\frac{d\rho_D}{dt} = -\frac{2i}{\hbar}\left(H_{ab}\rho_{ba} - \rho_{ab}H_{ba}\right) - i\hbar\frac{\left(\rho_D - \rho_D^{(0)}\right)}{T_1}, \tag{70}$$

$$\frac{d\rho_{ba}}{dt} = \frac{d\rho^*_{ab}}{dt} = -\frac{i}{\hbar}H_{ba}\rho_D - \left(\frac{1}{T_2} + \Omega_{ba}\right)\rho_{ba}, \tag{71}$$

where $\rho_D^{(0)}$ is the equilibrium density matrix. The interaction terms are given by

$$H_{ba} = H^*_{ab} = -\mu_{ba}\hat{E}(\vec{r},t)\exp(-i\omega t) + c.c., \tag{72}$$

and for a CT-DFWM experiment we are interested in an electric field of the form

$$\hat{E}(\vec{r},t) = \tilde{E}_1(\vec{r},t)\exp(i\vec{k}_1\cdot\vec{r}) + \tilde{E}_2(\vec{r},t)\exp(i\vec{k}_2\cdot\vec{r}). \tag{73}$$

We now expand the density operator in a power series in the interaction Hamiltonian as described in section 2.1. The nth order equations of motion are given by

$$\frac{d\rho_D^{(n)}}{dt} = -\frac{2i}{\hbar}\left(H_{ab}\rho_{ba}^{(n-1)} - \rho_{ab}^{(n-1)}H_{ba}\right) - i\hbar\frac{\left(\rho_D^{(n)} - \rho_D^{(0)}\right)}{T_1}, \tag{74}$$

$$\frac{d\rho_{ba}^{(n)}}{dt} = -\frac{i}{\hbar}H_{ba}\rho_D^{(n-1)} - \left(\frac{1}{T_2} + \Omega_{ba}\right)\rho_{ba}^{(n)}. \tag{75}$$

These are first order linear differential equations with solutions

$$\hat{\rho}_{ba}^{(n)} = \frac{i\mu_{ba}}{\hbar}\exp\left[-\left(\frac{1}{T_2} + i\Delta\omega\right)t\right]\int_{-\infty}^{t}\hat{E}(\vec{r},t')\rho_D^{(n-1)}\exp\left[\left(\frac{1}{T_2} + i\Delta\omega\right)t'\right]dt', \tag{76}$$

$$\rho_D^{(n)} = \frac{2i\mu_{ba}}{\hbar}\exp\left(-\frac{t}{T_1}\right)\int_{-\infty}^{t}\left\{\hat{E}(\vec{r},t')\hat{\rho}_{ab}^{(n-1)} + \hat{E}^*(\vec{r},t')\hat{\rho}_{ba}^{(n-1)}\right\}\exp\left[\frac{t'}{T_1}\right]dt', \tag{77}$$

where $\Delta\omega \equiv \Omega_{ba} - \omega$ and $\hat{\rho}_{ab} \equiv \rho_{ab} \exp(i\omega t)$. The nth-order macroscopic polarization is given by

$$P^{(n)}(\vec{r},t) = \hat{P}^{(n)}(\vec{r},t)\exp(-i\omega t) + c.c., \tag{78}$$

$$\hat{P}^{(n)}(\vec{r},t) = N\int_0^\infty \mu_{ba}\,\hat{\rho}_{ba}^{(n)}(\vec{r},t,\omega_0)\;g(\omega_0)\;d\omega_0, \tag{79}$$

where we have included inhomogeneous broadening with a distribution function $g(\omega_0)$, subject to the following normalization condition:

$$\int_0^\infty g(\omega_0)\;d\omega_0 = 1. \tag{80}$$

We now need to calculation the off-diagonal density matrix elements to third order. In general, there will be components with wave vectors of $\vec{k}_1$, $\vec{k}_2$, $\vec{k}_3 = 2\vec{k}_2 - \vec{k}_1$, $\vec{k}_4 = 2\vec{k}_1 - \vec{k}_2$; however, we are only interested in the $\vec{k}_3$ component. Substituting Eqn.(73) in for the electric field, keeping only $\vec{k}_3$ terms, and after some non-trivial algebra we arrive at:

$$\begin{aligned}\hat{\rho}_{ba}^{(3)}\left(\vec{k}_3\right) &= -2i\rho^{(0)}\left(\tfrac{\mu_{ba}}{\hbar}\right)^3\exp\left[-\left(\tfrac{1}{T_2}+i\Delta\omega\right)t + i\vec{k}_3\cdot\vec{r}\right]\\ &\text{x}\int_{-\infty}^{t}\int_{-\infty}^{t'}\int_{-\infty}^{t''}\{\tilde{E}_2(\vec{r},t')\,\tilde{E}_2(\vec{r},t'')\,\tilde{E}_1^*(\vec{r},t''')\exp\left[\gamma(t'-t'') + \tfrac{t'''}{T_2} + i\Delta\omega(t'+t''-t''')\right]\\ &+\tilde{E}_2(\vec{r},t')\,\tilde{E}_1^*(\vec{r},t'')\,\tilde{E}_2^*(\vec{r},t''')\exp\left[\gamma(t'-t'') + \tfrac{t'''}{T_2} + i\Delta\omega(t'-t''+t''')\right]\}dt'''dt''dt',\end{aligned} \tag{81}$$

where $\gamma = \frac{1}{T_2} - \frac{1}{T_1}$. In the short pulse limit, we assume that the electric field for each pulse can be expressed as the following delta function:

$$\tilde{E}_j(\vec{r},t) = \frac{\mu_{ba}}{\hbar}\Theta_j\delta(t-t_j) \qquad (j=1,2), \tag{82}$$

where Θ_j is the pulse area of the jth pulse. We assume that the distribution function $g(\omega_0)$ has a Gaussian form given by

$$g(\omega_0) = \frac{1}{\sqrt{\pi}\delta\omega}\exp\left[\frac{-(\omega-\omega_0)^2}{(\delta\omega)}\right], \tag{83}$$

where $\delta\omega$ represents the inhomogeneous linewidth. Using Eqn.(78) one can show that the macroscopic polarization is given by

$$\hat{P}_3^{(3)}(\vec{r},t) = \left\{\begin{array}{ll} -i\rho^{(0)}N\mu_{ba}\Theta_1(\Theta_2)^2\exp\left[i\vec{k}_3\cdot\vec{r} - \frac{(t-t_1)}{T_2}\right] & t \rangle\, t_2 \\ 0 & t \,\langle\, t_2 \end{array}\right\}. \tag{84}$$

In the experiment shown in Fig. 1, we are interested in an averaged polarization. Therefore, we will calculate the energy of the light emitted using the following formula:

$$J = \int_{-\infty}^{+\infty} \left| \hat{P}_3^{(3)} (\vec{r}, t) \right|^2 dt. \tag{85}$$

Performing this integration, we arrive at final expressions for the energy of the third-order polarization. For the case of inhomogeneous broadening $\left(\delta\omega \gg \frac{1}{T_2}\right)$:

$$J_I = \left\{ \begin{array}{ll} A \exp\left[-\frac{4}{T_2}(t_2 - t_1)\right] \left\{1 + \Phi\left[\frac{\delta\omega}{\sqrt{\pi}}(t_2 - t_1)\right]\right\} & t_2 - t_1 \rangle\ 0 \\ 0 & t_2 - t_1 \langle\ 0 \end{array} \right\} \tag{86}$$

where $\Phi(x) \equiv \frac{2}{\sqrt{\pi}} \int_0^x \exp(-t^2)\, dt$ and A is some constant. For the case of homogeneous broadening

$$J_H = \left\{ \begin{array}{ll} B \exp\left[-\frac{2}{T_2}(t_2 - t_1)\right] & t_2 - t_1 \rangle\ 0 \\ 0 & t_2 - t_1 \langle\ 0 \end{array} \right\}, \tag{87}$$

where B is some constant. These two equations can now be used to interpret the decay times found in CT-DFWM experiments. We see that we can relate the four-wave-mixing decay time to the transverse relaxation time by the following relations

$$T_2 = 4 \cdot \tau_{FWM} \qquad \text{inhomogeneously broadening,} \tag{88}$$

$$T_2 = 2 \cdot \tau_{FWM} \qquad \text{homogeneous broadening.} \tag{89}$$

Thus the homogeneous linewidth can be determined even in the presence of inhomogeneous broadening.

2

VITA

Arthur J. Fischer

Candidate for the Degree of

Doctor of Philosophy

Thesis: ULTRAFAST CARRIER DYNAMICS OF WIDE GAP SEMICONDUCTORS STUDIED VIA FOUR-WAVE-MIXING AND PUMP-PROBE SPECTROSCOPIES

Major Field: Physics

Biographical:

Personal Data: Born in Chicago, Illinois, on September 27, 1970, the son of Frederick C. and Madeleine B. Fischer.

Education: Graduated from Appleton High School East, Appleton, Wisconsin in May 1988; received Bachelor of Arts Degree in Physics from The University of Chicago, Chicago, Illinois in May 1992. Completed requirements for the Doctor of Philosophy Degree at Oklahoma State University in July 1998.

Professional Experience: Research Assistant, Department of Physics and Center for Laser and Photonics Research, Oklahoma State University, from August 1992 to present.

Professional Memberships: American Physical Society, Optical Society of America.